Modelling of sediment exchange processes and morphodynamics of gravel-bed Rivers

Van Hieu Bui

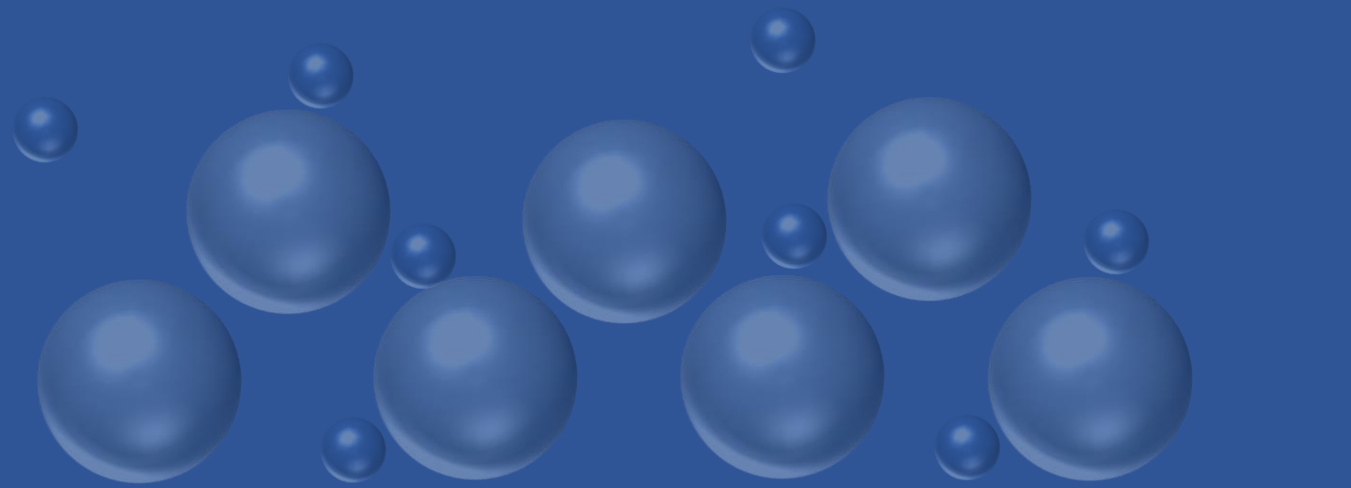

Munich, March 2020

Ingenieurfakultät Bau Geo Umwelt
Lehrstuhl für Wasserbau und Wasserwirtschaft

Modelling of sediment exchange processes and morphodynamics of gravel-bed Rivers

Van Hieu Bui

Vollständiger Abdruck der von der Ingenieurfakultät für Bau Geo Umwelt der Technischen Universität München zur Erlangung des akademischen Grades eines
Doktor-Ingenieurs (Dr.-Ing.)
genehmigten Dissertation.

Vorsitzender: Prof. Dr.-Ing. André Borrmann
Prüfer der Dissertation:

1. Prof. Dr.sc.tech. Peter Rutschmann
2. Prof. Dr.-Ing. Jochen Aberle
3. Prof. Dr. rer. nat. Michael Krautblatter

Die Dissertation wurde am 24.10.2019 bei der Technischen Universität München eingereicht und durch die Ingenieurfakultät Bau Geo Umwelt am 26.02.2020 angenommen.

> Knowledge in the head and virtue in the heart, time devoted to study or business, instead of show and pleasure, are the way to be useful and consequently happy.
>
> (John Adams, 1735-1826)

Acknowledgements

This Ph.D. research is difficult challenges, valuable chances to obtain valuable academic experience, and opportunities to surpass myself. The outcome of the research is only possible because of the assistance and cooperation of many individuals and organizations.

I would like to thank my mentor, Dr. Minh Duc Bui, and my supervisor, Prof. Dr. Peter Rutschmann, for years of guidance, mentoring, and encouragement. Their invaluable support and advice were critical both in enhancing my understanding of the subject and in providing me additional perspective on the study. My sincere thanks also go to Prof. Dr. André Borrmann, Prof. Dr. Jochen Aberle and Prof. Dr. Michael Krautblatter for taking time out of their busy schedule to help me in reviewing, evaluating and improving my thesis.

I would like to offer my grateful thanks to Thuyloi University for giving 4 years of absence for conducting this doctoral research. I thank TUM English Writing Center for supports and comments to improve this thesis. Particularly, I would like to thank the Vietnam International Education Development (VIED) Scholarship for offering me a prestigious scholarship to conduct this study. Without their support, none of my achievements would have been possible.

Enormous thanks to all colleagues at the Institute of Hydraulic and Water Resources Engineering – Technical University of Munich, Germany, for stimulating discussions and insights that have informed this thesis.

I would like to express my special appreciation and thanks to my family: my wife, my parents and my sister who not only supported me spiritually but also helped me care for my daughter and my son during my 4 years away from home.

Munich, February 2020
Van Hieu Bui
hieubv@tlu.edu.vn

Abstract

Fine sediment infiltration into void spaces in coarse bed material can potentially alter river morphodynamics and aquatic ecosystems. Understanding the alterations of gravel-bed structures, sediment transport, and the effects on aquatic habitat play an essential role in eco-hydraulic and sediment transport management. In recent years, the assessment of void changes in bed materials has attracted more attention. However, analyzing the morphological changes and grain size distribution associated with the porosity variations in gravel-bed rivers is still challenging.

A framework combining the Discrete Element Method (DEM) and Artificial Neural Network (ANN) was developed to predict the porosity and the fine sediment distribution. DEM was applied to simulate the 3D structure of packing-gravel-bed and fine infiltration processes under various forces. The sediment particle properties and interaction laws were posed into DEM and led to the collective behavior of the dissipative many-particle system. The developed algorithm and the image processing were used to extract information of the gravel-bed packing, grain size distribution, porosity variation and pore distribution from the results of particle simulation for training to machine learning models. In order to reduce computation time and to make connections between discrete element modelling and conventional hydro-morphodynamics modelling, ANN was applied to learn the rule of the fine sediment sorting and porosity variation in gravel, based on the generated data from DEM results. Analyzing the model results and comparing them with the measurement data show that our framework can successfully simulate the exchange process of fine sediment in gravel-bed rivers.

The porosity variation and fine sediment exchange was integrated to develop a bed variation model. A new model using a multi-layer concept to simulate morphological changes and grain size distribution was developed. This model considered the porosity variabilities in a gravel-bed river based on the mass conservation for each size fraction and the exchange of fine sediments between the surface and subsurface layers. The new model was tested on three straight channels. Analyzing the simulated results and comparing them with the observed data show that the developed model can successfully reproduce sediment transport, grain sorting processes, and bed level changes in gravel-bed rivers.

Keywords: numerical modelling; bed variation; porosity; grain sorting; DEM; ANN.

Zusammenfassung

In kiesführenden Flüssen kann die Wechselwirkung zwischen groben, bettbildenden Sedimenten und Feinsedimenten eine große Rolle spielen. Transportiertes Feinsediment kann in existierende Hohlräume in der Sohle eindringen, was zu Änderungen in der morphologischen Struktur des Gewässerbetts und damit auch dem aquatischen Ökosystem führt. Damit ist die Sohlporosität und das Verständnis der ablaufenden Prozesse eine wichtige Komponente für ökohydraulische Bewertungen sowie beim Sedimentmanagement generell. Entsprechend stieg das Interesse an einer Methode zur Bewertung der Veränderungen im Porenraum des Gewässers in den letzten Jahren an. Dennoch ist die Beschreibung der morphologischen Veränderungen wie die Korngrößenverteilung der Gewässersohle, die mit den Porositätsveränderungen verbunden sind, immer noch eine große Herausforderung.

Um Porositätsänderungen und die Verteilung von Feinsedimenten besser beschreiben und damit vorhersagen zu können, wurde ein integrales Modellkonzept entwickelt, welches die Diskrete-Elemente-Methode (DEM) und künstliche neuronale Netze (ANN) kombiniert. DEM wurde angewandt, um die dreidimensionale Struktur einer Kiessohle (packing gravel bed) sowie die Infiltrationsprozesse von Feinsedimenten unter Einwirkung verschiedener Kräfte zu simulieren. DEM ist in der Lage die Eigenschaften der einzelnen Sedimentpartikeln sowie die Wechselwirkungsgesetze realistisch darzustellen und bildet letztlich das das gemeinsamen Verhalten des dissipativen Mehrpartikelsystems akkurat ab. Mit den Ergebnissen der Partikelsimulation wurden ein Algorithmus zur Bildverarbeitung entwickelt, um Informationen über die Kiessohle, die Korngrößenverteilung, die Porositätsveränderung und die Porenverteilung zu gewinnen. Um die zeit- und rechenintensive DEM-Simulation mit einem konventionellen hydromorphodynamischen Model verbinden zu können, wird ein künstliches neuronales Netz (ANN) entwickelt. Dabei erlernt das ANN die Gesetzmäßigkeiten der Korngrößensortierung, der Porositätsveränderung im Kies, an Hand der generierten Daten aus den DEM-Ergebnissen. Die Analyse der Modelergebnisse und der Vergleich mit den Messdaten zeigen, dass das entwickelte Modellkonzept den Austauschprozess von

Feinsedimenten in Flüssen mit einer Kiessohle erfolgreich simulieren kann.

Mit den gewonnenen Erkenntnissen zu Porositätsveränderung und Feinsedimentaustausch wurde ein neuartiges Sohlveränderungsmodell entwickelt. Das neue Modell basiert auf einem Mehrschichtkonzept zur Simulation der morphologischen Veränderungen und der Korngrößenverteilung. Das Modell ist in der Lage die Porositätsveränderungen in einem Fluss mit Kiessohle abzubilden, unter Einhaltung der Massenerhaltung für jede Kornfraktion und dem Austausch von Feinsedimenten zwischen der Sedimentschicht der Sohloberfläche und den darunterliegenden Schichten. Das neue Modell wurde an drei geraden Kanälen verifiziert. Der Vergleich der Simulationsergebnisse mit tatsächlich gemessene Daten zeiget, dass das neu entwickelte Model den Sedimenttransport, die Kornsortierungsprozesse und die Sohlveränderung in Flüssen mit einer Kiessohle erfolgreich nachbilden kann.

Schlüsselwörter: numerical modelling; bed variation; porosity; grain sorting; DEM; ANN.

Table of contents

List of figures

List of tables

Nomenclature

Acronyms / Abbreviations

Adam	Adaptive Moment Estimation
ANN	Artificial Neural Network
ASF	Average Saturated Fines content
CFD	Computational Fluid Dynamics
CV	Control Volumes
DEM	Discrete Element Method
DNS	Direct Numerical Simulation
DOFs	Degrees Of Freedom
FDM	Finite Differences Method
FNN	Feedforward Neural Network
FVM	Finite Volume Method
MAE	Mean Absolute Error
MLP	Multilayer Perceptron
MPM	Meyer-Peter and Müller
NSE	Navier-Stokes equations
PDEs	Partial Differential Equations
R	Correlation coefficient

RANS	Reynolds-averaged Navier–Stokes
REV	Representation Elementary Volume
RMSE	Root Mean Square Error
SGD	Stochastic Gradient Descent
SWE	Shallow Water Equations
USCS	Unified Soil Classification System
WS	Watershed Segmentation

Chapter 1

Introduction

1.1 Background

Bed variation included morphodynamics and bed material characteristics, consequences of the sediment movement, is one of the important subjects in the hydrodynamics and river management. Sediment transport processes due to flowing water in gravel-bed rivers can be formed of bed load, suspended load, and movement inside the bed layer. More importantly, in the same hydraulic conditions, the transport rate of coarse size fraction may be different from the rate of fine size fraction. These lead to the distinct forms of gravel-bed rivers. Due to high-flow velocity, all finer particles may be eroded, leaving a layer of coarse particles. When the flow is unable to carry the coarse particles, then no more erosion occurs, which is known as an armoring process (Dietrich et al., 1989; Wilcock and DeTemple, 2005). Inversely, under low-flow conditions, sediment transport can cause extensive infiltration of fine sediment into void spaces in coarse bed material (Cui et al., 2008; Gibson et al., 2010), which is also known as clogging or colmation (Schälchli, 1992; Wu and Huang, 2000) (see Figure 1.1).

The change in grain size distribution of coarse and fine sediment not only lead to the variation in bed profile but also result in the change in porosity, a fraction of the volume of voids over the total volume of the gravel-bed river. According to Campbell (2000) and Selby and Hodder (1993), the porosity of sand-gravel mixtures can vary from about 0.10 to 0.50. Measured porosity values in the Rhine River range from 0.06 to 0.48 (Frings, Schuttrumpf,

---

Parts of this chapter were published as:

Bui, V.H.; Bui, M.D.; Rutschmann, P. Advanced Numerical Modeling of Sediment Transport in Gravel-Bed Rivers. Water 2019, 11, 550, doi:10.3390/w11030550.

and Vollmer, 2011) as an example.

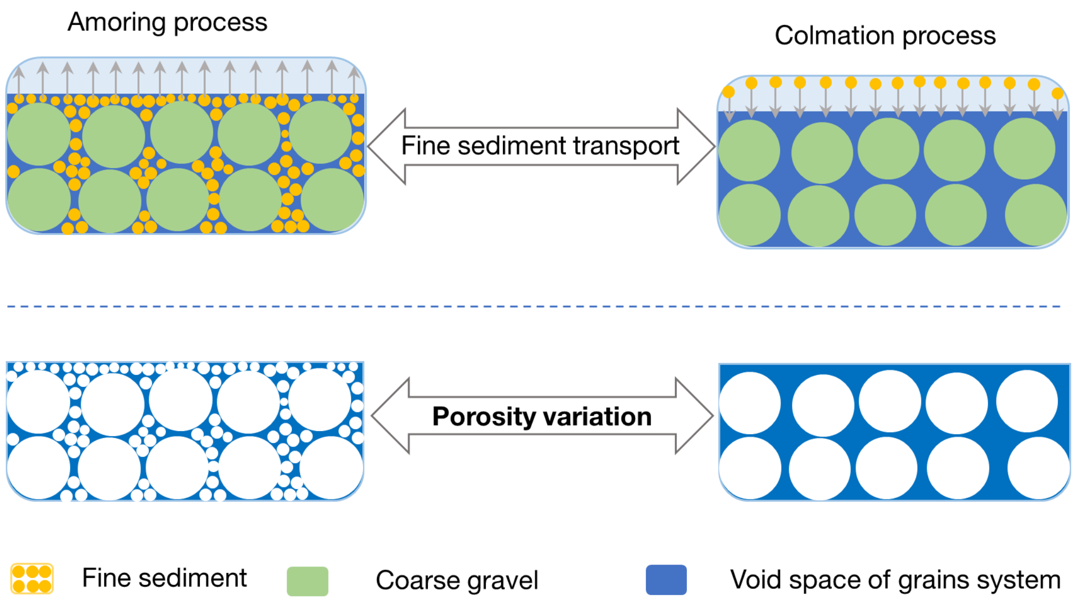

Figure 1.1 Porosity variation of grain system due to fine grain exchange.

The study of variation in porosity is vital for fluvial geomorphology assessment as well as in river ecosystem management. From a river management point of view, the amount of fine sediment stored in the void space of gravel-bed up to 22% (Frings, Kleinhans, and Vollmer, 2008) may be neglected during calculation by considering constant porosity. Morphologically, the porosity exerts strong influence on the rate of bed level changes (Verstraeten and Poesen, 2001; Wilcock, 1998). The impact of void space of gravel-bed on habitats for fish and aquatic insects is essential, and the importance of assessing the change in the void structure of the bed material in particularly has been strongly emphasized (Gayraud and Philippe, 2003).

Along with the development of computer science as well as the understanding in the interaction between hydrodynamic and sediment transport, numerical models have become useful tools for studying sediment transport and river engineering (Bui and Rutschmann, 2012). To model sediment transport processes as well as bed deformation, multi-layer models were applied for graded sediment transport. Despite the considerable variations of porosity, most models assumed that the porosity of bed material is constant. Therefore, sediment transport in the form of infiltration into the void spaces of the coarse bed, or fine particles in sublayers and the entrainment of fine sediment into the flow from the substrates are not taken into account. This assumption is inappropriate for simulating the sediment transport and bed variation in gravel-bed rivers, where fine sediment may be formed under the gravel surface layer. Furthermore, the exchange between bed material and transported sediment only takes place on the surface layer, and sediment transport from an upper layer to the lower layer is neglected. These assumptions are improper in gravel-bed rivers where finer sediment possibly drops into the subsurface layer.

1.2 Objectives

The main objective of this research is to develop a numerical hydromorphological model that considers the bed porosity change and the exchange flux of fine sediment between two different bed layers. To achieve this, the research has the following steps:

1. To study and analyze the conventional model for fine sediment exchange and porosity variation in gravel-bed rivers;
2. To develop a framework which combines Discrete Element Method (DEM) and Artificial Neural Network (ANN) for obtaining the porosity and fine sediment distribution, exchange rate between layers;
3. To construct an algorithm to calculate the grain size distribution and exchange rate then apply the image processing in porosity analyzing;
4. To build a new numerical model for bed variation of gravel-bed rivers considering porosity variation and exchange flux of fine sediment in two layers;
5. To verify the combined framework of DEM and ANN by comparing the simulated results with the experimental data;
6. To test the new bed variation model for three straight gravel-bed open channels.

1.3 Outline of the thesis

Chapter 2 focuses on the fundamental of hydrodynamics and morphodynamics. An introduction to the Navier-Stokes equations and its simplified form including Reynolds-Averaged-Navier-Stokes and shallow water theory are described in detail. The basics of sediment transport mechanisms include the concept of incipient motion of sediment particles and bed load equations are outlined therein. The modelling of the bed evolution component is provided by the description of the Exner equation. This chapter also encompasses the principles of numerical schemes for solving a system of partial differential equations, which model morphological evolution of the bed.

Chapter 3 illustrates the relationship between fine sediment infiltration and porosity variations of gravel-bed rivers. The concept of fine sediment, porosity, the controlling factor for gravel-bed included saturation state, the size ratio of fine sediment to gravel are introduced. The basic equation for fine sediment infiltration into immobile coarse and the infiltration experiment condition were mentioned. Theoretical and empirical methods for calculating porosity are also described in this chapter.

Chapter 4 contains a developed framework comprising of DEM and ANN to predict the porosity, fine sediment distribution, and exchange rate. DEM is used to simulate the gravel-bed structure and infiltration processes under various forces. A developed algorithm is applied to reproduce high resolution data from DEM results. A brief introduction of image processing to analyze pore distribution of simulated results is also characterized. A simple ANN (namely Feedforward Neural Network) used the DEM-based data to obtain the explicit relationship of porosity and fine sediment distribution.

Chapter 5 focuses on developing a new model using a multi-layer concept to simulate morphological changes and grain size distribution, taking into account the porosity variabilities in a gravel-bed river based on the mass conservation for each size fraction and the exchange of fine sediments between the surface and subsurface layers.

Chapter 6, which has three main parts presents the results and discussion. In the first part, the DEM results including porosity and fine sediment distribution (for verifying purposes, each simulation result was compared with the experimental results) are depicted. The generated data from DEM results based on the developed algorithm for calculating porosity and grain size distribution are also included in this section. The second part presents the results of predicting porosity and grain size distribution obtained from the Artificial Neural Network. The test result from ANN was compared with the DEM outputs to evaluate the efficiency of the ANN model. In the last part of this chapter, the new numerical model for bed-porosity variation is developed and tested for three straight gravel-bed open channels. The simulated results are then compared with the observed data to verify the improved model.

Chapter 7 makes some conclusions and recommendations for further research.

Chapter 2

Hydro-morphodynamic modelling

2.1 Overview

Hydro-morphodynamics comprises of hydrodynamics and morphodynamics. Hydrodynamics is a fluid mechanics subdiscipline that focuses on the forces exerted by or is applied to fluids and is popularly used in engineering to examine how energy and forces interact with fluids. To explore how conservation laws of energy, momentum, and mass apply to the incompressible liquid that is water, a river hydrodynamic model uses a series of equations. Under the impact of hydrodynamic forces, sediment transport as bed load is a crucial process that takes place in estuaries, rivers, and coastal regions. Frequently, this process and morphological changes of the bed may be detrimental to infrastructure and the environment. Sediment transport and the morphological evolution of the bed are governed by fluid flow properties, which in turn are influenced by any alteration in the bed morphology.

Fluid and bed motion form an interdependent two-phase phenomenon that must be evaluated through a component model system consisting of two distinct but interdependent parts: (1) a hydrodynamic component which defines flow evolution; and (2) a sediment transport/morphological component which defines bed evolution. This modelling system is generally called a hydro-morphological model. The standard method for conducting hydro-morphological simulations of rivers is to first decouple the hydrodynamic and morphodynamic systems. Decoupling is grounded on the logic that the channel bed responds at a much slower timescale than the flow. At the implementation level, these modules communicate by means of a quasi-steady morphodynamic time-stepping mechanism: during flow computation, the bed level is presumed constant, while calculating the bed level, flow, and sediment transport quantities are remain unchanged to the bed level changes. Additionally, the modules are connected at the programming level. The hydrodynamic component is often modeled by Reynold averaged Navier-Stokes equations (RANS), while the morphodynamic module is determined by the Exner equation.

2.2 Hydrodynamics

2.2.1 The Navier-Stokes equations

The movement of fluid in the physical domain is driven by various properties. For the purpose of bringing the behavior of fluid flow to light and developing a mathematical model, those properties have to be defined precisely as to provide the transition between the physical and the numerical domain. Velocity, pressure, temperature, density, and viscosity are the main properties that should be considered simultaneously when conducting a fluid flow examination.

The Navier-Stokes equations are the broadly applied mathematical model to examine changes on those properties during dynamic and/or thermal interactions. The equations are adjustable regarding the content of the problem and are expressed based on the principles of conservation of mass, momentum, and energy (White and Corfield, 2006):

Equation of continuity: The equation of continuity is based on the law of conservation of mass, which states that the mass in the control volume can be neither created nor destroyed in accordance with physical laws. The continuity equation can be written in either differential or integral form. In differential form, consider the infinitesimal control volume in Figure 2.1.

The difference between the mass fluxes entering and leaving the differential control volume equals the rate of increase of internal mass. The assumption of continuous fluid medium yields the following differential relationship:

$$\frac{\partial \rho_m}{\partial t} + \frac{\partial \rho_m v_x}{\partial x} + \frac{\partial \rho_m v_y}{\partial y} + \frac{\partial \rho_m v_z}{\partial z} = 0 \tag{2.1}$$

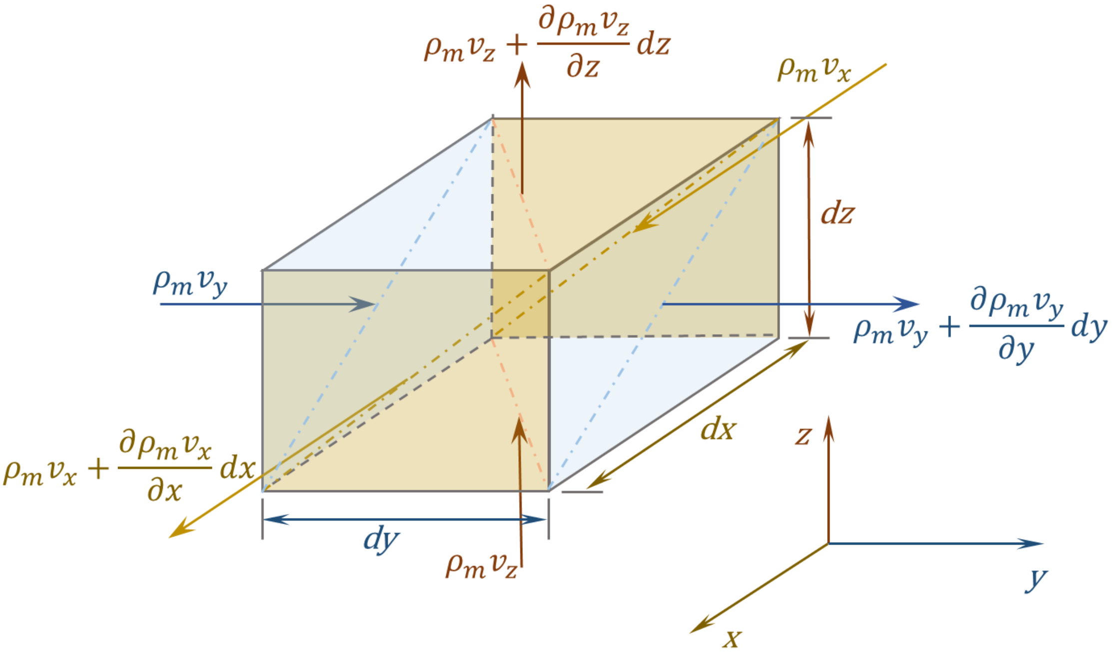

Figure 2.1 Infinitesimal element of fluid.

For a homogeneous incompressible fluid, the mass density is independent of space and time ($\rho_m = constant$); consequently, $\partial \rho_m / \partial t = 0$ and the divergence of the velocity vector must be zero:

$$\frac{\partial v_x}{\partial x} + \frac{\partial v_y}{\partial y} + \frac{\partial v_z}{\partial z} = 0 \tag{2.2}$$

Momentum equations: Using the law of conservation of momentum, which considers the forces acting on a domain, momentum equations can be written in its nonconservative form as:

$$\rho_m \frac{\partial v_i}{\partial t} + \rho_m v_j \frac{\partial v_i}{\partial x_j} = -\frac{\partial p}{\partial x_i} - \frac{\partial \tau_{ij}}{\partial x_j} + f_i \tag{2.3}$$

where v_i is velocity component in x_i-direction, p is pressure, τ_{ij} is three-dimensional shear stress vector, and f_i is forces i. Given an inviscid, Newtonian fluid the constitutional form of the shear stress τ_{ij} is described in Equation 2.4 with the dynamic viscosity $\mu (kg/sm^2)$, (Laurien and Oertel Jr, 2009).

$$\tau_{ij} = \mu \left(\frac{\partial v_i}{\partial x_j} + \frac{\partial v_j}{\partial x_i} \right) \tag{2.4}$$

Finally, combining both equations results in the momentum equation for incompressible fluids:

$$\rho_m \frac{\partial v_i}{\partial t} + \rho_m v_j \frac{\partial v_i}{\partial x_j} = -\frac{\partial p}{\partial x_i} + \mu \frac{\partial^2 v_i}{\partial x_j^2} + f_i \tag{2.5}$$

Conservation of energy: Conservation of energy is neglected because typical no relevant temperature gradients in the free surface application occur. The interested reader is referred to Hervouet (2007), Chanson (2004), and Laurien and Oertel Jr (2009). In summary, the continuity Equation (2.2) and momentum Equation (2.5) state the Navier-Stokes equations for incompressible fluids in three dimensions. An analytical solution of this equation set is only possible in certain well-defined cases. So far only numerical solutions exist, which are quite time-consuming. In a so-called direct numerical simulation (DNS), the complete temporal and spatial spectrum of the flow is solved but requires enormous computational effort. It is not necessary to resolve the complete spectrum to gain a satisfactory result; rather the influence of turbulence is treated separately from the flow (Laurien and Oertel Jr, 2009).

2.2.2 The Reynolds-Averaged-Navier-Stokes equations

As mentioned above, the full resolution of the Navier-Stokes equation is very complex and only for well-defined cases (like fully developed, laminar flows) a direct solution can be found. In turbulent flows, the field properties become random functions of space and time. Hence, the field variables v_i and p must be expressed as the sum of time-averaged and fluctuating parts as (Figure 2.2):

$$v_i = \bar{v}_i + v_i^+, p = \bar{p} + p^+ \tag{2.6}$$

The time-averaged values at a fixed point in space are given by:

$$\bar{v}_i = \frac{1}{t_1} \int_{t_o}^{t_o+t_1} v_i dt \tag{2.7}$$

Using the mean values over a sufficiently long time interval t_1 , the time-averaged term of the fluctuations equal zero, $\bar{v_i^+} = 0$ and $\bar{p^+} = 0$.

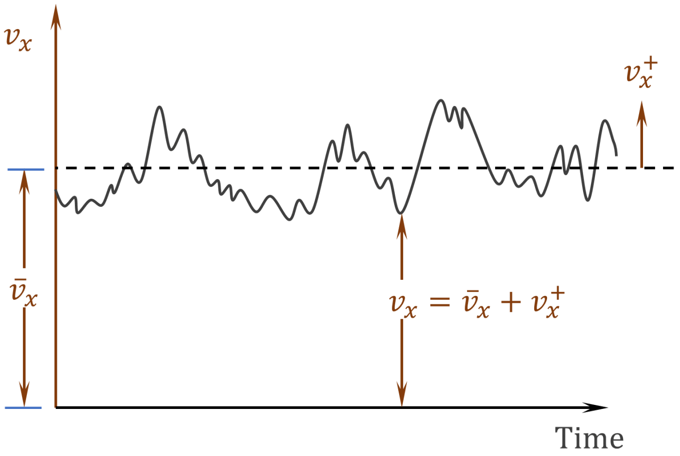

Figure 2.2 Velocity measurements versus time revised from Julien (2010).

Equation 2.6 is inserted into the Navier-Stokes equations to obtain the Reynolds-Averaged Navier-Stokes equations or shortly RANS equations. Here only the final three-dimensional RANS equations are listed, with Equation (2.8) and (2.9) for continuity and momentum, respectively.

$$\frac{\partial \bar{v}_i}{\partial x_i} = 0 \tag{2.8}$$

$$\rho_m \frac{\partial \bar{v}_i}{\partial t} + \rho_m \bar{v}_j \frac{\partial \bar{v}_i}{\partial x_j} = -\frac{\partial \bar{p}}{\partial x_i} + \frac{\partial}{\partial x_i}\left(\mu\left(\frac{\partial \bar{v}_i}{\partial x_j} + \frac{\partial \bar{v}_j}{\partial x_i}\right) - \rho_m \overline{v_i^+ v_j^+}\right) + f_i \tag{2.9}$$

The term $\rho_m \overline{v_i^+ v_j^+}$ is called Reynolds stress tensor ($\tau^{Re} = -\rho_m \overline{v_i^+ v_j^+}$) and must be provided externally by a turbulence model.

2.2.3 The shallow water equations

Shallow water equations (SWE) are a set of hyperbolic partial differential equations (or parabolic if viscous shear is considered) that describe the flow below a pressure surface in a fluid (sometimes, but not necessarily, a free surface). The shallow water equations, also called Saint-Venant equations, are derived from the Navier-Stokes equations under the assumption that the horizontal length scale is much larger than the vertical one. The shallow water equations describe a hydrostatic homogeneous incompressible fluid in response to gravitational and rotational accelerations. The combination of the mentioned assumptions and their application to the Navier-Stokes equations leads to the depth-averaged shallow-water equations for continuity and momentum (Hervouet, 2007):

$$\frac{\partial h}{\partial t}+\frac{\partial hU_x}{\partial x}+\frac{\partial hU_y}{\partial x}=0 \tag{2.10}$$

where U_x and U_y are the depth-averaged quantities of local velocities u_x and u_y.

$$\rho_m\frac{\partial U_i}{\partial t}+\rho_m U_j\frac{\partial U_i}{\partial x_j}=-\rho_m g\frac{\partial h}{\partial x_i}-\frac{\partial}{\partial x_i}\left(\mu\frac{\partial U_i}{\partial x_j}-\rho_m U_i^+U_j^+\right)+f_i \tag{2.11}$$

The term $\rho_m U_i^+U_j^+$ is the disturbing part of the averaged discussion. This is similar to the τ^{Re} in the RANS equations and estimated by a turbulence model.

2.2.4 Governing equation for water flow for rectangular channel

In general, flow hydraulics in a rectangular channel can be described by the 1-D shallow water equations for fluid mass and momentum balance (Parker, 1990b):

$$\frac{\partial h}{\partial t}+\frac{\partial q_w}{\partial x}=0 \tag{2.12}$$

$$\frac{\partial q_w}{\partial t}+\frac{\partial}{\partial x}\left(\frac{q_w^2}{h}\right)=-gh\frac{\partial h}{\partial x}+ghS-C_f u^2 \tag{2.13}$$

where h is the water depth, q_w is the flow discharge per unit width, x is the spatial coordinate along the channel, g is the gravitational acceleration, S is the bed slope, u is the depth-averaged flow velocity, and C_f is the dimensionless resistance coefficient, which is computed using the Manning-Strickler relation:

$$C_f^{-\frac{1}{2}}=\alpha_r\left(\frac{h}{k_s}\right)^{\frac{1}{6}} \tag{2.14}$$

In the above relation α_r is a dimensionless coefficient between 8 and 9 (Parker, 1990b), and k_s denotes a roughness height, related to surface size D_{s90} as:

$$k_s=n_k D_{s90} \tag{2.15}$$

where D_{s90} is the surface grain size such that 90% is finer and n_k is a dimensionless coefficient between 1.5 and 3 (Parker, 1990b). In this study, different values of α_r and n_k are specified for the flume-scale cases and field scale cases, as will be shown later. The mass continuity equation for a rectangular channel is thus simplified in case of steady, gradually varied flow:

$$\frac{\partial h}{\partial t} + \frac{\partial q_w}{\partial x} = 0 \tag{2.16}$$

$$\frac{du}{dx} = \frac{q_w}{h^2}\frac{dh}{dx} \tag{2.17}$$

Momentum conservation reduces to

$$u\frac{\partial u}{\partial x} = -g\frac{\partial h}{\partial x} - g\frac{\partial \eta}{\partial x} - C_f\frac{u^2}{h} \tag{2.18}$$

$$S = -\frac{\partial \eta}{\partial x};\; S_f\; = C_f\mathrm{Fr}^2;\; \mathrm{Fr}^2 = \frac{q_w^2}{gh^3} = \frac{u^2}{gh} \tag{2.19}$$

To get the backwater equation:

$$\frac{\partial h}{\partial x} = \frac{S - S_f}{1 - Fr^2} \tag{2.20}$$

Where Fr denotes the Froude number of the flow and S_f denotes the friction slope. For steady flow over a fixed bed, the backwater equation specified a first-order differential equation in h, requiring a specified value of h at some position as a boundary condition.

2.3 Sediment transport models

There exist many ways that sediment load of a river can be transported. However, The are somewhat arbitrary and not always practical due to the fact not all components are separable in practice (Hickin, 1995):

Dissolved load: Dissolved load is material that entered a solution and becomes part of the fluid flowing through the channel. This does not depend on flow forces in order to keep it in the water column as it is already dissolved (Hickin, 1995).

Suspended-sediment load: The term suspended-sediment load describes the clastic (particulate) material traveling through the channel contained in the water column. The upward flux of turbulence produced at the channel bed force these materials, generally silt and sand, suspended in the flow (Hickin, 1995).

Bed Load (Traction Load): The clastic (particulate) material traveling through the channel entirely supported by the channel bed itself is referred to as bed load. Shear stress at the boundary of the channel bed act to keep these materials (sand, and gravel) in motion (sliding and rolling). Dissimilar to suspended load, the bed-load component is almost always capacity limited (that is, it is a function of hydraulics instead of the supply of material). Many times, a distinction is made between the bed-material load and the bed load. The bed-material load is the sediment load that exists in substantial quantities in the bed (normally > 0.062 mm in diameter) and is then collected when sampling bed-load. It can then be said that the bed material is the origin of this load component and includes rolling and sliding particles (in bed-load transport) as well as those near the bed transported during suspension or saltation. Bed load is therefore just the component of sediment that is supported by the bed (and not by the flow). The term “bed load” denotes a mode of transport and not a material source (Hickin, 1995).

Pore-filling load: Frings, Kleinhans, and Vollmer (2008) introduce another definition of sediment load from a morphological perspective. The pore-filling load is the portion of fines in the sediment load that infiltrates into pores of larger grains if the flow conditions happen to decline.

2.3.1 Theory of incipient motion

For a flow of fluid to begin transporting sediment currently at rest on a surface, the boundary (or bed) shear stress exerted by the fluid must exceed the critical shear stress for the initiation of motion of grains at the bed. This basic criterion for the initiation of motion can be written as:

$$\tau_b = \tau_c \tag{2.21}$$

Bed shear stress (τ_b) is a measure of the force of friction from a fluid acting on a body in the path of that fluid. In the case of open channel flow, it is the force of moving water against the bed of the channel. Shear stress is calculated as:

$$\tau_b = \gamma_s R_H \; |SF| \tag{2.22}$$

γ_s is the specific water weight, R_H is the hydraulic radius, usually equal to the water column h, and the friction term (SF) is defined according to the Manning Theory (Díaz, Fernández-Nieto, and Ferreiro, 2008):

$$SF = \frac{\eta^2 u\,|u|}{R_H^{\frac{4}{3}}} \tag{2.23}$$

η is the Manning coefficient and u is the depth-averaged velocity of the fluid used to calculate the fluid-dynamic forces. After several experiments, Shields obtained an incipient motion diagram, through the non-dimensional shear. As specified by Shields (1936) theory, the movement begins when the shear stress exceeds a critical shear value. Above this value, the current is able to transport the granular sediment. The dominating forces acting on a sediment particle at the river bottom are the bed shear stress τ_b, sediment density ρ_s, fluid density ρ_m, grain diameter d_s, gravity g and the dynamic viscosity μ, (Huston and Fox, 2015). Applying dimensionless analysis on these parameters give two characteristic values as:

$$Re_* = \frac{u_* d_s}{\upsilon_m}; \; Fr_* = \frac{(u_*)^2}{(s-1)\,g d_s} \tag{2.24}$$

where Re_* is grain Reynolds number, Fr_* is grain Froude number, $s = \rho_s/\rho_m$ is relative density, d_s is grain diameter, $u_* = (\tau_b/\rho_m)^{(1/2)}$ is friction velocity and $\upsilon_m = \mu/\rho_m$is kinematic viscosity. Applying the friction velocity relation into Equation 2.24 gives the relation between the Shields parameter and the bed shear stress:

$$\tau_* = \frac{\tau_b}{(\rho_s - \rho_m)\,g d_s} \tag{2.25}$$

The incipient motion condition is expected as $\tau_* > \tau_{*c}$:

$$\tau_{*c} = \frac{\tau_c}{(\rho_s - \rho_m)\,g d_s} \tag{2.26}$$

Based on the analysis of fully developed two-dimensional flows in a laboratory channel and the evaluation of the beginning of sediment motion, a relation between both quantities is derived. Figure 2.3 shows the dependence between Re_* and critical τ_{*c} (Julien, 2010).

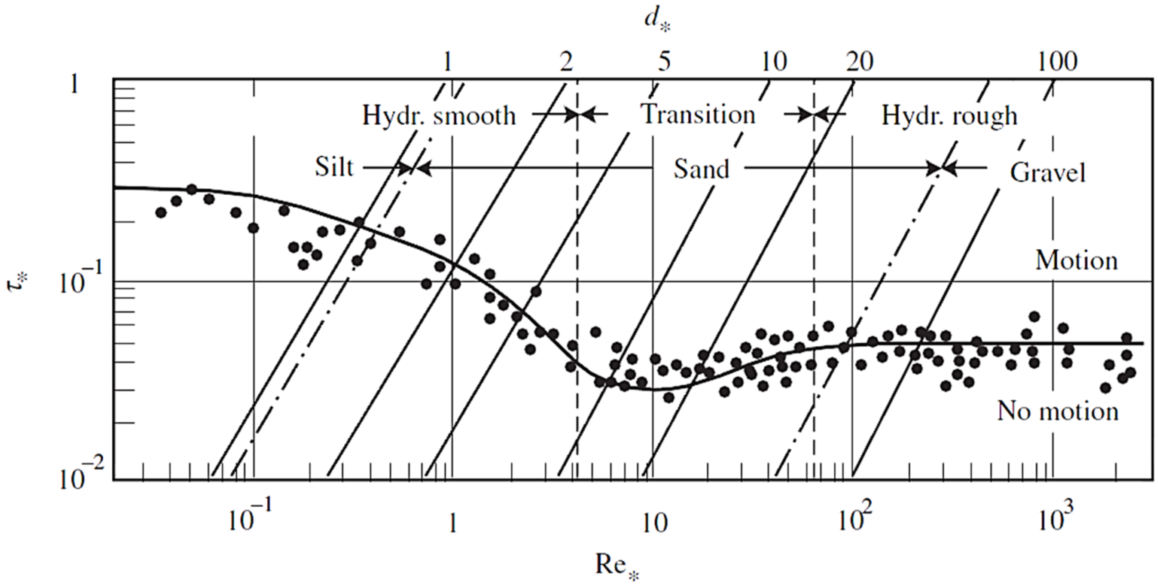

Figure 2.3 Shields diagram for granular material (Julien, 2010). The line represents the incipient movement condition, with respect to the grain-Reynolds number.

The thickness of bed layer is a few grain diameters thick, and $a = 2d_s$ has been commonly used (Figure 2.3). Bed load, or contact load, refers to the transport of sediment particles which frequently maintain contact with the bed. Bedload transport can be treated either as a deterministic or a probabilistic problem. Deterministic methods have been proposed by DuBoys (1879) and Meyer-Peter and Müller (1948) while probabilistic methods were developed by Einstein (1950) and Kalinske (1947).

2.3.2 Bedload transport

Meyer-Peter Müller's equation: The Meyer-Peter Müller's equation is probably the most widely applied equation in both basic research and engineering applications among numerous available semi-theoretical bedload transport equations. Meyer-Peter and Müller (1948) developed a complex bedload formula for gravels based on the mean sediment size d_{50} of the surface layer of the bed material. Chien (1956) demonstrated that the elaborate original formulation can be reduced in the following simple equation:

$$q_b^* = 8(\tau^* - \tau_c^*)^{3/2}; \tau_c^* = 0.047 \tag{2.27}$$

This equation is most appropriate for channels with large width-depth ratios and for grain diameters in the range of $0.4\ mm < d_{50} < 29\ mm$.

Einstein-Brown's equation: Einstein (1941) made the seminal contribution to bedload sediment transport. He introduced the idea that grains move in steps proportional to their size. He defined the bed layer thickness as twice the particle diameter. He extensively used probability concepts to formulate a relationship for contact sediment discharge.

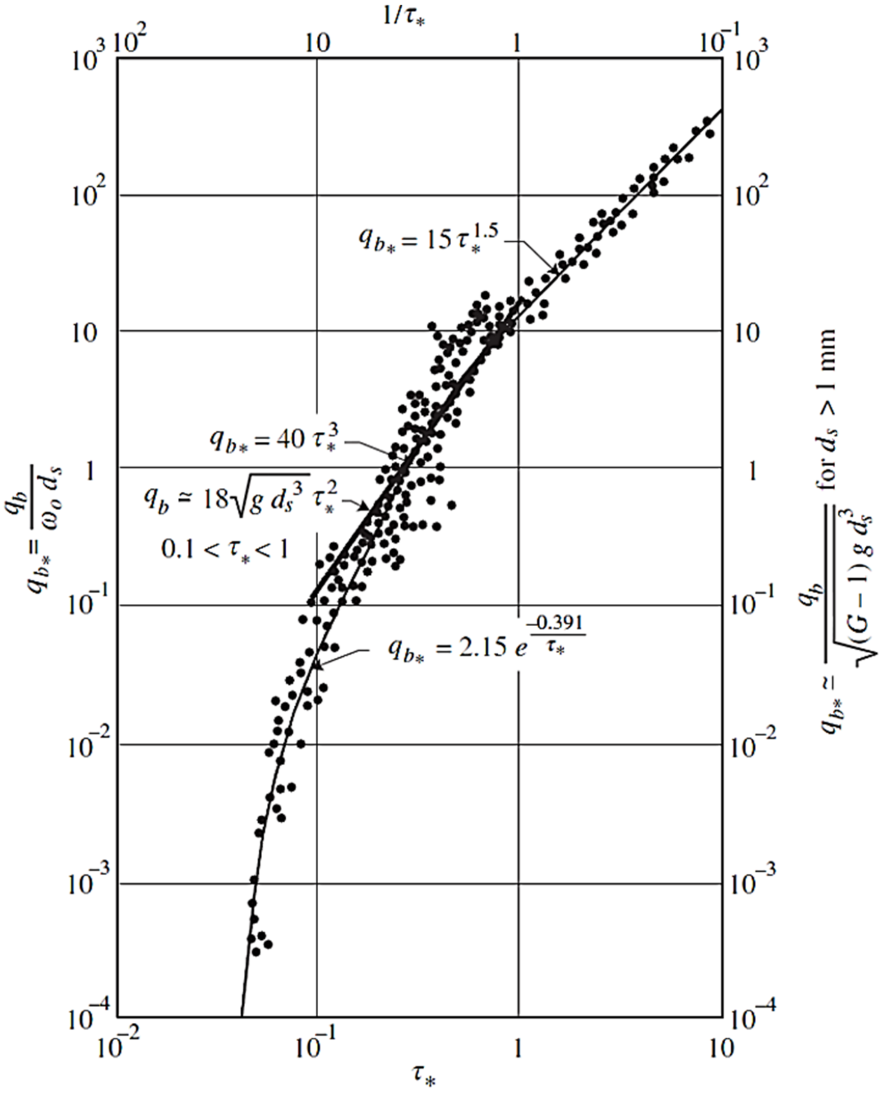

Figure 2.4 Dimensionless sediment discharge q_{b*} versus Shields parameter τ_* (Julien, 2010).

The sediment discharge q_b in the volume of sediment per unit width and time (q_b in L^2/T) is transformed, using Rubey's clear water fall velocity ω_o, into a dimensionless volumetric unit sediment discharge q_{b*} as:

$$q_{b*} = q_b \left(\sqrt{(s-1)\, g d_s^3} \left\{ \sqrt{\frac{2}{3} + \frac{36 \nu_m^2}{(s-1)\, g d_s^3}} - \sqrt{\frac{36 \nu_m^2}{(s-1)\, g d_s^3}} \right\} \right)^{-1} \tag{2.28}$$

Figure 2.4 shows the dimensionless rate of sediment transport q_{b*} as a function of the Shields parameter $\tau* = \tau_b/(\rho_s - \rho_m) g d_s$, with measurements from Bogárdi and Bogárdi (1974), Kalinske (1947), and Wilson and Geankoplis (1966). Brown (1950) suggested the following two relationships:

$$\begin{cases} q_{b*} = 2.15 e^{\frac{-0.319}{\tau_*}} \ when\ \tau_* \ < \ 0.18 \\ q_{b*} = 40 \tau_*^3 when\ 0.52 \ > \ \tau_* > \ 0.18 \end{cases} \tag{2.29}$$

Considering sediment transport data at high shear rates $\tau_* > 0.52$ one obtains:

$$q_{b*} = 15 \tau_*^{1.5} when \ \ \tau_* > 0.52 \tag{2.30}$$

This third approximation is not very accurate at such high shear rates, however, because large quantities of sediment will move in suspension that were not considered in this research.

2.3.3 Surface-based bed load equation

The significantly different sizes of fine sediment and coarse bed material lead to the dissimilarities in transport rate of each size fraction. A substrate-based bed load transport relation can be used for gross predictions of sediment transport in gravel-bed Rivers (Parker, 1990a). Consider the bed load transport of a mixture of sizes. The thickness E_a of the active (surface) layer of the bed with which bed load particles exchange is given by as

$$E_a = n_a D_{s90} \tag{2.31}$$

where D_{s90} is the size in the surface (active) layer as 90 percent of the material is finer, and n_a is an order-one dimensionless constant (in the range $1 \sim 2$). Divide the bed material into N grain size ranges, each with characteristic size D_j, and β_j denotes the fraction of material in the surface layer in the j^{th} size range (Parker, 1990a). The volume bed load transport rate per unit width of sediment in the j^{th} grain size range is denoted as q_{bj}. The total volume bed load transport rate per unit width is denoted as q_{bT}, and the fraction of bed load in the j^{th} grain size range is β_j:

$$q_{bT} = \sum_{j=1}^{N} q_{bj}, \ \beta_j = \frac{q_{bj}}{q_{bT}} \tag{2.32}$$

where τ^*, q^* and W^*, denote the dimensionless grain size specific Shields number τ_j^*, grain size specific Einstein number q_j^* and dimensionless grain size specific bedload transport rate W_j^*.

$$\tau_j^* \equiv \frac{\tau_b}{\rho_m R g D_j} = \frac{u_*^2}{R g D_j}, \ q_{bj}^* = \frac{q_{bj}}{\sqrt{R g D_j} D_j \beta_j}, \ W_j^* \equiv \frac{q_{bj}^*}{(\tau_j^*)^{3/2}} = \frac{R g q_{bj}}{(u_*)^3 \beta_j} \tag{2.33}$$

Assuming that a functional relation exists between $q_j^*(W_j^*)$ and τ_j^*:

$$q_{bj}^* = \frac{q_{bj}}{\sqrt{R g D_j} D_j \beta_j} = f_q(\tau_j^*), \ W_j^* = \frac{R g q_{bj}}{(u_*)^3 \beta_j} = f_W(\tau_j^*) \tag{2.34}$$

The bed load transport rate of sediment in the j^{th} grain size range is given as:

$$q_{bj} = \beta_j \sqrt{R g D_j} D_j f_q(\tau_j^*), \ q_{bj} = \beta_j \frac{u_*^3}{R g} f_W(\tau_j^*) \tag{2.35}$$

In case the grain size range is not represented in the surface (active) layer, it will not be represented in the bed load transport as specified by this formulation (Parker, 1990a).

2.3.3.1 Bed load relation for mixtures according to Parker (1990a, b)

Parker (1990a) used the empirical data to determine a surface-based bed load transport formula. The method is based on surface geometric size D_{sg} and surface arithmetic standard deviation σ_s on the ψ scale, both computed from the renormalized fractions β_j.

$$W_j^* = 0.00218 G\left(\varphi_j\right) \tag{2.36}$$

Where:

$$\varphi_j = \omega \varphi_{sgo} \left(\frac{D_j}{D_{sg}}\right)^{-0.0951}, \ \varphi_{sgo} = \frac{\tau_{sg}^*}{\tau_{ssrg}^*}, \ \tau_{sg}^* = \frac{u_*^2}{R g D_{sg}}, \ \tau_{ssrg}^* = 0.0386 \tag{2.37}$$

$$G(\varphi) = \begin{cases} 5474\left(1 - \frac{0.853}{\varphi}\right)^{4.5} \varphi > 1.59 \\ \exp\left[14.2(\varphi - 1) - 9.28(\varphi - 1)^2\right] \; for \; 1 \leq \varphi \leq 1.59 \\ \varphi^{14.2} \; for \quad \varphi < 1 \end{cases} \tag{2.38}$$

$$\omega = 1 + \frac{\sigma_s}{\sigma_o\left(\varphi_{sgo}\right)}\left[\omega_o\left(\varphi_{sgo}\right) - 1\right] \tag{2.39}$$

$$D_{sg} = 2^{\bar{\psi}_s}, \;\; \bar{\psi}_s = \sum_{j=1}^{N} \psi_j \beta_j, \; \sigma_s^2 = \sum_{j=1}^{N} \left(\psi_j - \bar{\psi}_s\right) \tag{2.40}$$

The functions $\sigma_o(\varphi_{sgo})$ and $\omega_o(\varphi_{sgo})$ are specified in Figure 2.5. More detail about the tables for these functions are given in Parker (1990b), along with a DOS implementation of the above method.

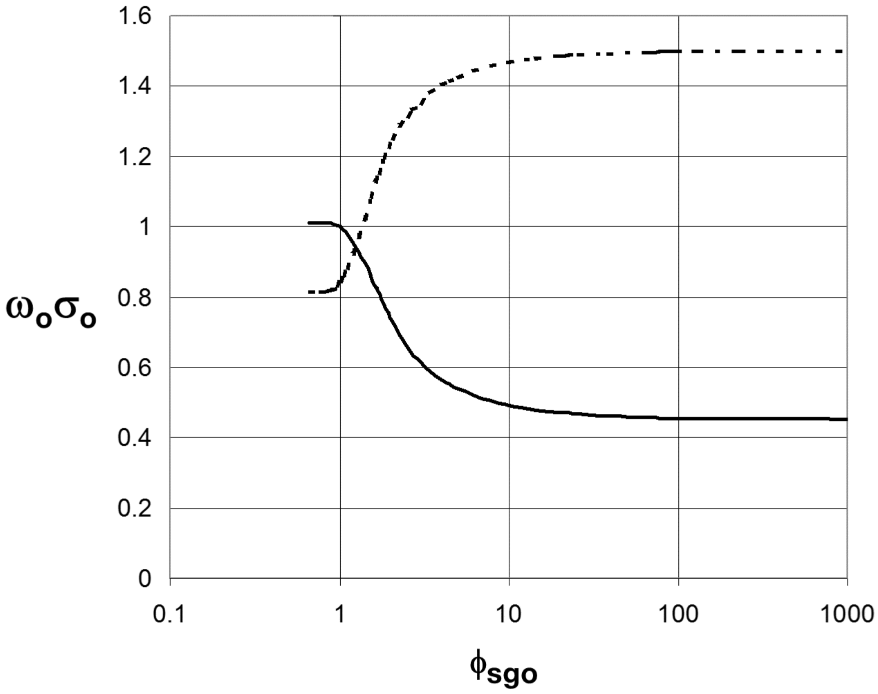

Figure 2.5 Plots of the functions $\sigma_o(\varphi_{sgo})$ and $\omega_o(\varphi_{sgo})$ for the Parker (1990a) relation.

Sequences of bed load calculation proposed by Parker (1990a) with the above relationships proceed as follows. The grain sizes and fractions (D_j, β_j) of the surface layer (from which the sand has been excluded), submerged specific gravity of the sediment R and shear velocity associated with skin friction u_* must be specified. The surface geometric grain size D_{sg} and arithmetic standard deviation σ_s are computed from Equation (2.40), in which the percent of finer (p_j) is calculated from the updated fraction (β_j). The Shields number τ^*_{sg} is computed with Equation (2.37). The values of W^*_j and q_{bj} are then obtained from Equation (2.36), (2.35). The total bed load transport rate per unit width q_{bT} and fraction bedload in the jth grain size range β_j are then calculated from Equation (2.32).

2.3.3.2 Bedload relation for mixtures according to Wilcock and Crowe (2003)

The surface-based relation of Wilcock and Crowe (2003a) generalizes the two-grain method of Wilcock and Kenworthy (2002) to an arbitrary number of grain size ranges of both gravel and sand. The dimensionless grain size specific bedload transport rate W^*_j is calculated by following equation.

$$W^*_j = \begin{cases} 0.002\phi^{7.5} & \phi < 1.35 \\ 14\left(1 - \frac{0.894}{\sqrt{\phi}}\right)^{4.5} & \phi \geq 1.35 \end{cases} ;\ \phi = \frac{\tau_b}{\tau_{rj}};\ j = 1,2,...,N \tag{2.41}$$

in which τ_b denotes bed shear stress, and τ_{rj} $(j = 1,2,...,N)$ is defined as the reference shear stress for sand and for the j^{th} size group of the gravel class, respectively (to be discussed in more detail below), W^*_j denotes dimensionless transport rate for the j^{th} size group of the gravel class, as defined below:

$$q^*_{bj} = \frac{q_{bj}}{D_j \beta_j \sqrt{RgD_j}},\ W^*_j = \frac{Rgq_{bj}}{(u_*)^3 \beta_j} \tag{2.42}$$

in which R denotes submerged specific weight of sediment particles, g denotes gravitational acceleration, u_* denotes shear velocity.

Values of τ_{rj} are scaled by τ_{rsg} for each mixture is a function of D_j/D_{sg} (Wilcock and Crowe, 2003a):

$$\frac{\tau_{rj}}{\tau_{rsg}} = \left(\frac{D_j}{D_{sg}}\right)^b;\ b = \begin{cases} \frac{0.67}{1+exp\left(1.5-\frac{D_i}{D_{sg}}\right)} & \frac{D_i}{D_{sg}} \geq 1 \\ \frac{0.12}{1+exp\left(1.5-\frac{D_i}{D_{sg}}\right)} & \frac{D_i}{D_{sg}} < 1 \end{cases} \tag{2.43}$$

$$\phi = \frac{\tau_b}{\tau_{rj}} = \frac{\tau_b}{\tau_{rsg}} \left(\frac{D_j}{D_{sg}}\right)^{-b} = \frac{\tau^*}{\tau^*_{rsg}} \left(\frac{D_j}{D_{sg}}\right)^{-b} \tag{2.44}$$

in which τ_{rsg} denotes a surface geometric mean-based reference shear stress, and D_{sg} denotes the geometric mean grain size of the surface layer (including both sand and gravel classes). On the basis of flume experimental data, Wilcock and Crowe (2003b) that surface geometric mean-based reference shear stress, τ^*_{rsg}, decreases with the increase in surface sand fraction (β_s):

$$\tau^*_{rsg} = \frac{\tau_{rsg}}{\rho_m R g D_{sg}} = 0.21 + 0.15 exp\left(-20\beta_s\right) \tag{2.45}$$

Similar to calculation sequences of Parker (1990a), Wilcock and Crowe (2003b) proposed the bed load calculation sequences as follows: the grain sizes and fractions (D_i, β_j) of the surface layer, submerged specific gravity of the sediment R and shear velocity associated with skin friction u_* must be specified. The surface geometric mean size D_g is computed from the fractions finer in the surface material and τ^*_{rsg} is evaluated from Equation (2.45). The fraction (β_s) of the surface material is computed from the fractions β_j. The values of W^*_j and q_{bj} are then obtained from Equation (2.40), (2.35). The total bed load transport rate per unit width q_{bT} and fraction bedload in the j^{th} grain size range β_j are then computed from Equation (2.32).

2.3.4 Bed evolution

The morphological evolution of the bed is defined mathematically by the so-called sediment continuity or Exner equation. This equation simply states that the time rate of change of the bed elevation is equal to the divergence of the sediment flux, which can be expressed in terms of the local flow properties through the use of an empirical sediment transport formulae (Kubatko, Westerink, and Dawson, 2006). In the case of the mobile bed, it is necessary to describe the movement of the granular sediment with an appropriate equation. The solid concentration is defined as:

$$c = \frac{V_s}{V} \tag{2.46}$$

where V_s is the solid volume and V the total volume. The rates of bed level changes are calculated from the equation of conservation of sediment mass. In two dimensions, this is written as:

$$(1 - p)\frac{\partial z}{\partial t} + \left(\frac{\partial q_x}{\partial x} + \frac{\partial q_y}{\partial y}\right) = (1 - p)\frac{\partial (c\rho_s)}{\partial t} \tag{2.47}$$

where z is bed level, x and y are horizontal space coordinates, t is time, p is porosity, and q_x and q_y are sediment transport rates in x and y directions. The term on the right side of the equation denotes the variation of the solid materials concentration in the control volume, where ρ_s is the sediment density. Assuming that the solid concentration is constant, the equation becomes:

$$(1 - p)\frac{\partial z}{\partial t} + \left(\frac{\partial q_x}{\partial x} + \frac{\partial q_y}{\partial y}\right) = 0 \tag{2.48}$$

Equation (2.48) is known as the Exner equation. In this equation, the transport rates q_x and q_y are functions of several parameters, namely current waves water depth and sediment properties. Within a morphological time step (time step used in solving Equation (2.48), the following at each grid point is assumed: sediment properties are fixed, currents and waves locally varies with water depth, and water level is at a fixed level above datum. Under these assumptions, the transport rate vary only with the bed level and Equation (2.48) can be written as an advection equation as:

$$(1 - p)\frac{\partial z}{\partial t} + \left(\frac{\partial q_x}{\partial z}\frac{\partial z}{\partial x} + \frac{\partial q_y}{\partial z}\frac{\partial z}{\partial y}\right) = 0 \tag{2.49}$$

$$or\ \frac{\partial z}{\partial t} + C_x(z)\frac{\partial z}{\partial x} + C_y(z)\frac{\partial z}{\partial y} = 0 \tag{2.50}$$

here $C_x(z)$ and $C_y(z)$ are the x and y components of the bed celerity, which also depend on the bed level. Equation (2.50) shows that morphological evolution occurs as non-linear propagation of the bed level deformations in the direction of the transport. The Exner equation needs a model for the sediment transport, originating from the theory of incipient motion developed by Shields (1936).

2.3.5 Interfacial exchange fractions

Sediment transports between the surface layer and substrate when the bed aggrades or degrades. The substrate is transferred into the surface layer as the bed degrades (Figure 2.6).

Hirano (1971) was one of the first to recognize this (Toro-Escobar, Parker, and Paola, 1996). To formulate the sediment exchange problem, the range of grain sizes are divided into N subranges $j = 1 \ldots N$ while $\beta_{a,j}(x,t)$ denote the mass fraction content in the surface layer at streamwise point x and time t, as shown in Figure 2.6. The flow and bed are assumed to be uniform in the transverse direction. The substrate size distribution has a vertical as well as streamwise structure; fraction content in the substrate is denoted as $\beta_{s,j}(x,z,t)$ where z denotes a vertical coordinate. The size distribution at the interface between the surface and substrate, which expresses the transfer of material as the bed degrades or aggrades, is denoted as $\beta_{l,j}(x,t)$ (Toro-Escobar, Parker, and Paola, 1996).

For the case of degradation ($\partial z/\partial t < 0$), the Hirano (1971)'s assumption can be expressed as follows:

$$\beta_{I,j} = \beta_{a,j}\,(x,t) \tag{2.51}$$

This would imply that the deposited substrate is identical in grain size distribution with the surface layer just above it (Toro-Escobar, Parker, and Paola, 1996).

In contrast to the field observation that the surface layer is usually systematically coarser than the substrate in gravel-bed streams (Dietrich et al., 1989), Parker (1990b) and Parker (1990a) tested an alternative assumption, according to which the bed load is transferred directly to the substrate deposition:

$$\beta_{I,j} = \beta_{b,j}\,(x,t) \tag{2.52}$$

$\beta_{b,j}$ here denotes the mass fractional content of the j^{th} size range in the bed load.

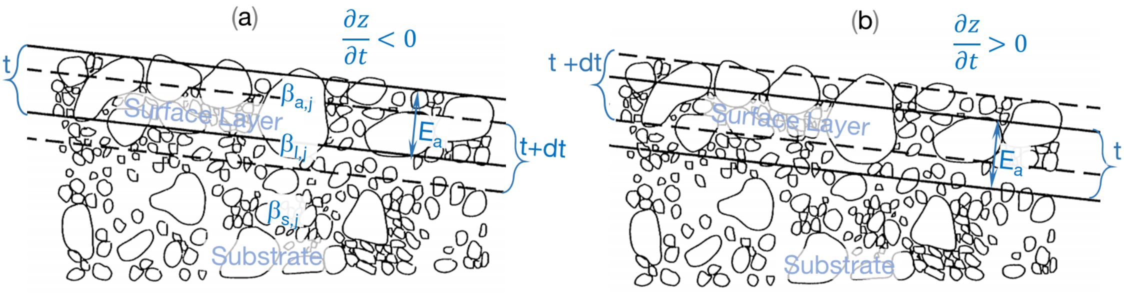

Figure 2.6 The transfer of sediment in bed degrades (a) and bed aggrades (b) revised from Toro-Escobar, Parker, and Paola (1996).

Toro-Escobar, Parker, and Paola (1996) combined these above assumptions to develop the transfer function for poorly sorted gravel during aggradation process. The hypothesis in this function is that the transfer fractions for the case of an aggrading bed can be specified in terms of some weighted average of the two:

$$\beta_{I,j} = \frac{c_j \beta_{b,j} + \left(1 - c_j\right) \beta_{a,j}}{\sum_{j=1}^{N} \left[c_j \beta_{b,j} + \left(1 - c_j\right) \beta_{a,j}\right]} \tag{2.53}$$

where c_j is a coefficient that could be a function of flow parameters. The above equation represents a generalization of one suggested by Hoey and Ferguson (1994). The normalization in the denominator is to ensure that $\beta_{I,j}$ always sums to 1. The coefficients are presumed to be positive and within the interval [0,1]. In order to empirically determine a relation, it is necessary to have data for the transfer, surface and bed load fractions $\beta_{a,j}$ and $\beta_{b,j}$ (Toro-Escobar, Parker, and Paola, 1996).

2.4 Numerical methods

Numerical analysis is the study of algorithms that use numerical approximation (as opposed to symbolic manipulations) for the problems of mathematical analysis (as distinguished from discrete mathematics). Flow and sediment transport are described by a coupled system of equations for hydrodynamic and morphodynamic systems which represent nonlinear hyperbolic partial differential equations and analytical solutions of these equations are not possible except for a few simplified cases. Therefore, they are often solved by numerical schemes where the continuous description of the equations is transferred into a set of discrete expressions in time and space (Rodi, Constantinescu, and Stoesser, 2013; Pletcher, Tannehill, and Anderson, 2012).

2.4.1 Spatial discretization

2.4.1.1 Finite Difference Method (FDM)

The finite difference method uses Taylor series expansions to derive difference quotient expressions for the derivatives at discrete grid points, expressing them through variable values at neighboring grid points (Rodi, Constantinescu, and Stoesser, 2013). This is explained here by reference to a one-dimensional variable distribution as shown in Figure 2.7.

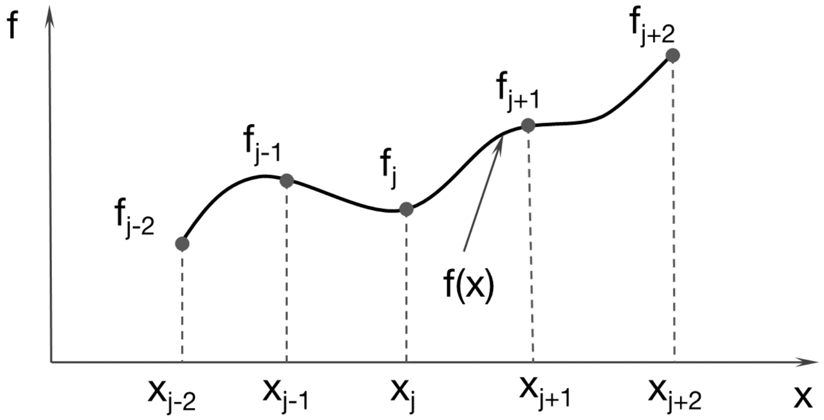

Figure 2.7 Finite difference computational stencils for 1 D problems revised from Rodi, Constantinescu, and Stoesser (2013).

In Figure 2.7, a continuous function $f(x)$ can be represented as a series of discrete values f_j at discrete points (j). The value f_{j+1} at point $(j+1)$ can be expressed in terms of a Taylor series expanded about point (j) as:

$$f_{j+1} = f_j \; + \; \frac{\partial f}{\partial x}|_j (\Delta x)^1 + \frac{\partial^2 f}{\partial x^2}|_j \frac{(\Delta x)^2}{2} + \frac{\partial^3 f}{\partial x^3}|_j \frac{(\Delta x)^3}{6} + \ldots \tag{2.54}$$

Equation (2.54) is exact if an infinite number of terms on the right-hand side is retained and/or if $\Delta x \to 0$. The accuracy of Equation (2.54) depends on which terms are neglected. With Equation (2.54) and similar Taylor series expansions for other neighboring points, we can derive the following approximations:

$$1^{st} \; order \; \frac{\partial f}{\partial x}|_j \; = \frac{f_{i+1} - f_i}{\Delta x} + \Gamma_1; \; 2^{nd} \; order \; \frac{\partial f}{\partial x}|_j \; = \frac{f_{i+1} - f_{i-1}}{2\Delta x} + \Gamma_2 \tag{2.55}$$

The above equation presents the first-order forward or upwind difference and the second-order central difference approximations Equation (2.54). The truncation term Γ_1 represents the higher-order terms not accounted for in the difference approximations and is the difference between the exact solution of the derivative and its discrete approximations.

An advantage of this method is its easy implementation to numerical solvers. However, FDM need the computational grid to be structured, a common restriction when dealing with complex, three-dimensional geometries. This limitation can be relieved by using multi-block grids or by using the FDM on curvilinear coordinates (Rodi, Constantinescu, and Stoesser, 2013). However, when we encounter irregular geometries, complex grids, or an unusual specification of boundary conditions, finite difference techniques become difficult to apply.

2.4.1.2 Finite Volume Method (FVM)

The FVM offers an alternative approach for deriving the discretized equations. This method is based on the principle that the divergence term, which frequently occurs in differential equations governing various interesting scientific phenomena, can be rewritten as a surface integral using the divergence theorem. The FVM is integrated over a finite number of Control Volumes (CV) that comprise the flow domain. Based on the balance for each CV, the rate of change of a quantity in the CV is sum of its flux through the CV faces, and in the case of momentum also of pressure forces acting on the CV faces and volume forces (Rodi, Constantinescu, and Stoesser, 2013).

Consider the general 1 D unsteady convection-diffusion equation (without source terms):

$$\frac{\partial f}{\partial t} + u\frac{\partial f}{\partial x} = \Gamma\frac{\partial^2 f}{\partial x^2} \tag{2.56}$$

where: u is the velocity, Γ is the diffusion coefficient, u and Γ are assumed constant. The 1-D finite volume domain with the CV around node P (Figure 2.8), for which integration between west and east yields:

$$\int_w^e \frac{\partial f}{\partial t}dx + \int_w^e u\frac{\partial f}{\partial x} = \int_w^e \Gamma\frac{\partial^2 f}{\partial x^2} \tag{2.57}$$

$$\frac{\partial}{\partial t}\left(\frac{1}{\Delta x}\int_w^e f dx\right)\Delta x + u\left[f_e - f_w\right] = \Gamma\left[\frac{df}{dx}|_e - \frac{df}{dx}|_w\right] \tag{2.58}$$

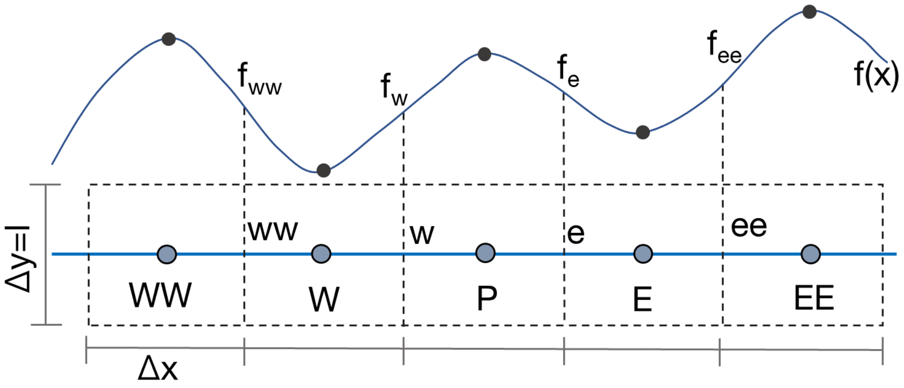

Figure 2.8 Finite volume computational stencils for 1 D problems revised from Rodi, Constantinescu, and Stoesser (2013).

In the Equation (2.58), the first term represents the rate of change of the average quantity $\bar{f}$ in the CV, the second and third term (net convective flux (C) and net diffusive flux (D)) are expressed as the surface fluxed through the two CV face denote e and w (for east and west). For uniform grid and linear interpolation using the nodal value of neighboring, the convective flux is calculated by the following equation:

$$C = u\left[f_e - f_w\right] = u\left[\frac{f_E + f_P}{2} - \frac{f_P + f_W}{2}\right] = u\Delta x\left[\frac{f_E - f_W}{2\Delta x}\right] \tag{2.59}$$

The net diffusive for uniform grid spacing:

$$D = \Gamma\left[\frac{df}{dx}|_e - \frac{df}{dx}|_w\right] = \Gamma\left[\frac{f_E - f_P}{2} - \frac{f_P - f_W}{2}\right] = \Gamma\Delta x\left[\frac{f_W - 2f_P + f_E}{2\Delta x}\right] \tag{2.60}$$

The advantage of FVM is its automatic conservation of the quantity considered because this method is based on the flux-balance where the outflow from one cell becomes inflow into another. This makes the FVM stable and flexible, yet relatively easy to implement. This is why the FVM is commonly implemented in commercial computational fluid dynamics (CFD) solvers (Pletcher, Tannehill, and Anderson, 2012; Rodi, Constantinescu, and Stoesser, 2013).

2.4.2 Time discretization

Similar to the discretization in space, the discretization of the time derivative using finite differences is an approximation analogous to the first-order expression. Equation (2.54) can, for instance, be derived from a Taylor series as:

$$\frac{\partial f}{\partial x}|_j = \frac{f_{i+1} - f_i}{\Delta x} + \Gamma_1 \tag{2.61}$$

where Δt is time step, f_n is the value of f at time t_n, f_{n+1} is the yet unknown value of f at time t_{n+1} and Γ_1 is the truncation error. The simplest time discretization schemes are explicit and implicit Euler methods, in which variable f_{n+1} is calculated from:

$$\frac{f_{n+1} - f_n}{\Delta t} = rhs^n; \ \frac{f_{n+1} - f_n}{\Delta t} = rhs^{n+1} \tag{2.62}$$

Euler methods can be considered as the analogs of forward and backward differencing in space and are first-order accurate in time. Euler methods are called two-point methods because the value of at two instances in time is involved. A second-order accurate two-point method can be constructed by applying the trapezoidal rule to approximate *rhs*, which yields the semi-implicit Crank-Nicolson method:

$$\frac{f_{n+1} - f_n}{\Delta t} = \frac{1}{2}\left(rhs^n + rhs^{n+1}\right) \tag{2.63}$$

The explicit Euler method provides very fast computational results, but suffers from instability for inappropriate time steps or grid resolutions. Therefore, explicit time discretization methods are subject to rigorous stability conditions, which are generally known as the CFL condition (Courant-Friedrichs-Levy conditions):

$$CFL = \frac{|u|\,\Delta t}{\Delta x} < 1 \tag{2.64}$$

where u is characteristic velocity, and Δx is grid resolution.

2.4.3 Numerical solutions

The numerical solution of the system consisting of two hydrodynamic and one sediment equation is non-trivial. Cunge, Holly, and Verwey (1980) examined two useful ways for describing any sediment transport flux that is a function of only flow velocity. Both approaches, however, are adaptable for any sediment transport flux but with varying degrees of difficulty (Hudson and Sweby, 2005).

Decoupled approach: The water motions are assumed to be steady with respect to changes in the bed level for the decoupled approach. Alternatively put, the timescale over for which the bed changes are so much longer than those of the hydrodynamic motions that these individual motions do not invoke bed changes: only the mean hydrodynamic effect responds to bed changes. In other words, the propagation speed of the bed waveforms (like ripples or tidal sand waves) is considerably slower than the wave speeds of the flowing water. These assumptions enable the water flow to be separately discretized from the bed. Moreover, the approach takes advantage of the slow bed evolution by iterating the water flow to a state of equilibrium every update of the bed. The quasi-stationary assumption is introduced numerically by iterating to a state where the time derivatives are equal to zero. By doing so, the computation time is substantially reduced for test cases where the bed evolves slowly (Hudson and Sweby, 2005).

$$\begin{bmatrix} h \\ uh \end{bmatrix}_t + \begin{bmatrix} uh \\ hu^2 + \frac{1}{2}\ gh^2 \end{bmatrix}_x = \begin{bmatrix} 0 \\ -ghz_x \end{bmatrix} \tag{2.65}$$

Coupled approach: No assumptions are made and water flow and bed changes are computed simultaneously in the coupled approach. This approach allows for the water motions to either be steady or unsteady and bed level changes are significant. Here the sediment continuity equation's wave speed can be similar to the wave speeds of the water flow. The system is discretized simultaneously when following this approach (Hudson and Sweby, 2005).

$$\begin{bmatrix} h \\ uh \\ z \end{bmatrix}_t + \begin{bmatrix} uh \\ hu^2 + \frac{1}{2}\ gh^2 \\ \frac{1}{1-p} \end{bmatrix}_x = \begin{bmatrix} 0 \\ -ghz_x \\ 0 \end{bmatrix} \tag{2.66}$$

Both approaches discussed above can be written in the general form:

$$\frac{\partial \vec{w}}{\partial t} + \frac{\partial F(\vec{w})}{\partial x} = \vec{R} \tag{2.67}$$

where $F(\vec{w})$ is the numerical flux and $\vec{R}$ contains the inhomogeneous term. To solve the system (2.66) the continuous equations must be discretized to represent the finite number of grid points that exist. Using the upwind scheme, this discretization takes the form:

$$\vec{W}_i^{t+1} = \vec{W}_i^t - \frac{\Delta t}{\Delta x}(\vec{F}_{i-1}^t - \vec{F}_i^t) + \frac{\Delta t}{\Delta x}\vec{R}_i \tag{2.68}$$

The upwind scheme, an example of an explicit scheme, is the solution at the next time-step $t+1$ can be derived explicitly from the quantities known at the previous time-step t. This is to in contrast to with an implicit scheme where the differential equation of the finite differences has terms at the new time step $t+1$.

The points $x = x_o$ and $x = x_i$ are the spatial boundaries that require numerical boundary conditions . The spatial step size (Δx) is fixed and the time step is variable (Hudson and Sweby, 2005).

$$\Delta t = \frac{v\Delta x}{max(|\lambda_k|)} \tag{2.69}$$

where $max(|\lambda_k|)$ is the maximum wave speed, λ_k are the eigen values of the Jacobian matrix associated with the system,

$$A(\vec{w}\ ) = \frac{\partial \vec{F}}{\partial \vec{w}} \tag{2.70}$$

where k is the k-th component of the system and v is the required Courant number. Unless otherwise stated, the scheme presented is considered stable for Courant number less than one. The value λ_k corresponds to the travel speeds of information in the general system (2.67), (2.69) ensures time steps are small enough so that waves cannot propagate farther than its adjacent cell in one integration, as is consistent with the numerical scheme (2.68). Therefore, this is a major reason for why most morphodynamic codes prefer the decoupled approach, as the hydrodynamical wave speeds are normally much greater than the morphodynamical ones. This results in time steps orders of magnitude smaller and correspondingly slower performing codes. The decoupled approach is advantageous for the reason that any sediment transport flux, or even a black-box approach, is easy to implement, whereas in the coupled approach difficulties can arise when involving transport fluxes of sediment that are more complex (Hudson and Sweby, 2005). In Hudson (2001) and Rezzolla (2011), one can find additional information regarding numerical methods for morphodynamic modelling and their solution.

2.4.4 Stability, consistency, and convergence of numerical discretization

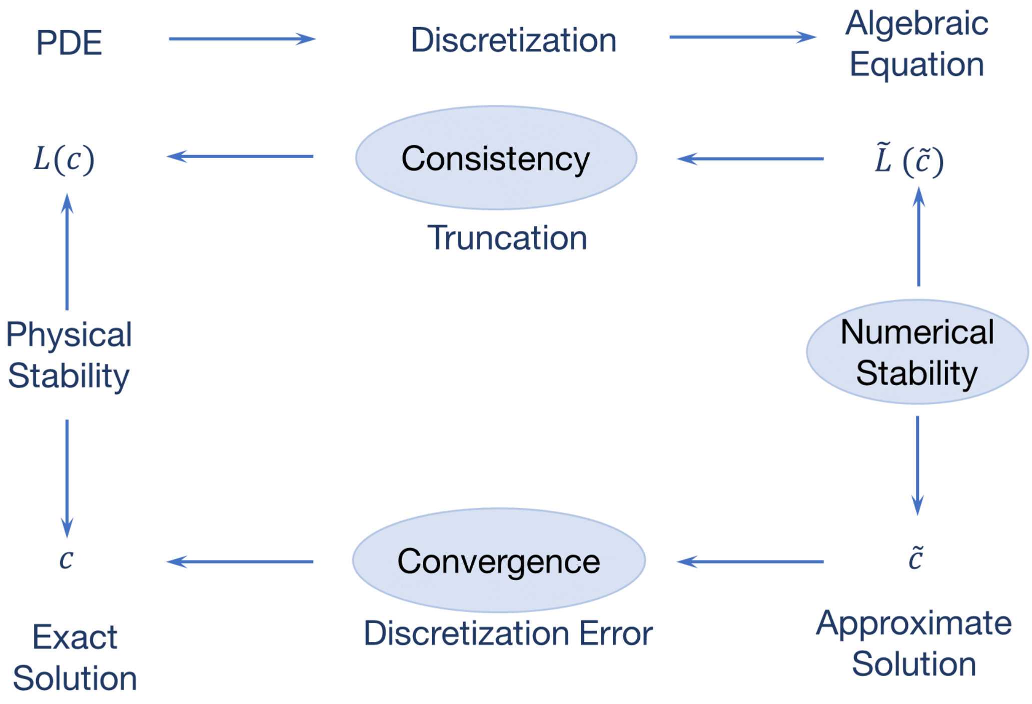

Figure 2.9 The error in discretization.

The errors in a discretization are the difference between the solution of the original problem and the solution of the discrete problem. These must be defined so that the difference makes sense and can be quantified (Figure 2.9) including:

Consistency: The discrete equation approaches the differential one, as the increments in the independent variables vanish.

Stability: A stable numerical scheme prevents the unlimited growth of numerical error during calculation.

Convergence: The discrete solution approaches the true solution to the partial differential equation as the increments go to zero.

Chapter 3

Fine sediment exchange and porosity variation in gravel-bed Rivers

3.1 Overview

Fine sediment infiltration into void spaces of coarse bed material can potentially alter river morphodynamics and aquatic ecosystems. As a result of the fine sediment exchange in void space process, the ratio of the remaining void volume over the total volume of a gravel-bed, the porosity is varying (Frings, Kleinhans, and Vollmer, 2008; Nunez-Gonzalez, Martin-Vide, and Kleinhans, 2016). Figure 3.1 shows a qualitative dependency between the bed porosity and fine size fraction, as well as their influence on the infiltration process (based on Nunez-Gonzalez, Martin-Vide, and Kleinhans (2016)). In which, porosity is reached the minimum value when the fine sediment is completely filled in the void space of gravel bed.

The background of the fine sediment infiltration and the porosity variation are included as two main parts of this chapter. In each main part, the literature review and the fundamental definition are introduced as a preamble. The theoretical and experimental approaches for calculating the fine sediment distribution (the first part) and porosity variation (the second part) are presented respectively.

Parts of this chapter were published as:

Bui, V.H.; Bui, M.D.; Rutschmann, P. Advanced Numerical Modeling of Sediment Transport in Gravel-Bed Rivers. Water 2019, 11, 550, doi:10.3390/w11030550.

Bui, V.H.; Bui, M.D.; Rutschmann, P. Modeling infiltration process of fine sediment in gravel bed river. Proc. of Wasserbau-Symposium. 2018, 419-426, Austria.

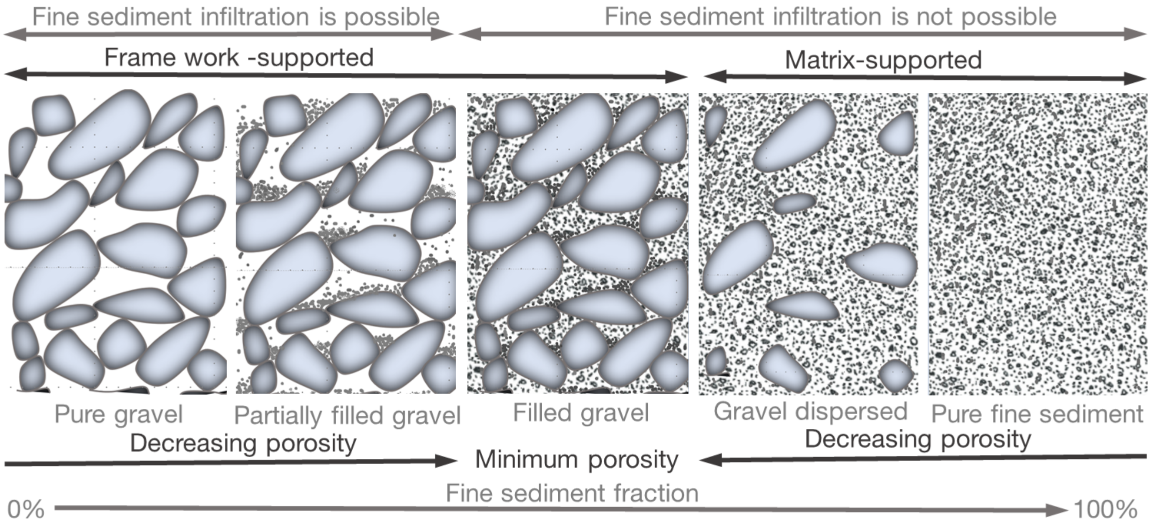

Figure 3.1 Schematic structure of bottom sediments as a function dependent on the magnitude of the fine component sediment revised from Nunez-Gonzalez, Martin-Vide, and Kleinhans (2016).

3.2 Fine sediment infiltration

3.2.1 Introduction

Fine sediment infiltration, where sand or silt fills a previously vacant gravel substrate, has important ecological and river engineering implications (Cui et al., 2008; Gibson et al., 2009a; Matthias, 1999; Wood and Armitage, 1997). Therefore, studies for predictive analysis has interested engineers in both field laboratories and theories. A number of experiments have been conducted in sediment flumes to study the infiltration process (Beschta and Jackson, 1979; Carling, 1984; Cunningham, Anderson, and Bouwer, 1987; Einstein, 1968; Gibson et al., 2009b; Iseya and Ikeda, 1987; Schälchli, 1995). Improved techniques for sampling, which are used in the study of Gibson et al. (2009a), enabled the fine deposition distributions to be measured as a function of depth in open framework gravels. Fines can infiltrate into gravel beds through bridging and unimpeded static percolation (Gibson et al., 2009a). In addition to laboratories and field tests, Sakthivadivel and Einstein (1970) established a model to characterize the infiltration process of fine sediment through a porous column due to intra-gravel flow, following the conservation of mass for fine sediment and through correlating the probability that fine sediment particles lodge in place as a result of intra-gravel flow velocity. Lauck (1991) built a model that describes the infiltration process assuming sediment infiltration occurs as a stochastic process of particles falling into a predefined space. Cui et al. (2008) developed models for simulating infiltration process with several assumptions, where a fine particle is classified when its pore size is smaller than that of a clean coarse particle.

The investigations of the dependent of size ratio (fine sediment to gravel), pore diameter and porosity on exchange fine sediment process are attracted by many studies. Einstein (1968) conducted the first spontaneous percolation experimental investigation, proving that fine silica flour traveled through (infiltrated) a framework of clean gravel to the deposits base without being clogged, resulting in voids being filled from the base upwards. Experimentations have focused on the influence of the grain size ratio (the ratio of the coarse sediment diameter which makes up the bed framework D, and the fine sediment that infiltrates, d) on this process (Beschta and Jackson, 1979; Hickin, 1995; Gibson et al., 2009a). These studies have observed that with differing size ratios the finer sediment may exhibit unimpeded static percolation, form a bridge layer, or do not infiltrate into the bed. Unimpeded percolation is the process where the sediment matrix voids are filled deposit base upward with rather constant fine content. If fine sediments become blocked in void throats and are only able to infiltrate to a limited depth, typically ranging between 2.5 and $5.0D_{90}$, then a bridge layer is formed (Díaz, Fernández-Nieto, and Ferreiro, 2008) (D_x represents the grain size that x percent is finer). Further infiltration is prevented by the bridge layer and fine sediment accumulates to the bed surface because of the excess sediment supply from upstream. Huston and Fox (2015) found that a the coarse bed porosity together with the roughness Reynolds number, a combination that indicates the pore water velocity distribution is that of the initially un-infiltrated bed, was a significant factor of the maximum bridging depth. These investigations have been useful in describing and quantifying several traits of the infiltration process. However, little is known on the vertical fine sediment distribution, the influence of factors on infiltration process, the connection between the bed characteristics (included fine fraction, porosity) and morphodynamics.

Recently, a model concept for bed variation with porosity changes, considering the exchange processes between bed material and transport sediment, was introduced by (Bui, Bui, and Rutschmann, 2019). This model considered the effect of infiltration of fine sediment process in a gravel-bed river by involving the change of porosity in multi-layer. The active source term was developed based on transfer function between surface and subsurface layers. The fractional exchange rate was calculated by modifying the transfer function for deposition process proposed by (Toro-Escobar, Parker, and Paola, 1996). This transfer function only considered the fraction of fine sediment in surface layer, bed load and parameters related to surface layer thickness. However, this model has limitations because it did not involve the characteristics of both surface and subsurface layers in terms of porosity change and critical entrance ratio. In a natural process of infiltration, the characteristics of the active layer include porosity, grain size distribution, and interaction force between fine sediment and gravel, which all significantly contribute to the infiltration process. Furthermore, other features consisting of compaction degree of gravel-bed, cohesion and contact forces also considerably influence the infiltration process in gravel-bed river with dense granular flow, which were neglected in these models.

3.2.2 The saturated fine sediment fraction

Bed sediments are usually divided into two different size classes: The fine sediment includes particles with a size less than 2 mm (i.e., sand) and coarse sediment with a particle size larger than 2 mm (i.e., gravel). The fine fraction of fine particle is typically defined in two ways. The first definition of the fine fraction β^* is defined as the volume of fine sediment as a fraction of bed volume (Cui et al., 2008):

$$\beta^* = \frac{V_f}{V_f + V_p + V_g} \tag{3.1}$$

This second definition, more popular in river science than the first definition is denoted with β which is defined as the volume or mass of fine sediment as a fraction of all sediment (Cui et al., 2008).

$$\beta = \frac{V_f}{V_f + V_g} \tag{3.2}$$

V_f is the volume of fine sediment, V_p is the volume of pore space, V_g the volume of gravel.

The second definition of the volumetric fraction is used in this study. A transformation between β and β^* is needed in order to compare results and model predictions from various studies. There is a simple transformation for the porosity of a clean gravel bed (p_g) (Cui et al., 2008).

$$\beta^* = \frac{\beta\,(1 - p_g)}{1 - \beta} \tag{3.3}$$

$$\beta = \frac{\beta^*}{(1 - p_g - \beta)} \tag{3.4}$$

If the effect of size ratio of coarse gravel to fine sediment (D/d) is neglected (for example the fine grain size is significantly smaller than that of gravel particles $D/d \rightarrow \infty$, where D denotes the characteristic particle size of gravel and d represents the characteristic particle size of fine sediment), all the void space in the gravel mixture may be filled with fine sediment particles and the void space within the fine sediment. The solid volume and pore volume in the gravel mixture are determined by $V_g = (1 - p_g)V_t, V_{pg} = p_g V_t$, respectively. V_t is the gravel mixture's total volume (for example the combined volume of pores and solids), and p_g is the gravel's porosity. When the pore space of the gravel mixture being entirely filled by fine sediment assuming that $D/d \rightarrow \infty$ the volume of fine sediment (solid only) will be $V_s = (1 - p_f)p_g V_t$, where p_f is the fine sediment's porosity, we attain the expression for saturated fine sediment infiltration (Leonardson, 2010; Wooster et al., 2008):

$$\beta^*_{sat} = \frac{V_s}{(V_g + V_s)} \tag{3.5}$$

$$\beta^*_{sat} = \frac{\left(1 - p_f\right) p_g V_t}{(1 - p_g) V_t + \left(1 - p_f\right) p_g V_t} = \frac{\left(1 - p_f\right) p_g}{1 - p_f p_g} \tag{3.6}$$

where β^*_{sat} is the saturated fine sediment infiltration value for the deposit under the assumption $D/d \rightarrow \infty$.

The fine sediment fraction which fills the pores of a gravel decreases with an increase in fine sediment particle size, because larger fine sediment particles are more difficult to fit into the gravel interstices. Thus, when considering the effect of the size ratio of fine sediment to gravel on infiltration process, a more generalized expression of Equation (3.6) is described by the following equation:

$$\beta^*_{sat} = \frac{\left(1 - p_f\right) p_g}{1 - p_f p_g} f_n\left(\frac{D}{d}\right) \tag{3.7}$$

where $f_n(D/d)$ is a function of D/d. Wooster et al. (2008) propose the experimental equation for estimating the effect of size ratio (D/d):

$$f_n\left(\frac{D}{d}\right) = 1 - exp\left[a_2\left(\frac{D}{d}\right) + b_2\right] \tag{3.8}$$

where b_2 and a_2 are coefficients determined with experimental data.

3.2.3 Theory model of fine sediment infiltration

Cui et al. (2008) developed a theoretical model for fine sediment infiltration by adopting a filtration relationship proposed by Sakthivadivel and Einstein (1970) for the settling of sand through a riverbed. The continuity equation for fine sediment exchange in gravel bed can be derived as following expression (Figure 3.2):

$$\frac{\partial \beta^*}{\partial t} + \frac{\partial q}{\partial z} = 0 \tag{3.9}$$

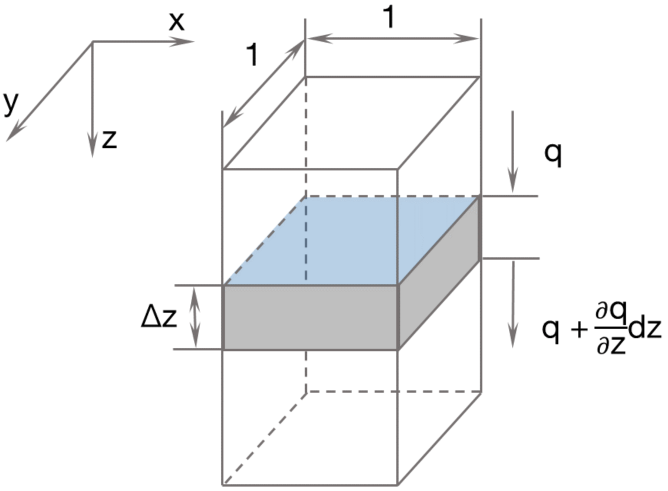

Figure 3.2 Schematic diagram showing the finite volume used for the derivation of governing equation for fine sediment infiltration revised from Cui et al. (2008).

where q is downward fine sediment flux per unit area (solid volume per unit time per unit area; t is time; and z is depth into the sediment deposit). Both β^* and q are functions of space and time, $q = q(z,t)$, and $\beta^* = \beta^*(z\ ,\ t)$.

A trapping coefficient, defined earlier as the fraction of the fine sediment load trapped in the bed when traveling vertically a unit, was introduced by Cui et al. (2008):

$$\Delta V_f = \xi q \Delta t \Delta z = \frac{\partial \beta^*}{\partial t} \Delta t \Delta z \tag{3.10}$$

Combining this relation with Equation (3.9):

$$\frac{\partial \beta^*}{\partial t} = \xi q \tag{3.11}$$

$$\frac{1}{q}\frac{\partial q}{\partial z} = -\xi \tag{3.12}$$

Using the hypothesis that the trapping coefficient (ξ) is either a constant or is at a minimum value when a sediment deposit is void of fine sediment and increases monotonically with increases in fine fraction (β^*), Cui et al. (2008) proposed the following model for ξ:

$$\xi = \xi_o \, exp\left(\phi \frac{\frac{\beta^*}{\beta^*_{sat}}}{1 - \frac{\beta^*}{\beta^*_{sat}}}\right) \tag{3.13}$$

Substituting Equation (3.13) into Equation (3.12) yields:

$$\frac{1}{q}\frac{\partial q}{\partial z} = -\xi_o \, exp\left(\phi \frac{\frac{\beta^*}{\beta^*_{sat}}}{1 - \frac{\beta^*}{\beta^*_{sat}}}\right) \tag{3.14}$$

Where ϕ is dimensionless coefficient with a nonnegative value that defines the shape of the ξ to β^*/β^*_{sat} relation (Cui et al., 2008).

Cui et al. (2008) proposed the following boundary conditions to be consistent with infiltration of a clean gravel-bed with constant influx q_o that stops at a time t_{clog} when the sand fraction reaches a maximum possible value β^*_o :

$$\beta^*(t = 0, z > 0) = 0 \, , \, q(t = 0, z > 0) = 0 \tag{3.15}$$

$$q(t > 0, z = 0) = \begin{cases} q_o & \beta^*(z = 0) < \beta^*_o \\ 0 & \beta^*(z = 0) = \beta^*_o \end{cases} \tag{3.16}$$

Cui et al. (2008) stated that the only analytical solution to Equation (3.14) is the case where ξ is constant, in which case $\beta(z)$ decreases exponentially with depth. If ξ is constant and using the above boundary conditions, then $\beta^*(z,\, t)$ is determined by Equation (3.11):

$$\beta^*(t,\, z) \;=\; \int_0^{\beta^*} d\beta^{*\prime} \;=\; \xi_o \int_0^t q_s(z,\, t'\,)\partial t' \tag{3.17}$$

where the apostrophe on $\beta_o^*\ (t_o)$ indicates the integration variable corresponding to $\beta^*(t)$. The total flux past any depth z before time t_{clog} is equal to the total flux into the bed minus the sand deposited between the depths of 0 and z (Leonardson, 2010). This is represented by rewriting the right side of Equation (3.17):

$$\xi_o \int_0^{t_{clog}} q_s(z,\, t'\,)\partial t' \;=\; \xi_o \int_0^{t_{clog}} q_s(z=0,\, t'\,)\partial t' - \xi_o \int_0^{t_{clog}} \beta^*(z',t_{clog}\,)\partial z'\;. \tag{3.18}$$

In Equation (3.18), the first term on the right side is denoted by β_o^*. Connecting the left side of Equation (3.17) with the right side of Equation (3.18) yields:

$$\beta^*\left(z,t_{clog}\right) \;=\; \beta_o^* - \xi_o \int_0^z \beta^*(z|',t_{clog})\partial z' \tag{3.19}$$

The derivative of Equation (3.17) with respect to z:

$$\beta^*(z,t_{clog}) = \beta_o^* e^{-\xi_o z} \tag{3.20}$$

and therefore:

$$\beta^*(z,\, t_{clog}) \;=\; \beta_o^* e^{\,-\xi_o z} \tag{3.21}$$

For fine sediment deposition case, it is assumed that infiltration has come to completion and so $\beta^*(z) = \beta^*(z,\, t_{clog})$. These parameters in the equation (3.20) are used to investigate the controlling factors that affect on the infiltration processes of fine sediment into gravel-bed Rivers.

3.2.4 The empirical model of fine sediment infiltration

The empirical model for infiltration of fine sediment into gravel bed, developed by Wooster et al. (2008), is based on the theoretical model by Cui et al. (2008) and assumes a constant trapping coefficient ξ_w.

$$\beta(z) = \beta_{o,w} e^{-\xi_w \left(\frac{z}{D_g} - 2\right)} \tag{3.22}$$

To develop an empirical relationship between $\beta_{o,w}$ and ξ_w, Wooster et al. (2008) used a set of plane-bed sand infiltration experiments into nine different gravel beds under uniform flow. The gravel mixtures in the beds included a range of D_{50}/d_{50} from 15 to 50 and D_{15}/d_{85} from 6 to 32. Regression analysis was used to develop empirical models of $\beta_{o,w}$ and ξ_w as functions of the gravel and sand geometric standard deviation:

$$\beta_{o,w} = \frac{(1-p_f)p_g}{1-p_f p_g}\left[1 - exp\left(-0.0146\,\frac{D}{d} + 0.0117\right)\right] \tag{3.23}$$

$$\xi_w = 0.0233\sigma_g^{1.95}\left[ln\left(\frac{D\sigma_g}{d}\right) - 2.44\right] \tag{3.24}$$

where p_f is the porosity of sand, p_g is the porosity of gravel and σ_g is the geometric standard deviation of the gravel grain size distribution.

3.2.5 The effect of flow on infiltration

There is uncertainty in the relationship between infiltration and flow conditions (Leonardson, 2010). In flume experiments, it has been proven that infiltration has been positively correlated to shear stress (Beschta and Jackson, 1979; Gibson et al., 2011). Frostick, Lucas, and Reid (1984) found that areas of high velocity also had high infiltration and in contrast, Carling and McCahon (1987) found that in areas of slack water high infiltration also existed. Sear (1993) found that suspended sediment infiltration was negatively correlated to shear stress but bed load infiltration was unrelated to shear stress. Gibson et al. (2009a) performed 11 identical sand infiltration experiments with and without water flowing while using the same sediment mixtures. A slightly smaller amount of sand infiltrated during the no-flow experiments than in the flow experiments when using the same sediment.

The Wooster's model did not focus on flow since discharge was kept constant for all experiments. Through the introduction of the flow and no-flow experiments, a small range of flow conditions was characterized in the infiltration data (Wooster et al., 2008). To incorporate flow into a model for vertical fine fraction distribution, this data was used. Because infiltration is a subsurface process, the analysis emphasized subsurface flow (Leonardson, 2010; Wooster et al., 2008). An explicit model for flow in the upper pore spaces was developed to achieve this by Leonardson (2010).

3.2.6 Summary of experimental conditions

The simulation results in this study are compared with the experimental results conducted by (Gibson et al., 2011; Gibson et al., 2009a; Wooster et al., 2008). In this section, a brief introduction of their experimental conditions is introduced.

In both experiments (Wooster et al., 2008; Gibson et al., 2009a), fine sediment was infiltrated into an immobile gravel-bed in a flume. The fine sediment was first added at the entrance and moved as bed load along the length of the flume until it had been carried over the sampling areas. At this moment, Gibson et al. (2009a) immediately cut off the flow. Water was kept flowing at the same rate in Wooster et al. (2008) until all surface fines had been washed away. The flume beds were sampled in several locations afterwards. In the large dataset gathered by Wooster et al. (2008) one unimodal sand mixture infiltrated into nine different gravel mixtures at three different feed rates. The bed was sampled by excavating 12 cm diameter circular pits, each comprising of 1-4 horizontal layers. The sand seals produced in the low and medium feed rate experiments were alike, while considerably less sand had infiltrated in the high feed rate experiments. The model presented in Wooster et al. (2008) established from only low- and medium-feed data. In Wooster et al. (2008), the nine different sediment mixtures are referred to as Zones 1-9; Zone 10 is a duplicate of Zone 1. Table 3.1 summarizes the experimental conditions. The experiments of Gibson et al. (2009a) included infiltration of two different sizes of sand into one gravel mixture (Table 3.1).

Gibson et al. (2009a) additionally performed another set of experiments with the same sediments but without flowing water. In the no-flow experiments, sand was fed by dropping it into the water from above rather than through a flume. Samples were collected using 10 cm diameter canisters filled with gravel and, prior to infiltration, were buried in the bed. Samples were removed in 8-10 horizontal layers that encompassed the sediment-water interface down to the bottom of the canister. The sediment used by Gibson et al. (2009a) abides to the range of sediment used to create the Wooster model in terms of D_{50}/d_{50}, D_{15}/d_{85}, gravel size, and that the sands were close in diameter. Experiments ran until the substrate had either bridged or filled at an observation window located 14 m downstream of the sand source. This corresponded to run times of 61.9 to 111.5 min. The flume was gradually drained after each experiment and cores were removed from the center of the flume at 4.3, 8.3, 11.3, and 15.3

m downstream of the source. Four flume experiment with tracer materials were performed in Gibson et al. (2011) to examine how a pulse of fine sediment infiltrates into a gravel bed. The experimental conditions of three experiments for immobile gravel-bed are described in Table 3.1. One additional, flexible sample location was additionally selected for each experiment. In Gibson et al. (2011) experiment, the cores were extracted in roughly 1 cm layers that were then dried and individually sieved. Most core samples included two distinct types of layers. The top one or two layers (bed load layers) were found to have little or no gravel and rather contained sand that was actively being transported over the clogged gravel before the experiment finished. Below the bed load layers, six to nine layers of gravel substrate with interstitial sand deposits were contained in the core. The material retained at each sieve from each layer was captured and labeled separately so to determine each layer's size specific introduction-time distribution of interstitial fine sediment Gibson et al. (2011).

Table 3.1 Experimental data collected by Nunez-Gonzalez, Martin-Vide, and Kleinhans (2016).

ID	Run	Bed gravel		Feed sediment		ASF [1]
		D_m [mm]	$\sigma^{(D)}$	d_m [mm]	$\sigma^{(d)}$	f_s
	Wooster et al. (2008)					
1	1(Z1)	7.2	1.87	0.35	1.24	6%
2	1(Z2)	10.2	1.77			11%
3	1(Z3)	13.1	1.68			12%
4	1(Z4)	17.2	1.17			17%
5	1(Z5)	7.4	1.9			5%
6	1(Z6)	7.9	1.22			12%
7	1(Z7)	8.7	1.71			7%
8	1(Z8)	7.6	1.46			5%
9	1(Z9)	4.3	1.65			5%
10	1(Z10)	7.2	1.87			6%
	Gibson et al. (2009a)					
11	1(S-IFS1)	7.1	1.37	0.43	1.70	25%
12	2(S-IFS2)			0.26	1.94	20%
13	3(S-IFS3)			0.21	1.55	20%
14	4(S-IFS4)			0.12	1.37	-

---

[1] Average saturated fines content.

	Gibson et al. (2011)					
15	1(Z1)	7.7	1.41	0.65	1.58	20%
16	2(S2)	7.7	1.41	0.36	1.66	19%
17	3(S2)	9.7	1.27	0.36	1.66	31%

3.3 Porosity variation

3.3.1 Introduction

The significantly different sizes of fine sediment and coarse bed material is the reason for the change in the void space of gravel-bed rivers. If finer sediments occupy the interstitial spaces of coarser bed materials, the void space of the bed material decreases. If finer sediments are supplied at a small rate to a riverbed covered by a completely developed armor coat, the fine sediments can infiltrate into the interstitial spaces of the coarser bed material and move into void spaces. As a result of fine sediment exchange in void space, the ratio of void space over the total of gravel-bed and the porosity change (Frings, Kleinhans, and Vollmer, 2008; Nunez-Gonzalez, Martin-Vide, and Kleinhans, 2016). The study of variation in porosity is vital for fluvial geomorphology assessment as well as in river ecosystem management. As mentioned above, in the field of the river management modelling, the large amount of fine sediment stored in the void space of gravel-bed may not be taken into account when porosity is considered constant (Frings, Kleinhans, and Vollmer, 2008). The void spaces of gravel-bed, home of small fishes and aquatic species, are essential and are of strong importance in assessing changes in the pore structure of gravel-bed river (Gayraud and Philippe, 2003). Navaratnam, Aberle, and Daxnerová (2018) confirmed the effect of porosity and grain orientation on flow resistance from studies carried out over artificial beds that a porous gravel-bed imposes higher flow resistance than its non-porous counterpart for comparable relative submergences. Morphologically, the porosity strongly influences the volume of bed material and bed level changes (Verstraeten and Poesen, 2001; Wilcock, 1998). Thus, for gravel-bed rivers, the change of the bed porosity should be taken into account in hydromorphological models (Bui, 2018; Frings, Kleinhans, and Vollmer, 2008; Sulaiman, Tsutsumi, and Fujita, 2007a).

Porosity prediction for fluvial gravel-bed mixtures can be classified into two types: empirical prediction and theoretical prediction. The empirical prediction focuses primarily on the relationship between grain size and porosity. Examples are the prediction of Peronius and Sweeting (1985), Wooster et al. (2008), and Wu and Wang (2006). Carling and Templeton (1982) studied the sedimentological properties of British upland streams, focusing on consolidated, clast-supported gravel deposits with variable infills of sand and silt. They observed a strong relation between porosity and median grain size. Wu and Wang (2006) reanalyzed existing laboratory and field data in order to improve the earlier porosity prediction of Komura (1963). Wooster et al. (2008) mixed grains ranging from 0.075 to 22 mm in size in order to construct unimodal sand-gravel mixtures. After slightly compacting the samples by hand, they measured the porosity of the mixtures, which was found to be related to the standard deviation of the grain size distribution. A very different type of empirical porosity predictor was developed by Peronius and Sweeting (1985). They included the effect of grain shape on porosity and used a Kolmogorov-Smirnov statistic to express grain size. Their predictor was based on porosity measurements in densified, artificially packed, cohesionless mixtures. Empirical predictions are primarily based on porosity measurements in natural sediments and are easy to apply because of their simple form but cannot be employed with confidence in areas other than the original study area. Because of the limitation in the number of controlling factors considered (only deviation of the grain size distribution, median grain size) the porosity calculation based on the relation between the sediment standard deviation strongly overestimates the porosity of nearly uniform sediments. The porosity calculation based on the deviation of the grain size distribution that leads to an increase in porosity seems valid, however, this does not result in an accurate porosity prediction (Frings, Schuttrumpf, and Vollmer, 2011).

In addition to empirical porosity predictors, there are also some theoretical packing models that can be used to predict porosity. Most of them originate from laboratory experiments with spherical grains and simple packings (often consisting of only two size fractions). Early theoretical packing models simulated either the mixing process filling or the mixing process occupation (Ouchiyama and Tanaka, 1984). In natural sediment mixtures with a large range of grain sizes, however, filling effects and occupation effects occur simultaneously. Yu and Standish (1991) and Yu and Standish (1993), known as one of the best performances for porosity prediction of sand gravel-bed (Frings, Schuttrumpf, and Vollmer, 2011), developed a porosity prediction for continuous grain size distributions that accounts for both mixing processes at the same time. This semi-model has a required experimental coefficient and was recently verified for a binary mixture. A computer random-packing model of spherical particles, mainly studied in the research field of powder technology, is a very useful tool to obtain porosity. Suzuki and Oshima (1983) employed a random-packing model to find the positions of particles in a vessel by dropping and rolling. Nolan and Kavanagh (1993) improved a random-packing model for a lognormal distribution. Desmond and Weeks (2014) developed a different random packing model to obtain the packing fraction. These processes' significant time consumption leads to a difficulty of their application in a large domain or their integration into other calculation systems which require the porosity recalculation at every time step that the size fraction change.

3.3.2 Fundamentals

Porosity is a granular material property of high importance in describing porous media. It is a grain samples ratio of pore volume (V_p) to bulk volume (V_b).

$$p = \frac{V_p}{V_b} \tag{3.25}$$

Although it is a dimensionless quantity, written as either decimal or percentage, it represents a volume ratio of pore space to the bulk space. A simple example of porosity for a granular media is illustrated in Figure (3.3).

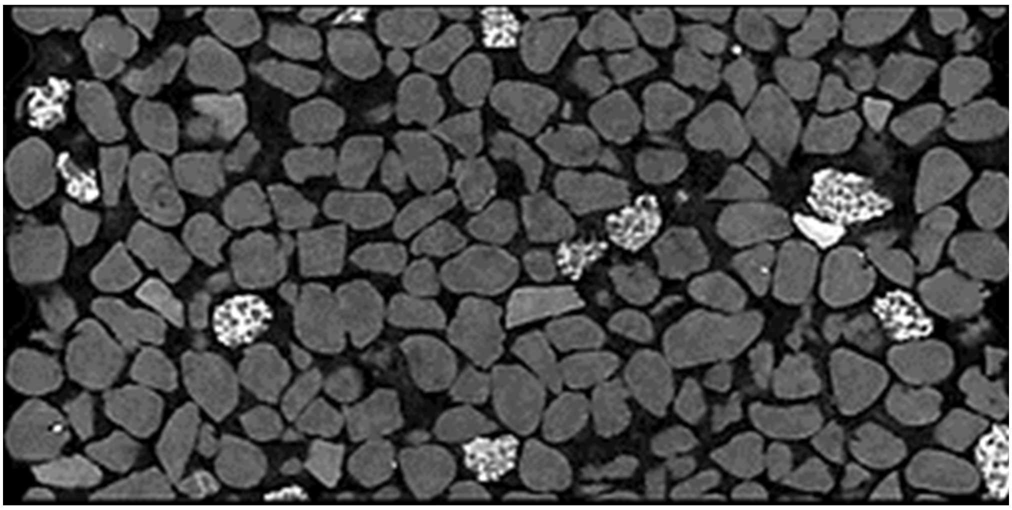

Figure 3.3 Gravel for structural analysis using X-Ray (black areas are pore space, gray areas are grains) (OR3D, 2019).

.

Quantifying the storage capacity of the gravel bed river, and subsequently defining the volume of fine sediment available to be produced, are primary uses of learning porosity. In some experimental methods, porosity is related to the penetration rate and the volume of fluid (water) in the void space.

Porosity is an average property defined over the representative elementary volume (REV) (Bear, 2013). Therefore, the volume of the porous media must be larger than the single pore size so that the addition of more pores will maintain a statistical average that is meaningful but must be smaller than the heterogeneity of the entire flow domain. Thus, the REV offers a uniform porosity value for the entire domain of the porous media.

Soil void ratio (e): Porosity is usually used in parallel with soil void ratio (e) , which is defined as the ratio of the volume of voids to the volume of solid. The porosity and the void ratio are inter-related as follows:

$$e = p/(1-p) \quad \textit{and} \quad p = e/(1+e) \tag{3.26}$$

Effective porosity: Numerous porosity types have been developed based on the degree of connectivity or the time of pore development. Total porosity is defined as the ratio of the media's total pore space to the total bulk volume. The ratio of interconnected pore space to the bulk volume of the rock is known as effective porosity. Figure 3.4 shows the example of total and effective porosity in a vuggy rock. It is important to note the pathway for fluid to migrate in connected pores and the isolated nature of others. Fine sediment infiltration depends on the fluid flowing through the porous media. Subsequently, effective porosity is of important to reservoir engineering (Asquith, 1985).

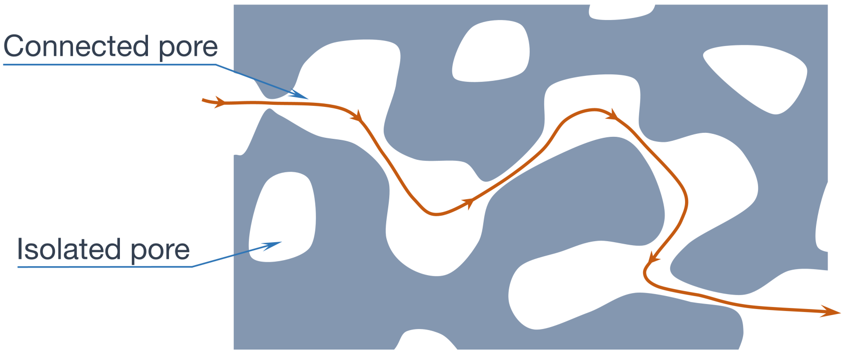

Figure 3.4 Isolated and connected pores in a vuggy rock (Asquith, 1985).

Controls on Porosity: The initial (pre-diagenesis) porosity is influenced by three main microstructural parameters. These are grain size and its distribution, grain packing, and particle shape. However, it is seldom found that the initial porosity is in real gravel, as these have subsequently been impacted by the secondary controls on porosity such as geochemical diagenetic and compaction processes. Theoretical porosities for differing grain packing arrangements can be calculated. The theoretical maximum porosity for a cubic packing of gravel constructed of spherical grains of uniform size is 0.4764 and is independent of grain size (Glover, 2000). Figure 3.5 displays the maximum porosity of other packing arrangements.

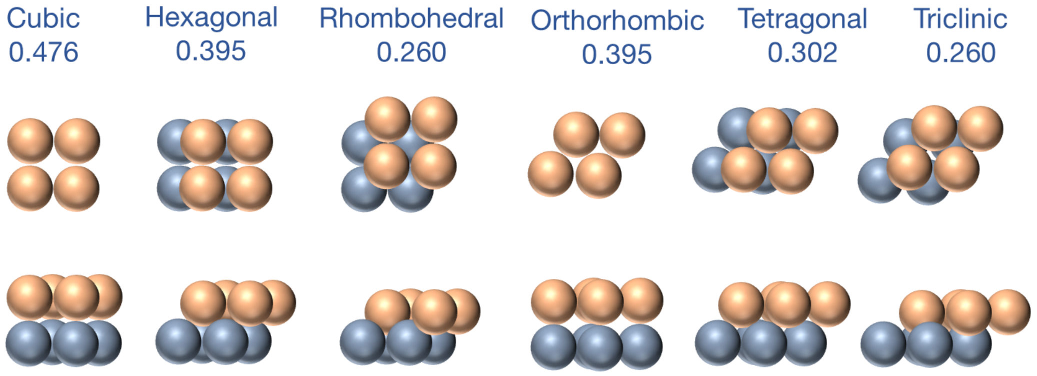

Figure 3.5 Maximum porosity for different packing arrangements revised from Glover (2000).

3.3.3 The range of porosity values

In the bed of a lake or in gravel-bed river, the porosity value is very high (up to 60%) in unconsolidated sediments that have been recently deposited (Asquith, 1985; Frings, Schuttrumpf, and Vollmer, 2011). However, more ordinary materials, including loose sands and gravel may have porosities up to 45% which are either extremely unstable or stabilized by cement. It is possible for high porosities to exist when porosity is due to dissolution (secondary porosity). In regards rock materials, total porosity may also be very high, however, due to unconnected pores and vugs that make up the pore structure. Their permeability can be very low (Asquith, 1985). Likewise, porosities can be very low. Table 3.2 presents the porosity (p) ranges for a few common bed materials.

Table 3.2 Typical porosity (p) values of fine sediment and gravel for different river-bed materials (Geotechdata.info, 2013).

Description	USCS[2]	p_{min}	p_{max}	$p_{specific}$
Well graded gravel, sandy gravel, with little or no fines [1]	GW	0.21	0.32	
Poorly graded gravel, sandy gravel, with little or no fines [1]	GP	0.21	0.32	
Silty gravels, silty sandy gravels [1]	GM	0.15	0.22	
Gravel [2]	(GW-GP)	0.23	0.38	
Clayey gravels, clayey sandy gravels [1]	GC	0.17	0.27	
Glatial till, very mixed grained [4,5]	(GC)	-	-	0.2
Well graded sands, gravelly sands, with little or no fines [1,2]	SW	0.22	0.42	
Coarse sand [2]	(SW)	0.26	0.43	
Fine sand [2]	(SW)	0.29	0.46	
Poorly graded sands, gravelly sands, with little or no fines [1,2]	SP	0.23	0.43	
Silty sands [1,2]	SM	0.25	0.49	
Clayey sands [1]	SC	0.15	0.37	
Inorganic silts, silty or clayey fine sands, with slight plasticity [1]	ML	0.21	0.56	
Uniform inorganic silt [3]	(ML)	0.29	0.52	
Inorganic clays, silty clays, sandy clays of low plasticity [1]	CL	0.29	0.41	
Organic silts and organic silty clays of low plasticity [1,3]	OL	0.42	0.68	
Silty or sandy clay [3]	(CL-OL)	0.2	0.64	
Inorganic silts of high plasticity [1]	MH	0.53	0.68	
Inorganic clays of high plasticity [1]	CH	0.39	0.59	
Soft glacial clay [4,5]	-	-	-	0.55
Stiff glacial clay [4,5]	-	-	-	0.38
Organic clays of high plasticity [1,3]	OH	0.5	0.75	
Soft slightly organic clay [4,5]	(OH-OL)	-	-	0.66

---

[2] The Unified Soil Classification System

Peat and other highly organic soils [4,5]	Pt	-	-	
Soft very organic clay [4,5]	(Pt)	-	-	0.75

[1]Swiss Standard SN 670 010b, Characteristic Coefficients of soils, Association of Swiss Road and Traffic Engineers.

[2]Das, B., Advanced Soil Mechanics. Taylor & Francis, London & New York, 2008.

[3]Hough, B., Basic soil engineering. Ronald Press Company, New York, 1969.

[4]Terzaghi, K., Peck, R., and Mesri, G., Soil Mechanics in Engineering Practice. Wiley, New York, 1996.

[5]Obrzud R. & Truty, A.THE HARDENING SOIL MODEL - A PRACTICAL GUIDEBOOK Z Soil.PC 100701 report, revised 31.01.2012.

3.3.4 Empirical porosity calculation

The empirical porosity predictors of river-bed material focus mainly on the relation between porosity and one represented parameter (median grain size or standard deviation) of bed material and neglecting the effect of other factors effected on the porosity (Frings, Schuttrumpf, and Vollmer, 2011). Most of the empirical porosity models were developed by analyzing the collected data from natural sediment and laboratory.

Carling and Reader (1982) analyzed the sediment properties of British upland streams, concentrating on consolidated, clast-supported gravel deposits ($D = 2 - 1000mm$) with variable infills of sand and silt. They observed a strong relation between porosity (p) and median grain size (D_{50}, m) for D_{50} in range $(0.005, 0.200m)$:

$$p = 0.0333 + \frac{0.4665}{1000{D_{50}}^{0.21}} \tag{3.27}$$

Wu and Wang (2006) studied existing laboratory data in order to enhance the earlier porosity predictor of (Komura, 1963). They also found a clear relation between porosity and median grain size for $1.00\ 10^{-6} < D_{50} < 0.100$.

$$p = 0.13 + \frac{0.21}{(1000D_{50} + 0.002)^{0.21}} \tag{3.28}$$

Wooster et al. (2008) combined grains ranging from 0.075 to 22 mm in size in order to build unimodal sand-gravel mixtures. After slightly compressing the samples, they measured the porosity of the mixtures, which was found to be related to the standard deviation of the grain size distribution. The result of the porosity predictor can be described by the following equation:

$$p = 0.621 e^{-0.457\sigma_\varphi} \tag{3.29}$$

for $0.26 < \sigma_\varphi < 1.80$ with σ_φ the geometric standard deviation of the grain size distribution, expressed on the φ scale (Krumbein, 1934):

$$\sigma_\varphi = \sqrt{\sum f_j \left(\varphi_j - \sum f_j \varphi_j\right)^2} \tag{3.30}$$

where f_j is the fraction content of sediment in size class j and φ_j is the characteristic sediment diameter for size class j^{th} expressed on the φ scale, equal to $log_2(D_j/D_{ref})$, and D_j is the characteristic sediment diameter expressed in m and D_{ref} is a reference size of $0.001m$.

3.3.5 Theorical porosity calculation

3.3.5.1 Porosity of binary mixtures

The volume of a unit bed sediment with a porosity p consists of two types of sediment: coarse and fine. The absolute volume (without porosity) of the bed sediment is $(1-p)$. The size of fine particles compared to coarse sediment is usually less than 0.154 (critical ratio for rhomebohedral regular packing), and the arrangement of coarse particles is not affected by the fine particles during the infiltration process.

If the bed does not contain fine sediment, then the total volume of coarse sediment is $(1-p^{(D)})V_b$, where $p^{(D)}$ is the porosity of coarse sediment, $(V_b = 1)$ is bulk volume of a unit bed sediment. Correspondingly, the relative ratio of coarse sediment volume to the total volume of bed sediment is determined.

$$f^{(D)} = \frac{1-p^{(D)}}{1-p} \tag{3.31}$$

If the bed does have fine sediment then $f(d) = (1-f^{(D)})$ and the correlation between porosity of bed and porosity of coarse sediment and the relative proportions of fine sediment is as follows:

$$p = \frac{p^{(D)} - f^{(d)}}{1-f^{(d)}} \tag{3.32}$$

The minimum of bed porosity is ($p^{(D)} \times p^{(d)}$). Substituting this value into Equation (3.32) we obtain the relationship between bottom porosity and the characteristics of fine sediment for this case as follows:

$$p = \frac{p^{(d)} f^{(d)}}{1 - p^{(d)}\left(1 - f^{(d)}\right)} \tag{3.33}$$

Following Nunez-Gonzalez, Martin-Vide, and Kleinhans (2016), Equation (3.33) is used to calculate the porosity for the bed in the predominance of the sand matrix (right panel of Figure 3.1). As mentioned above, equations (3.32) and (3.33) are obtained with ideal gravel; these equations will be modified by measured data. For example, Koltermann and Gorelick (1995) proposed the followings expression for calculating the bed porosity:

$$p = \begin{cases} p^{(D)} - \left(1 - p^{(d)}\right) f^{(d)} & if\ f^{(d)} \leq p^{(D)} \\ p^{(d)} f^{(d)} & if\ f^{(d)} \geq p^{(D)} \end{cases} \tag{3.34}$$

The bed porosity reaches the minimum value of p when the fine size fraction of sediment is approximately equal to the porosity of the coarse sediment. Kamann et al. (2007) has improved Equation (3.34) and proposed the same expression to calculate the porosity of the bottom as follows:

$$p = \begin{cases} p^{(D)} - \left(\frac{p^{(D)} - p_{min}}{f_{min}^{(d)}}\right) f^{(d)} & if\ f^{(d)} \leq p^{(D)} \\ p^{(d)} + \left(\frac{p^{(d)} - p_{min}}{1 - f_{min}^{(d)}}\right)\left(f^{(d)} - 1\right) & if\ f^{(d)} \geq p^{(D)} \end{cases} \tag{3.35}$$

Where $f_{min}^{(d)}$ is a fine size fraction when the bed porosity reaches the minimum value.

3.3.5.2 Porosity of mixture

The semi-analytical model for different grain sizes developed by Yu and Standish (1991) and Yu and Standish (1993) is one of the best models for predicting porosity of sand gravel (Frings, Schuttrumpf, and Vollmer, 2011).

The porosity model is based on the assumptions that the grains are spherical in shape, not deformable, uniform in density, and random packing. Although these assumptions are not fully similar to natural sediments, the porosity calculations are acceptable for natural sediments with angular grains (Yu and Standish, 1993). The porosity predictions have been extensively validated for three-fraction mixtures and can apply to multi fraction mixtures as well (Yu and Standish, 1991).

The mixture of n components with diameter $d_1 > d_2 > ... > d_n$ and specific volume $V_1, V_2, \ldots V_n$ is considered. The overall specific volume of mixture can generally be written as:

$$V = f\left(V_j, \beta_j, d_j\right) \tag{3.36}$$

Where V_j is the initial specific volume of component j^{th}, which corresponds to p_j is porosity of component j^{th}. For each component j of the mixture, M_j and N_j are calculated based on comparing the size ratio of the diameter of component j and another diameter with the critical ratio (0.154). The overall specific volume of the mixture is divided into three partial specific volumes $V^S_{j,ummxg}$, $V^{MI}_{j,mix}$ and $V^L_{j,unmxg}$ (Figure 3.6).

$$M_j = f(d_j) = \begin{cases} K & if\ d_k \geq d_j/0.154 > d_{k+1} \quad (k = 1...n) \\ 1 & \qquad\qquad if\ d_j/0.154 > d_1 \end{cases} \tag{3.37}$$

$$N_j = f(d_j) = \begin{cases} K & if\ d_{k-1} \geq 0.154 d_j > d_k \quad (k = 1...n) \\ n & \qquad\qquad if\ d_j/0.154 < d_1 \end{cases} \tag{3.38}$$

$$V^T_j = \left(V^S_{j,ummxg} + V^{MI}_{j,mix} + V^L_{j,ummxg}\right) \tag{3.39}$$

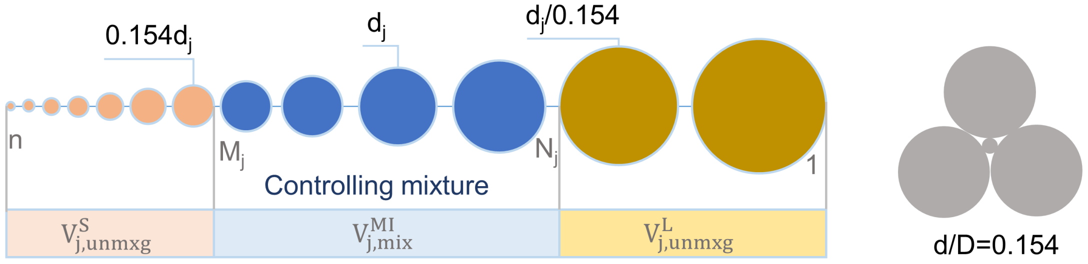

Figure 3.6 Classifying the mixture to partial specific volumes for diameter d_j.

A mixture of grains will be divided into partial specific volumes for each (d_j) grain based on the size ratio (Figure 3.6). The middle zone is the controlling mixture of grain size j^{th}

(occupation), the first zone and the last zone represent the filling mechanism. Particles in the first zone can fill, but not disturb the structure of particle j^{th} (d_j). Particle j^{th} can fill, but not disturb the structure of particles in last zone (Figure 3.6).

$V^{MI}_{j,mix}$ represents the unmixing effect which change the skeleton of the controlling component. Because the partial specific of controlling mixture is the same as the specific volume when only these controlling components themselves form a packing mixture:

$$V^{MI}_{j,mix} = V_{j,mix} \sum_{j=M}^{N} \beta_j \tag{3.40}$$

$$V_{j,mix} = V_{j,o} + \frac{\sum_{h=M}^{N-1} \sum_{l=h+1}^{N} \delta_{hl} \left(\left(\frac{d_l}{d_h} \right), \rho_o \right) \beta_h \beta_l}{\left(\sum_{j=M}^{N} \beta_j \right)^2} + \frac{\sum_{h=M}^{N-1} \sum_{l=h+1}^{N} \gamma_{hl} \left(\left(\frac{d_l}{d_h} \right), \rho_o \right) \beta_h \beta_l \left(\beta_h - \beta_l \right)}{\left(\sum_{j=M}^{N} \beta_j \right)^3} \tag{3.41}$$

Where δ_{hl}, γ_{hl} the quadratic coefficient and cubic coefficient express the joint action of mixture as can be seen in the (Figure 3.7). $V^{S}_{j,ummxg}$ and $V^{L}_{j,unmxg}$ are presented filling mechanism (Mixing effect). The semi-empirical interaction equations $f_{(j,k)}$ and $g_{(j,k)}$ are functions of diameter and density of controlling mixture, which was modified by Yu and Standish (1993). The equations are slightly different from that of previous equations. This is particularly true for spherical particles where initial porosity is relatively low:

$$V^{L}_{j,unmxg} = \begin{cases} 0 \quad if\, M = 1 \\ \sum_{j=1}^{M-1} \left[V_{j,mix} - \left(V_{j,mix} - 1 \right) \right] g\left(i,j\right) \beta_j \;\; if \;\; M \geq 2 \end{cases} \tag{3.42}$$

$$V^{S}_{j,unmxg} = \begin{cases} 0 \quad if \;\; N = n \\ \sum_{j=N+1}^{n} V_{j,mix} \left[1 - f\left(i,j\right) \right] \beta_j \;\; if \;\; N \geq n-1 \end{cases} \tag{3.43}$$

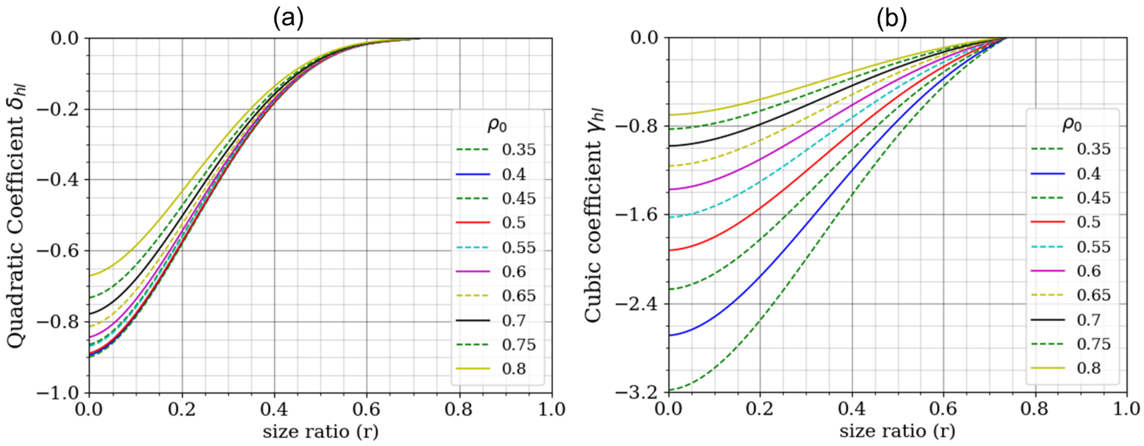

Figure 3.7 Joint action coefficient (a: for quadratic coefficient, b: for cubic coefficient).

Finally, the overall specific volume of mixture (V) is obtained by optimization and porosity of mixture (p) gained by following equation:

$$V = max(V_1^T, V_2^T, V_3^T ... V_j^T ... V_n^T) \tag{3.44}$$

$$p = 1 - \frac{V}{V_b} \tag{3.45}$$

Where V_b is bulk volume.

Chapter 4

Combination of DEM and ANN for predicting porosity and fine sediment distribution

4.1 Overview

In this chapter, a framework combining the Discrete Element Method (DEM) and Artificial Neural Network (ANN) was developed to predict the porosity and grain size distribution of gravel-bed rivers. Firstly, DEM was applied to simulate the 3D bed structure formed by fine sediment infiltrating into the gravel bed. Then, the results of porosity and sediment distributions obtained by the DEM were compared with experimental results to confirm the capacity of the DEM model. An algorithm was developed for calculating porosity and grain size distribution by the depth and along the flume. Finally, datasets obtained by the DEM model were used to design an ANN model, called Feed Forward Neural Network (FNN), for predicting the bed porosity grain size distribution.

The framework of DEM and ANN combining multiple techniques into one platform is illustrated in (Figure 4.1-I, II, III). Details of the implementation for each component are presented in subsequent subsections. The bed porosity variation model (Figure 4.1-IV) is introduced in the Chapter 5.

Parts of this chapter were published as:

Bui, V.H.; Bui, M.D.; Rutschmann, P. A Combination of Discrete Element Method and Artificial Neural Network for Predicting Porosity of Gravel-Bed River. Water 2019, 11, 1461, doi:10.3390/w11071461.

Bui, V.H.; Bui, M.D.; Rutschmann, P. Modeling infiltration process of fine sediment in gravel bed river. Proc. of Wasserbau-Symposium. 2018, 419-426, Austria.

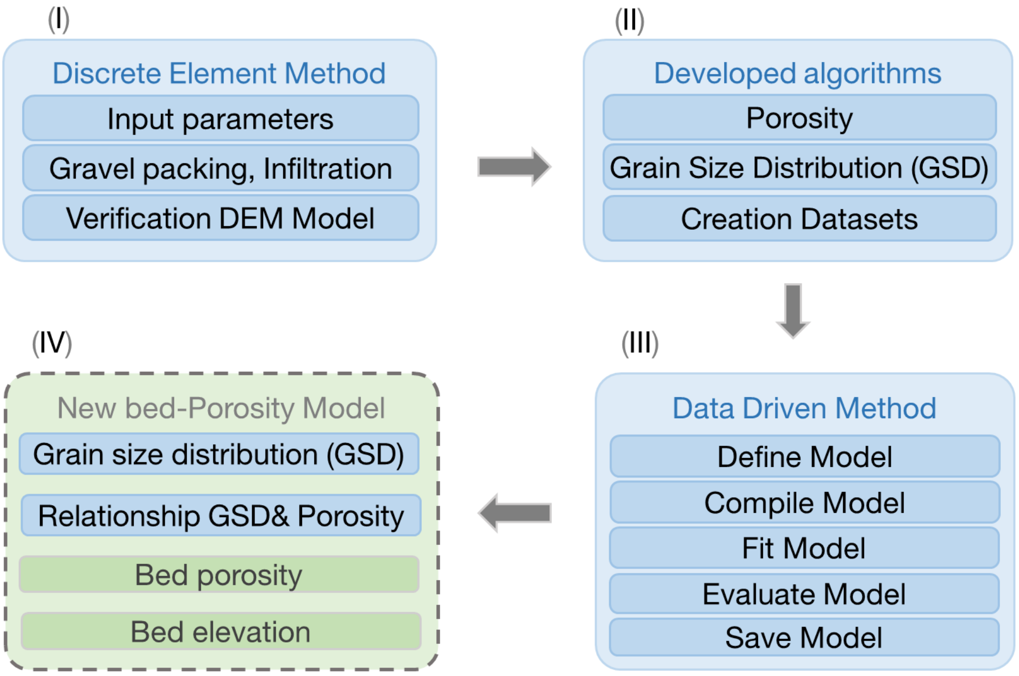

Figure 4.1 The prediction of porosity and fine sediment distribution using DEM and ANN.

4.2 Discrete Element Method

Discrete Element Method (DEM) was initially suggested by Cundall and Strack (1979) to model the mechanical behavior of granular flows and to simulate the forces acting on each particle and its motion. Typically, a particle can be classified into two types of motion in DEM: translation and rotation. Momentum and energy of particles are exchanged during collisions with their neighbors or a boundary wall (contact forces), and particle-fluid interactions, as well as gravity. Through the application of Newton's second law of motion, the trajectory of each *i* particle (including its acceleration, velocity, and position) are determined from the following equations:

$$m_i \frac{d\vec{u}_i}{dt} = m_i \vec{g} + \sum_k \vec{f}_{i,k} + \vec{f}_{i,f} \tag{4.1}$$

$$I_i \frac{d\vec{\omega}_i}{dt} = \frac{d_i}{2} \sum_k \left(\vec{f}_{i,k} \times \vec{n}_{i,k} \right) \tag{4.2}$$

Where m_i is the mass of a particle i; $\vec{u}_i$ is the velocity of a particle; $\vec{g}$ is Gravity acceleration; $\vec{f}_{i,k}$ is interaction force between particle i and particle k (contact force); $\vec{f}_{i,f}$ is interaction force between the particle i and the fluid ; I_i is moment of inertia; $\vec{\omega}_i$ is angular velocity; d_i is diameter of the grain i; $\vec{n}_{i,k}$ (directional contact) is vector connecting the center of grains i and k.

This study uses a contact force model based on the principle of spring-dashpot as well as suggestions of Johnson (1974). The contact force is obtained from a force analysis method; the stiffness and damping factors are analyzed in two directions: orthogonal and tangent to the contact surface between the two grains (Figure 4.2):

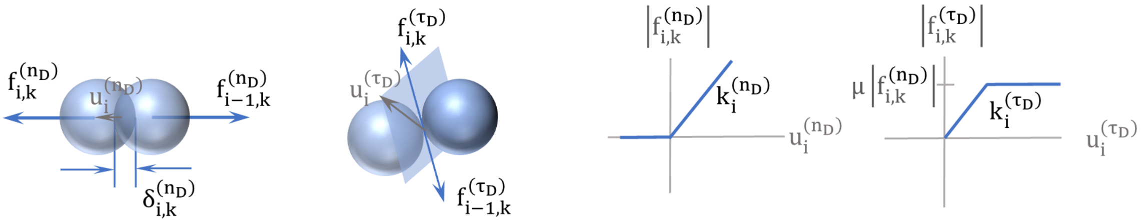

Figure 4.2 Contact forces revised from Fleischmann et al. (2015).

$$f_{i,k}^{(n_D)} = k_i^{(n_D)} \delta_{i,k}^{(n_D)} + \alpha_i^{(n_D)} \Delta u_i^{(n_D)} \tag{4.3}$$

$$f_{i,k}^{(\tau_D)} = k_i^{(\tau_D)} \delta_{i,k}^{(\tau_D)} + \alpha_i^{(\tau_D)} \Delta u_i^{(\tau_D)} \tag{4.4}$$

(n_D) and (τ_D) are known as two components of contact force in normal and tangential directions; k_i is stiffness of grain i; $\delta_{i,k}$ is the characteristic of the contact and displacement (also called the length of the springs in the two directions above); α_i is damping coefficient; and Δu_i is relative velocity of grain at the moment of collision. Following Coulomb, the value of tangential friction is determined by the product of the friction coefficient μ and the orthogonal force component. In the nonlinear contact force, Hertz – Mindlin model, the tangential force component will increase until the ratio $(f^{(\tau_D)}/f^{(n_D)})$ reaches a value of μ, and it retains the maximum value until the particles are no longer in contact with each other. A detail of the force models, as well as the method for determining the relevant coefficients, can be found in Bui, Bui, and Rutschmann (2018) and Johnson (1974).

After calculating all forces acting on the sediment particles as well as the velocity and the position of the particle at a previous time step, the current velocity and position of grain is found by solving Equations (4.3) and (4.4). The grain size distribution, as well as the bed porosity for whole the domain, can be defined afterwards. As a result, it is also possible to estimate the exchange rate of the fine fraction between different bed layers.

The DEM simulations begin with defining of the system geometry. This comprises of boundary conditions, particle coordinates and material properties by identifying the contact model parameters such as the friction and stiffness coefficients. How loading or deforming occurs within the system can be determined by the user through adding loads, deformations or settlements. The simulation begins as either a transient or dynamic analysis and runs until the completion of a defined number of time steps. An overlap check procedure starts after particles are inserted into the simulation box, which is conducted based on the geometry and coordinates of the particles. Upon the simulation of motions starting, particles that physically encounter each other are detected, and the contact forces are then calculated at each time step. The magnitude of particle forces is related to the distance between each of the contacting particles. From this data the resultant force including, body forces, external forces and moment acting on each particle can be calculated.

Moreover, two sets of equations for the dynamic equilibrium of the particles are computed in the case when particle rotation is blocked. Each particle translational movement is derived from the resultant applied force and each particle rotational movement is formulated from the resultant applied moment. By knowing the inertia of the particles, particle translational and rotational accelerations can be calculated. After new contact forces are determined, the particle positions and orientations are updated and ready for the next time step and will be repeated for all time steps. Although this system seems to respond in an almost static manner, the Discrete Element Method is a transient or dynamic analysis.

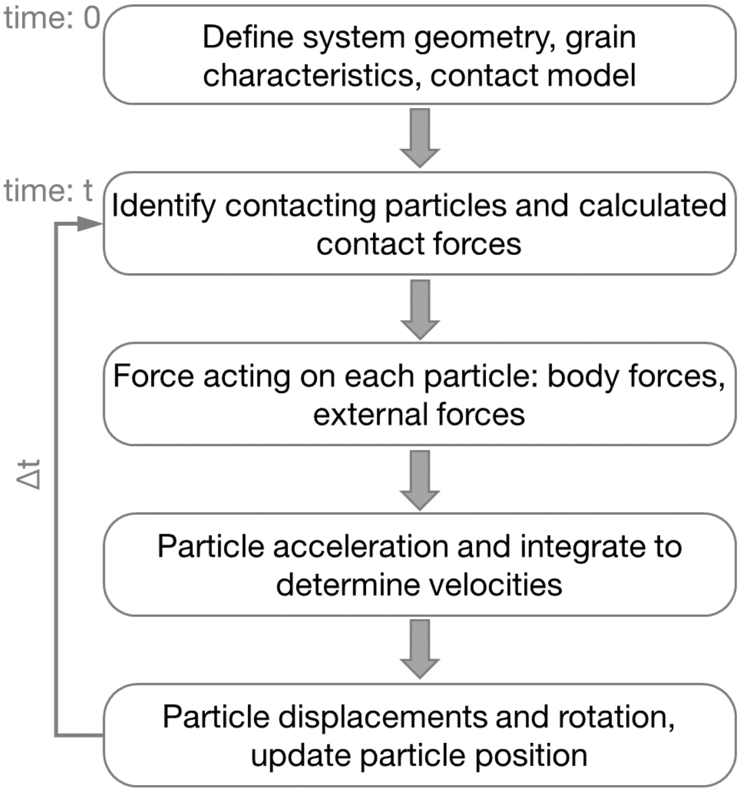

Figure 4.3 Calculation sequence within a DEM time step.

Figure 4.3 shows the calculation series that occur within a given time step. Particle velocities and incremental displacements are the first to be calculated. Here, the equilibrium of each particle in the sequence is considered. In the second series of calculations, upon the system geometry being updated, the forces at each contact in the whole system are then calculated. Particle rotational moment is produced from the normal contact force as well as the tangential component of the contact force. As the output of these calculated moments and forces, the new particle position is generated for the next time step, and the series of calculation begins again. For every particle-based DEM simulation, the following fundamental assumptions are accepted. The first consideration is that particles are rigid, each possessing finite inertia that can be described analytically. Moreover, the particles can translate and rotate independently of each other. The detections of new particle contacts are automatically completed by a geometry check algorithm. Physical contacts of particles normally happen over an infinitesimally small area based on the allowed overlapping and consist of only two particles. Particles that interact in DEM simulations are authorized to overlap slightly at the contact point, where the magnitude of the overlap is required to be small. The compressive inter-particle forces can be calculated from the particles overlapping value. Tensile and compression forces can be transferred at particle contact points normal to the direction of contact, as well as a tangential force orthogonal to the normal contact force. Furthermore, there is a distance between two separating particles where the tensile inter-particle forces are calculated. When particles collide, this force is its maximum value, and then the particles move away from each other, which also means that the contact area reduces to zero and is no longer used in contact force calculations. The last key assumption is that clusters of the rigid base particles can be used to represent a single particle. A measurable deformation of the composite particles is caused by the relative motion of the base particles within the cluster. These particle agglomerates may also be rigid themselves.

Defining a simulation time step is one of many essential steps in setting up the DEM. Sufficiently short time steps ensure the stability of the system and enable stimulation of the real processes. According to Cundall and Strack (1979) and Johnson (1974), disturbances that occur during motion of particles in a granular system propagate following the Rayleigh waves form along the surface of solid. The simulation time step is included in the Rayleigh time, which is the time the energy wave takes to transverse the smallest element in the system. The simulation time step should be small enough so that any disturbance of a particle's motion only propagates to its nearest neighbors. Velocity and acceleration are assumed to be constant during the time step. Moreover, the time step duration should be smaller than the critical time increment evaluated from theory. Several equations have been proposed for calculating a critical time step (Cundall and Strack, 1979). Thus, this study applied a time step of 0.00001s, which is smaller than 20 percent of the Rayleigh time.

This study used the Open Source Software LIGGGHTS (LAMMPS[1] Improved for General Granular and Granular Heat Transfer Simulations) and implemented a new Hertz–Mindlin granular contact model (Johnson, 1974; Landau and Lifshitz, 1986; Mindlin, 1949), where grains are modeled as compressible spheres with a diameter d that interacts when in contact via the Hertz–Mindlin model (Johnson, 1974; Landau and Lifshitz, 1986; Mindlin, 1949). Algorithms were developed to calculate grain size distribution and porosity from the calculated results of location and diameter of grains.

---

[1] Large-scale Atomic/Molecular Massively Parallel Simulator.

4.2.1 Algorithms for calculating size distribution and porosity of a cross section from DEM results

The results obtained from LIGGGHTS contains 3D locations and diameter of grains. To calculate the porosity and grain size distribution, a simple algorithm was developed. Using K different planes with elevations z_k $(k = 0,..,K)$, which intersect the spherical grain matrix. The diameter of the generated circle i $(i = 1,..,n_k)$ is dependent on the spherical diameter and the relative position between the k plane and grain i (Figure 4.4).

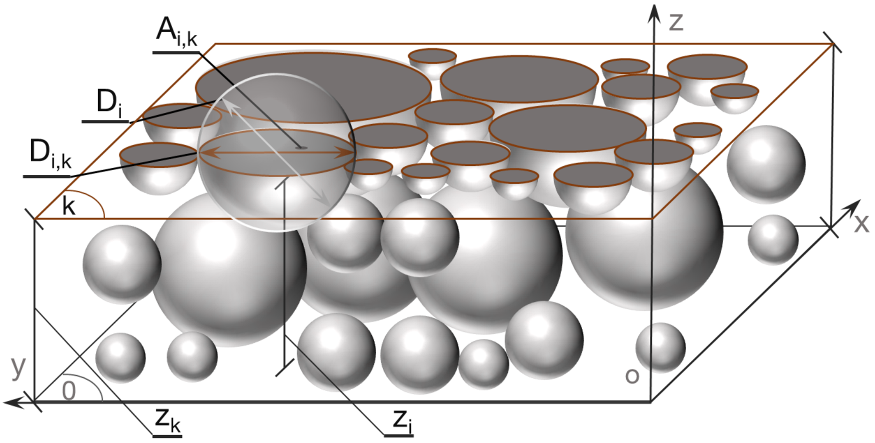

Figure 4.4 Calculation parameters of the generated circle by k-plane across grain matrix.

The diameter of each circle created by the intersection between plane k and grain i^{th} is calculated as:

$$D_{i,k} = \sqrt{D_i^2 - 4\left(z_k - z_i\right)^2} \qquad if\ \ z_i - \frac{D_i}{2} \leq z_k < z_i + \frac{D_i}{2} \tag{4.5}$$

Total solid area ($A_{s,k}$) of all n_k grains in plane k is determined:

$$A_{s,k} = \sum_{i=1}^{n_k} A_{i,k} = \sum_{i=1}^{n_k} \frac{\pi D_{i,k}^2}{4} \tag{4.6}$$

The total area A_t is calculated based on the shape generated by the plane k cut across the grain channel, whereby, the porosity of cross section k is calculated by the following equation:

$$p_k = 1 - \frac{A_{s,k}}{A_t} \tag{4.7}$$

To calculate the grain size distribution, the grains in cross-section k are divided into m_k size fractions with characteristic grain size D_j $(j = 1,\dots,m_k)$ and $D_{j-1} < D_j$, then the area of each fraction is calculated:

$$A_j^{(k)} = \sum_{i=1}^{n_{j,k}} \frac{\pi D_{i,k}^2}{4} \ \ if \ \ D_{j-1} \le D_{i,k} < D_j \tag{4.8}$$

With

$$\sum_{j=1}^{m_k} n_{j,k} = n_k \tag{4.9}$$

The fraction of class j in cross-section k is calculated by the following equation:

$$\beta_j^{(k)} = \frac{A_j^{(k)}}{\sum_{i=1}^{m_k} A_i^{(k)}} \tag{4.10}$$

4.2.2 Exchange rate of fine sediment and time normalization

In DEM executed by LIGGGHTS, the locations and number of the fine sediments are updated in every time step and dumped in result files. From this result, simple equations are developed to calculate the exchange rate of fine sediment in gravel-bed (so called exchange rate) that describes the ratio of the number of the fine sediments trapped to the total number of sediment fed. Hence, for the sample j^{th}, three exchange rates were defined for the 2 layers gravel-bed model included: the exchange of surface layer $E_{j,sur}^t$, the exchange of subsurface layer $E_{j,sub}^t$ and total exchange rate $E_{j,tot}^t$ by the following equations:

$$E_{j,sur}^t = \frac{N_{j,sur}^t - N_{j,sur}^{t-1}}{n_{j,fed}^t} \tag{4.11}$$

$$E_{j,sub}^t = \frac{N_{j,sub}^t - N_{j,sub}^{t-1}}{n_{j,fed}^t} \tag{4.12}$$

$$E^t_{j,tot} = \frac{N^t_{j,tot} - N^{t-1}_{j,tot}}{n^t_{j,fed}} \tag{4.13}$$

In which, $N^t_{j,sur}$ and $N^{t-1}_{j,sur}$ are the number of grain trapped in surface layer at time t and $t-1$; $N^t_{j,sub}$ and $N^{t-1}_{j,sub}$ are the number of grain trapped in surface layer at time t and $t-1$; $N^t_{j,sub}$ and $N^{t-1}_{j,sub}$ are the number of grain trapped in two layers at time t and $t-1$; $n^t_{j,fed}$ total number of grain is fed from time $t-1$ to time t.

In the conducted samples for investigating exchange rate, the simulation time is significantly different, (for example, the large size ratio of fine and coarse grain ($d/D = 0.45$) has the simulation time of 15 minutes, however, with the small size ratio ($d/D = 0.1$) the simulation time is up to 15 hours). In order to facilitate comparison, time simulation is normalized by defining the time for start exchange as 0 and the ended time simulation as 1. The normalized time for sample j^{th} at time step k is calculated by:

$$t^k_j = \frac{T^k_j - T^B_j}{T^E_j - T^B_j} \tag{4.14}$$

In which, T^B_j is the time step at beginning of the infiltration process, T^E_j is the time step at end of the infiltration process of the sample j^{th}; T^k_j is the time step k of the infiltration process of the sample j^{th}.

4.2.3 Pore distribution using Watershed Segmentation

Watershed segmentation (WS) is an advanced approach that detects grains and outputs the average size. Such a method is widely used in object boundary detection and image segmentation in computer science, which has been used for characterization of rock structures. Sheppard, Sok, and Averdunk (2004) used a coupling of the watershed and active contour methods to segment grayscale distance maps attained through transforming binary images. Since image noise influences the WS method, an anisotropic diffusion filter, which removes noise but keeps important visual features, was used. The WS algorithm was used by Ketcham (2005) to separate visually connected particles and extract the size distributions and the orientation of particle contacts from high-resolution X ray images. Wildenschild and Sheppard (2013) made use of the WS method to divide the granular space of an unconsolidated sand sample and the void space. Through estimating the size of the extracted pores and grains, it is possible to obtain the pore and grain networks of porous media. Rabbani, Jamshidi, and Salehi (2014) employed a 3D city block distance function in combination with the WS algorithm in order to separate connected pores found in the rock structure and estimate the pores average size, which is integral in the construction of a pore network. The same practice is applied in this study to partition connected grains in 2D binary images (Rabbani and Ayatollahi, 2015).

Pore distribution of gravel-bed river plays a vital role for analyzing the fine sediment infiltration. To determine the pore distribution, Watershed Segmentation to analyze the cross section images (Rabbani and Ayatollahi, 2015) was used in this study. The Watershed Segmentation method is a useful tool capable of detecting and distinguishing objects that touch in images. A traditional way to produce edge images is by applying a gradient and then a threshold to the outputted images to generate a binary edge image. Malpica et al. (1997) claim the watershed algorithm is a fast and efficient technique to segment and separate combined clusters of objects. The watershed algorithm becomes most applicable for processing grayscale or gradient images; however, its use in segmenting binary images by converting binary images to grayscale using distance transformation is also valid. To better understand this algorithm, think about two objects that touch as shown in Figure 4.5. This study aims to detach these pores via the Watershed Segmentation method.

First, distance transform on our binary image must be applied. The pixel brightness as described in the distance transformation is solved by determining the distance between that point and the nearest pixel of the object's boundary (Figure 4.5b). Numerous formulas exist to calculate this distance including Euclidean, city block, and chessboard. Rabbani, Jamshidi, and Salehi (2014) discovered that the city block distance transforms used before watershed results in more effective segmentation of the porous rock images into two and three dimensions. Secondly, one must convert the distance map into a topological surface where brighter pixels indicate deeper parts of that surface (Figure 4.5c). Therefore, a basin is formed for each of the objects in the image. Accumulation of water begins in the deepest part of the basin as per the depth contours (Figure 4.5d). As flooding persists, the water level rises in the basins until two previously isolated water pools converge with each other. When water pools of two different basin encounter each other, the pixel location is denoted as the watershed ridge line. At the completion of the flooding process, all watershed ridge line pixels are detected. At this point, the watershed ridge line separates the two touching objects (Figure 4.5e). As previously mentioned, brighter pixels in the distance map signify points farther from the boundary of an object. In this study, the city block distance formula was used to create the distance map. For two points with x and y coordination, the city block formula can be written as follows: City block distance $= |x_1 - x_2| + |y_1 - y_2|$.

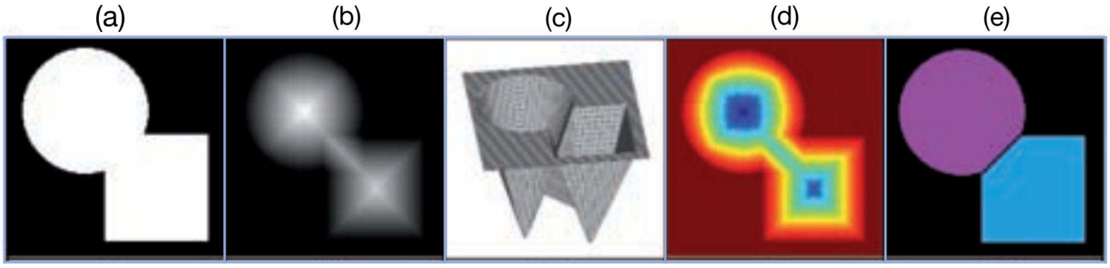

Figure 4.5 Sample segmentation using the watershed method: (a) original binary image; (b) grayscale distance map; (c) topological surface; (d) depth contours; (e) detected objects separated by the watershed ridge line (Rabbani and Ayatollahi, 2015).

4.2.4 Transferred coefficient

The infiltration process of fine sediment into void space of gravel-bed strongly depends on the size of the void, which is dependent on unusual geometries of the matrix that exhibit various void fractions. Allen (1982) states that for cubic, orthorhombic and rhombohedral packing arrangements of spherical particles, the void fractions are 0.48, 0.40 and 0.26, respectively, while values of D/d_l (when d_l is the largest circle diameter that fits into the voids) are 1.37, 1.90 and 2.41, respectively. The most densely packed arrangement for spheres results in a void fraction approximately equal 0.26 (Hales, 2005). That being said, it is difficult to achieve this packing arrangement in a real system. In contrast, the packing arrangement with the loosest packing, in which the system is still stable, was presented in Onoda and Liniger (1990) and has a void fraction of roughly 0.45; this state is termed ‘random loose packing’. Amongst these two extremes, the term ‘random close packing’ was defined by Scott and Kilgour (1969). As spheres randomly arranged in a rigid container and vibrated to guarantee maximum packing; this has a void fraction of about 0.36.

In this study, the pore size of gravel bed was used as a factor influencing the fine sediment infiltration process. However, it differs from previous researchers (Peronius and Sweeting, 1985; Allen, 1982; Valdes and Santamarina, 2008) who used the pore size definition as the largest circle diameter that fits into the voids. This study results from the Watershed Segmentation method, the pore size is defined as the diameter of the circle that has the same area with the void space (so-called equivalent area). For convenient comparison of these results to the previous studies, the transferred coefficient can be used to convert between the two definitions of pore size mentioned above. To evaluate the range of the transferred coefficient (R), This study considered the range of ’close packing’ (cubical packing) and of ’loose packing’ (tetrahedral packing) (Figure 4.6).

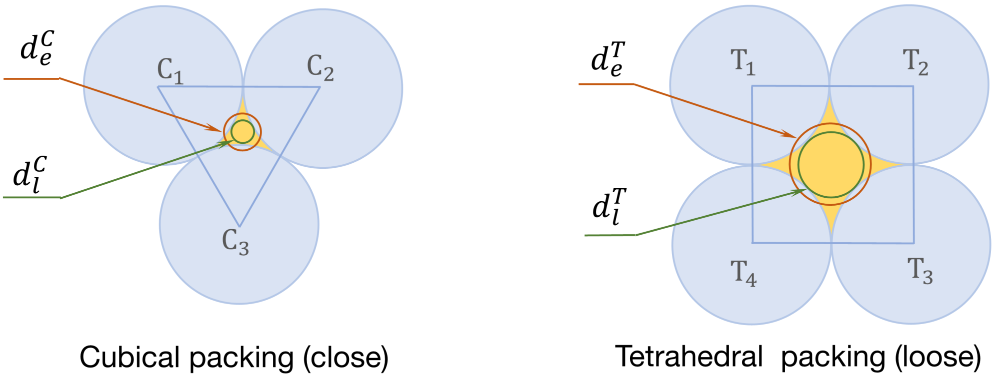

Figure 4.6 Calculation of the transferred coefficient from the equivalent area diameter to the largest diameter that fits into the voids.

Areas of void space of cubical $\left(A_{void}^C\right)$ and tetrahedral packing $\left(A_{void}^T\right)$ are calculated by following equations:

$$A_{void}^C = \frac{D^2\sqrt{3}}{4} - \frac{\pi D^2}{8} = \frac{2\sqrt{3}-\pi}{8}D^2 \tag{4.15}$$

$$A_{void}^T = D^2 - \frac{\pi D^2}{4} = \frac{4-\pi}{4}D^2 \tag{4.16}$$

The diameters are defined by the equivalent pore area of cubical $\left(d_e^C\right)$ and tetrahedral packing $\left(d_e^T\right)$:

$$d_e^C = \sqrt{\frac{A_{void}^C}{\frac{\pi}{4}}} = \sqrt{\frac{A_{void}^C}{\frac{\pi}{4}}} = \sqrt{\frac{2\sqrt{3}-\pi}{2\pi}}D = 0.227D \tag{4.17}$$

$$d_e^T = \sqrt{\frac{A_{void}^T}{\frac{\pi}{4}}} = \sqrt{\frac{4-\pi}{\pi}}D = 0.523D \tag{4.18}$$

The largest diameters are fitted in a pore of cubical $\left(d_l^C\right)$ and tetrahedral packing $\left(d_l^T\right)$:

$$d_l^C = 2\left(\frac{2}{3}D\frac{\sqrt{3}}{2} - \frac{D}{2}\right) = \frac{2\sqrt{3}-3}{3}D = 0.155D \tag{4.19}$$

$$d_l^T = \left(\sqrt{2}-1\right)D = 0.414D \tag{4.20}$$

Transferred coefficients for cubical packing $\left(R^C\right)$ and tetrahedral packing $\left(R^T\right)$ are calculated by following equations:

$$R^C = \frac{d_e^C}{d_l^C} = \frac{0.227D}{0.155D} = 1.46 \tag{4.21}$$

$$R^T = \frac{d_e^T}{d_l^T} = \frac{0.523D}{0.414D} = 1.26 \tag{4.22}$$

Transferred coefficient range from 1.26 to 1.46 for loose packing and close packing respectively. However, the transferred coefficient is also dependent on the shape and the deformation that were not considered in this calculation.

4.3 Artificial Neural Network

4.3.1 Introduction

In recent decades, Artificial Neural Network (ANN), a computational intelligence technique, has been emerged as a powerful tool for handling complex geoscience, morphology problems (Bui, Kaveh, and Rutschmann, 2015; Saljooghi and Hezarkhani, 2014). In this study, ANN is applied to predict the characteristics of gravel bed included porosity and grain fraction of gravel bed. Porosity prediction using ANN mostly originates from the field of petroleum engineering to investigate carbonate reservoirs based on well-log data (using the acoustic, nuclear, resistivity technology, sonic transit time and density logs to obtain the porosity indirectly) (Bagheripour and Asoodeh, 2013; Kraipeerapun, Fung, and Nakkrasae, 2009; Link and Himmer, 2003). Because of using indirect measurement methods and using many conversation formulas (Saljooghi and Hezarkhani, 2014), porosity data obtained by well-log data has high errors and low resolution (a porosity value is usually calculated for a layer thickness of several meters). These prevented the application of ANN in predicting porosity of a gravel-bed river where bed thickness is much smaller than carbonate reservoirs. However, with a high resolution of data, the porosity prediction from ANN enables us to overcome two weak points of empirical and theoretical porosity prediction in gravel-bed rivers, including limited multi controlling factor, and computation time.

Artificial Neural Network (ANN) is a general term encompassing many different network architectures. A Feed-forward Neural Network (FNN) is an artificial neural network where connections between nodes do not form a cycle. FNN is the first and simplest type of artificial neural network developed. Information of an FNN travels in only one direction, forward, from input nodes, through hidden nodes to then the output nodes. Further, the most widely used FNN is a multilayer perceptron (MLP). An MLP model contains several artificial neurons otherwise known as processing elements or nodes. A neuron is a mathematical expression that filter signals traveling through the net. An individual neuron receives its weighted inputs from the connected neurons of the previous layer, which are normally aggregated along with a bias unit. The bias unit is purposed to scale the input to a useful range to improve the convergence properties of the neural network. The combined summation is delivered through a transfer function to generate the neuron output. Weighted connections modify the output as it is passed to neurons in the next layer, where the process is repeated. The weight vectors that connect the different network nodes are discovered through the so-called error back-propagation method. During training, these parameters values are varied in order for the FNN output to align with the measured output of a known dataset (Bhattacharya, Price, and Solomatine, 2007; Haykin and Network, 2004). Changing the connection weights in the network according to an error minimization criterion achieves a trained response. Overfitting is avoided if a validation process is implemented during the training. When the network has been sufficiently trained to simulate the best response to input data, the network configuration is fixed and a test process is conducted to evaluate the performance of the FNN as a predictive tool (Bui, Kaveh, and Rutschmann, 2015).

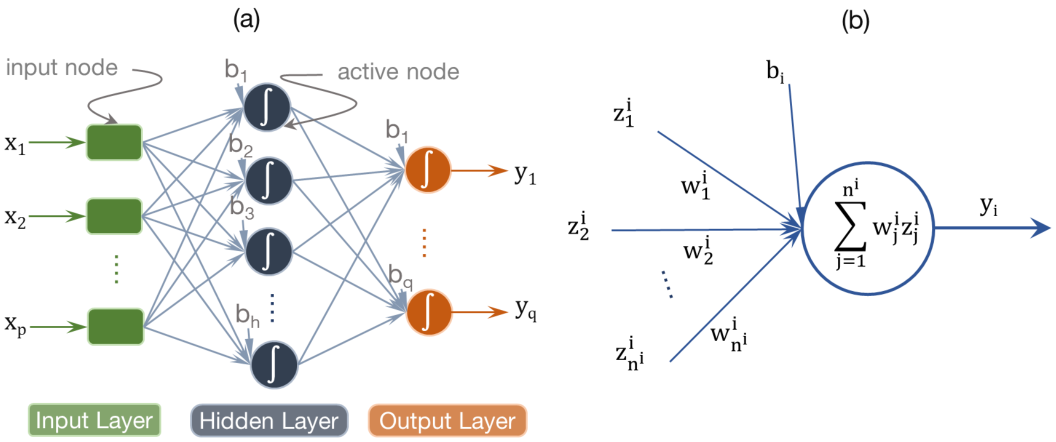

Figure 4.7 Three-layer feedforward neural network (a), where input layer has p input nodes, hidden layer has h activation functions, and output layer has q nodes. A node of the network (b).

4.3.2 Feed-forward neural networks

In feed-forward networks (Figure 4.7), messages are passed forward only. A network with L layers has a parameter $W^{(l)} \in R^{d_l \times d_{l-1}}$ and a differential function $f^{(l)} : R^{d_1} \rightarrow R^{d_1}$ corresponding to the l^{th} layer (Stratos, 2019). Given an input $x \in R^{d_o}$, the network outputs:

$$y := a^{(L)} \tag{4.23}$$

where each $a^{(l)} \in R^{d_l}$ is define is defined recursively from the base case $a^{(0)} := x$ as follows (Stratos, 2019):

$$z^{(l)} := W^{(l)} a^{(l-1)};\ a^{(l)} :=\ f^{(l)} z^{(l)} \tag{4.24}$$

The training process minimizes a loss function $l :\ \ R^{d_L \times d_L}\ \rightarrow R$ over labeled examples (x, y) (Stratos, 2019). The gradient of the squared loss on (x, y) with respect to $W(L)$ is

$$\frac{\partial}{\partial W^{(L)}} \left[\frac{1}{2} \left\| y - a^{(L)} \right\|^2 \right] = \left[\left(a^{(L)} - y \right) \odot f^{(L)'} z^{(L)} \right] \left(a^{(L-1)} \right)^T \tag{4.25}$$

the form mirrors the delta rule because $a^{(L)} = f^{(L)} \left(W^{(L)} a^{(L-1)} \right)^T$ where $a^{(L-1)}$does not involve $W^{(L)}$. By defining the "error term"

$$\delta^{(L)} := \left(a^{(L)} - y \right) \odot f^{(L)'} \left(z^{(L)} \right) \tag{4.26}$$

Equation (4.25) can be simplified as $\delta^{(L)} \left(a^{(L-1)} \right)^T$ (Stratos, 2019). Similarly, the gradient with respect to $W^{(l)} for\ l < L$ can be verified to be $\delta^{(l)} \left(a^{(l-1)} \right)^T$ where

$$\delta^{(l)} := f^{(l)'} \left(z^{(l)} \right) \odot \left(W^{(l+1)^T} \delta^{(l+1)} \right) \tag{4.27}$$

Computation of all gradients in a multi-layer network is commonly known as "backpropagation", which is a special case of automatic differentiation. For concreteness, here is the backpropagation algorithm for an L layer feedforward network with the squared l_o. Input labeled example $(x, y) = R^{d_L} \times R^{d_L}$ parameters $\left\{ W^{(l)} \right\}_{l=1}^{L}$ (Stratos, 2019). Output:

$$\bar{W}^{(l)} := \frac{\partial}{\partial W^{(L)}} \left[\frac{1}{2} \left\| y - a^{(L)} \right\|^2 \right] for\ l = 1 \ldots L \tag{4.28}$$

Feedforward phase:
Set $a^{(0)} \leftarrow$ x, and for $l = 1 \ldots L$ compute:

$$z^{(l)} \leftarrow W^{(l)} a^{(l-1)} a^{(l)} \leftarrow f^{(l)} z^{(l)} \tag{4.29}$$

Backpropagation phase:
Set $\delta^{(L)} \leftarrow \left(a^{(L)} - y\right) \odot f^{(L)'} \left(z^{(L)}\right)$, and for $l = L-1 \ldots 1$ compute:

$$\delta^{(l)} \leftarrow f^{(l)'} \left(z^{(l)}\right) \odot \left(W^{(l+1)^T} \delta^{(l+1)}\right) \tag{4.30}$$

Set $\bar{W}^{(l)} \leftarrow \delta^{(l)} \left(a^{(l-1)}\right)^T$, and for $l = 1 \ldots L$:

4.3.3 Optimization algorithm

The optimization algorithm (or optimizer) is the main approach used for training a machine learning model to minimize its error rate. There are two metrics to determine the efficiency of an optimizer: speed of convergence (the process of reaching a global optimum for gradient descent); and generalization (the model's performance on new data). Popular algorithms such as Adaptive Moment Estimation (Adam) or Stochastic Gradient Descent (SGD) can capably cover one or the other metric. The Adam optimizer, presented by Kingma and Ba (2014), is extensively used for deep learning models requiring first-order gradient-based descent with small memory and the ability to compute adaptive learning rates for different parameters (Jangid and Srivastava, 2018). This method is computationally efficient, easy to implement and has proven to perform better than the RMSprop and Rprop optimizers (He et al., 2018). Gradient rescaling is reliant on the magnitudes of parameter updates. The Adam optimizer does not require a stationary object and can work with more sparse gradients. The decaying averages of past and past squared gradients m_t and v_t respectively is calculated based on (Kingma and Ba, 2014) as follows :

$$m_t = \beta_1 m_{t-1} + (1 - \beta_1) g_t \tag{4.31}$$

$$v_t = \beta_2 v_{t-1} + (1 - \beta_2) g_t^2 \tag{4.32}$$

m_t and v_t are estimates of the first moment (the mean) and the second moment (the uncentered variance) of the gradients respectively. m_t and v_t are initialized as vectors of 0. The authors of Adam noticed that they are biased towards zero, particularly during the initial time steps and during smaller decay rates (i.e. β_1 *and* β_2 are close to 1). Bias-corrected first and second moment estimates are computed to counteract these biases (Kingma and Ba, 2014):

$$\hat{m}_t = \frac{m_t}{1-\beta_1^t} \tag{4.33}$$

$$\hat{v}_t = \frac{v_t}{1-\beta_2^t} \tag{4.34}$$

Parameters are then updated by:

$$\theta_{t+1} = \theta_t - \frac{\eta}{\sqrt{\hat{v}_t}+\varepsilon_1}\hat{m}_t \tag{4.35}$$

The default value in this study: $\beta_1 = 0.9$, $\beta_2 = 0.999$ and $\varepsilon = 10^{-8}$ with learning rate $\eta =$ 0.001. More detail about this method is available in Kingma and Ba (2014).

4.3.4 Model evaluation

According to the suggestion of Legates and McCabe Jr (1999), a perfect evaluation of the model performance should include at least one goodness-of-fit or relative error measure (i.e, correlation coefficient, R) and at least one absolute error measure (i.e. root mean square error, $RMSE$ or mean absolute error, MAE). This study employs a range of statistical measures to evaluate the performance of our new model, including R, $RMSE$, and MAE as formulate.

The measures of correlation coefficient (R), root mean square error ($RMSE$), and mean absolute error (MAE) are used to evaluate the performance of these two models, and are formulated in equations:

$$R = \frac{n\sum_{i=1}^{n}(x_i y_i) - \left(\sum_{i=1}^{n} x_i\right)\left(\sum_{i=1}^{n} y_i\right)}{\sqrt{\left[n\sum_{i=1}^{n} x_i^2 - \left(\sum_{i=1}^{n} x_i\right)^2\right]\left[n\sum_{i=1}^{n} y_i^2 - \left(\sum_{i=1}^{n} y_i\right)^2\right]}} \tag{4.36}$$

$$RMSE = \sqrt{\frac{1}{n}\sum_{i=1}^{n}(x_i - y_i)^2} \tag{4.37}$$

$$MAE = \frac{1}{n}\sum_{i=1}^{n}|x_i - y_i| \tag{4.38}$$

where: n is the number of measurements, x_i is calculated value i^{th}, y_i represents the measured value i^{th}. The R expresses degree of similarity between predicted and actual where values closer to 1 indicate greater similarity and values close to -1 indicate the opposite. $RMSE$ on the other hand represents the average distance of a data point from the fitted line measured along a vertical line, while MAE indicates how close predictions are to the measured outputs. Low $RMSE$ and MAE values indicate high confidence in the model-predicted values.

Chapter 5

A new numerical model for modelling sediment transport in gravel-bed rivers

5.1 Introduction

In gravel-bed rivers, depending on the hydraulic parameters, the incoming sediment distribution, and the bed composition, some particle sizes may be eroded while others deposited or immovable. More importantly, the transport rate of the coarse size-fractions may be different from the transport rate of the fine size-fractions. Consequently, several different processes may occur. For example, under high-flow conditions all the finer particles may be eroded, leaving a layer of coarser particles. Only when the flow is unable to carry the coarse particles will no more erosion occur. Inversely, under low-flow conditions, sediment transport can cause extensive fine sediment infiltration into void spaces in coarse bed material, which is known as colmation process. It is no doubt that porosity of bed material is not constant and plays an important role in the fluvial geomorphology as well as in the river ecosystem.

To model sediment transport processes as well as bed deformation, multi-layer models were applied for graded sediment transport. Despite the considerable variations of porosity, most of the conventional models assumed that the porosity of bed material is constant.

Parts of this chapter were published as:

Bui, V.H.; Bui, M.D.; Rutschmann, P. Advanced Numerical Modelling of Sediment Transport in Gravel-Bed Rivers. Water 2019, 11, 550, doi:10.3390/w11030550.

Bui, V.H.; Bui, M.D.; Rutschmann, P. A new numerical model for sediment transport in gravel-bed river. Proc. of the 5th IAHR Europe Congress — New Challenges in Hydraulic Research and Engineering. 2018, 723-725, Italy, doi:10.3850/978-981-11-2731-1_189-cd.

Therefore, sediment transport in the form of infiltration into the void spaces of the coarse bed, or fine particles in sublayers and the entrainment of fine sediment into flow from the substrates, is not taken into account. This assumption can be inappropriate for simulating the sediment transport and bed variation in gravel-bed rivers. Toro-Escobar, Parker, and Paola (1996) accounted for this process in terms of an appropriate transfer or exchange function at the interface between the surface layer and substrate. Based on the data from a large-scale experiment on the aggradation and the selective deposition of gravel, they proposed an empirical form for the transfer function, where material that is transferred to the substrate can be represented as a weighted average of bed load and surface material, with a bias toward bed load. Applying this function with the assumption of a constant porosity, Cui (2007) developed a numerical model for sand entrainment/infiltration from/into the subsurface. The model was applied to study the dynamics of grain size distributions, including the fractions of sand in sediment deposits and on the channel bed surface. Hirano (1971) has presented a bed variation model for sediment mixtures and pointed out this necessity of considering the change of porosity in some cases. Further, Sulaiman, Tsutsumi, and Fujita (2007a) proposed an approximated bed variation model while considering the change in bed porosity, where the thickness of each layer is assumed to be constant and equal. Furthermore, the exchange between bed material and the transported sediment only takes place on the surface layer, and sediment transport from an upper layer to the lower layer is neglected. These assumptions are improper in gravel-bed rivers, where finer sediment possibly drops into the subsurface layer.

This chapter presents an effort to develop a numerical hydromorphological model considering the bed porosity change and exchange of fluxes of fine sediment between two different bed layers in which the relationship between the grain size distribution and the porosity, the exchange of fine sediment between layer, could be determined by the combination framework of Discrete Element Method and Artificial Neural Network introduced in Chapter 4. The proposed model for exchange processes of bed material and transport sediment on the surface layer and subsurface layer is introduced to obtain the time and space variations of the bed level, grain size distribution, and bed porosity.

5.2 Sediment transport and bed variation module

The size-fraction method is applied to divide bed material into some size-fractions. Each fraction is characterized by average grain size and volume percentage of occurrence in the bed material and presented these components as the probability of a different group.

Applying the so-called multi-layer concept, I divide the vertical bed structure into different layers. Figure 5.1 shows a diagram of this structure consisting of one active layer and several substrate layers. Sediment particles are continuously exchanged between flow and the active layer; sediments in this layer can be transported as bed load, suspended load, or infiltration. Furthermore, they can move between the active layer and sublayers depending mostly on the bed porosity and grain size distribution as will be discussed below. Fine particles in the top substrate (2) may also be attracted to the surface layer and entrained flow.

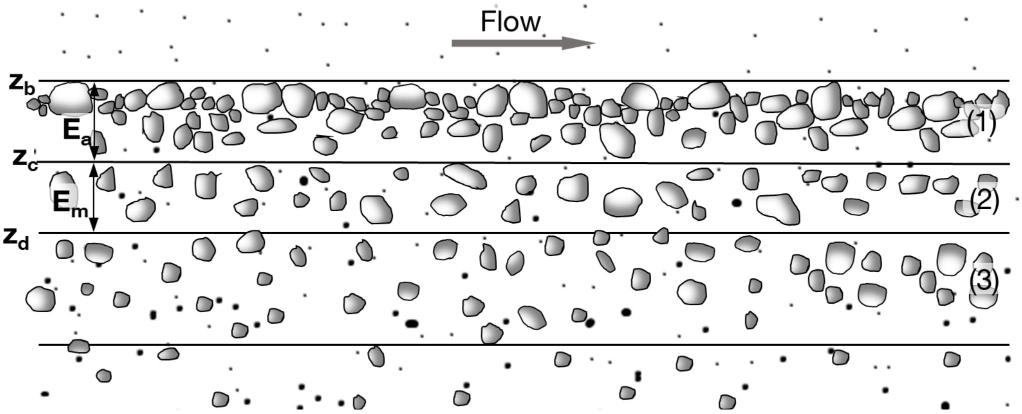

Figure 5.1 The structure diagram of the vertical cross-section is based on the multi-layers model. (1) = active layer; (2) and (3) = substrate layers; E_a and E_m = Active layer thickness and active-stratum layer thickness; z_b = bed elevation; z_c and z_d = substrate elevations.

Riverbed morphology in nature can be related to all three types of sediment transport mentioned above (bed load, suspended load and infiltration of fine sediment). When the settling velocity of sediment particle is more significant than critical shear stress velocity, sediment particle only moves in the forms of bed load or infiltration. In this study, three following hypothesises were used:

1. The horizontal surface is unchanged ($Z_d = 0$), so sediment sorting occurs only in the active layer (1) and the upmost sublayer (2).
2. The bed sediment is moving under two forms: infiltration or bed load.
3. The flow and sediment transport are one-dimensional. The horizontal exchange surface is assumed as unchanged, so sediment sorting occurs only in the active layer and sublayers and $Z_d = 0$.

5.2.1 Bed elevation

The change in the bed elevation is calculated using the law of continuity of bed sediment in the active layer:

$$\frac{\partial}{\partial t}\left[\int_0^{z_b}(1-p)\,dz\right]=-\frac{\partial q_b}{\partial x} \tag{5.1}$$

Where x = The coordinate axis along the flow direction; z = The coordinate axis along the vertical direction; t = time; $p = p(x,z,t)$ = bed porosity; $q_b = q_b(x,t)$ = specific volumetric bed load discharge. q_b and its fraction $q_{b,j}$ are determined by experiment or semi-experiment considering non-equilibrium bed load (Bui and Rutschmann, 2010). Further, Equation (5.1) can also be rewritten as:

$$\frac{\partial}{\partial t}\left[\int_0^{z_b-E_a}(1-p)\,dz+\int_{z_b-E_a}^{z_b}(1-p)\,dz\right]=-\frac{\partial q_b}{\partial x} \tag{5.2}$$

Applying the theorem of mean values and Leibniz integral rule for two finite integrals in the left-hand side of Equation (5.2) yields:

$$\frac{\partial\left[(z_b-E_a)(1-p_s)\right]}{\partial t}+\frac{\partial\left[E_a(1-p_a)\right]}{\partial t}=-\frac{\partial q_b}{\partial x} \tag{5.3}$$

In which $p_a = p_a(x,t)$ = the average porosity of active layer; $p_s = p_s(x,t)$ = the average porosity of sublayer layer (Figure 5.2).

$$\left[(z_b-E_a)\frac{\partial(1-p_s)}{\partial t}+(1-p_s)\frac{\partial(z_b-E_a)}{\partial t}\right]+\left[E_a\frac{\partial(1-p_a)}{\partial t}+(1-p_a)\frac{\partial E_a}{\partial t}\right]=-\frac{\partial q_b}{\partial x} \tag{5.4}$$

$$\left[-(z_b-E_a)\frac{\partial p_s}{\partial t}+(1-p_s)\frac{\partial z_b}{\partial t}-(1-p_s)\frac{\partial E_a}{\partial t}\right]+\left[-E_a\frac{\partial p_a}{\partial t}+(1-p_a)\frac{\partial E_a}{\partial t}\right]=-\frac{\partial q_b}{\partial x} \tag{5.5}$$

$$(1-p_s)\frac{\partial z_b}{\partial t}=-\frac{\partial q_b}{\partial x}+\left[(z_b-E_a)\frac{\partial p_s}{\partial t}+E_a\frac{\partial p_a}{\partial t}+(p_a-p_s)\frac{\partial E_a}{\partial t}\right] \tag{5.6}$$

We obtain bed level change considering porosity change in two layers:

$$(1-p_s)\frac{\partial z_b}{\partial t} = -\frac{\partial q_b}{\partial x} + S_p \tag{5.7}$$

$$S_p = \left[(z_b - E_a)\frac{\partial p_s}{\partial t} + E_a\frac{\partial p_a}{\partial t} + (p_a - p_s)\frac{\partial E_a}{\partial t}\right] \tag{5.8}$$

If the porosity of layers is constant, the porosity source term $S_p = 0$ and Equation (5.7) becomes the Exner equation. Therefore, Equation (5.7) can be considered as the expansion of the Exner equation, when considering the variation of porosity in space and time.

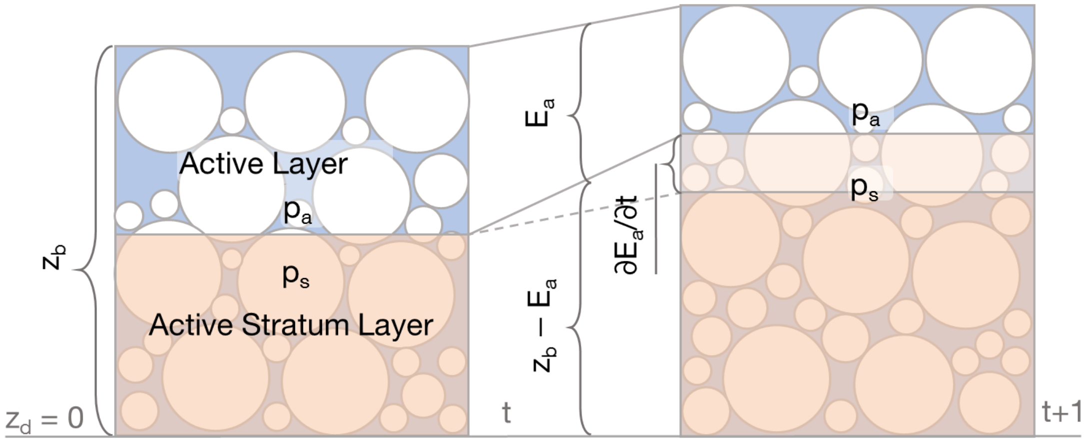

Figure 5.2 Bed level change due to porosity variation in different time steps.

5.2.2 Grain size distribution

Applying the law of continuity for each size fraction in bed composition:

$$\frac{\partial}{\partial t}\int_0^{z_b}(1-p)\,\beta_j dz = -\frac{\partial\left(q_j\right)}{\partial x} \tag{5.9}$$

$$q_j = \beta_{b,j} q_b;\;\; q_b = \sum q_j;\; \beta = \sum \beta_j \tag{5.10}$$

$$\frac{\partial}{\partial t}\int_0^{z_b-E_a}(1-p_s)\,\beta_{s,j}dz + \frac{\partial}{\partial t}\int_{z_b-E_a}^{z_b}(1-p_a)\,\beta_{a,j}dz = -\frac{\partial\left(\beta_{b,j}q_b\right)}{\partial x} \tag{5.11}$$

Where p_a is the porosity of the active layer, p_s is the porosity of the active stratum which $\beta_{a,j}$ = the size fraction j^{th} of sediment in the active layer; $\beta_{s,j}$ = the size fraction j^{th} of sediment in subsurface layer; and $\beta_{b,j}$ = the size fraction j^{th} of sediment transport in the form of bed load.

Assuming that the grain sorting in an active layer only occurs under the flow interaction and exchange process between the active layer and the active stratum layer and while applying the mass conservation law in the active layer, the equation for the change of size fraction is obtained, as below:

$$\frac{\partial}{\partial t}\left[\int_{z_b-E_a}^{z_b}\beta_{a,j}\left(1-p_a\right)dz\right]=-\frac{\partial\left(\beta_{b,j}q_b\right)}{\partial x}+S_{F,j} \tag{5.12}$$

Applying the theorem of mean values and Leibniz integral rule:

$$\frac{\partial\left[E_a\left(1-p_a\right)\beta_j\right]}{\partial t}=-\frac{\partial\left(\beta_{b,j}q_b\right)}{\partial x}+S_{F,j} \tag{5.13}$$

$$E_a\left(1-p_a\right)\frac{\partial\beta_j}{\partial t}+E_a\beta_j\frac{\partial\left(1-p_a\right)}{\partial t}+\left(1-p_a\right)\beta_j\frac{\partial E_a}{\partial t}=-\frac{\partial\left(\beta_{b,j}q_b\right)}{\partial x}+S_{F,j} \tag{5.14}$$

Equation (5.14) can be rewritten in the following form:

$$\frac{\partial\beta_{a,j}}{\partial t}=\frac{1}{E_a\left(1-p_a\right)}\left[\beta_{a,j}E_a\frac{\partial p_a}{\partial t}-\beta_{a,j}\left(1-p_a\right)\frac{\partial E_a}{\partial t}-\frac{\partial\left(\beta_{b,j}q_b\right)}{\partial x}\right]+\frac{S_{F,j}}{E_a\left(1-p_a\right)} \tag{5.15}$$

Based on the mass conservation and assuming that the grain sorting of the active stratum layer is caused by the exchange process between the surface layer and subsurface one, the following equation for the size fraction change in the subsurface layer is obtained:

$$\frac{\partial}{\partial t}\int_0^{z_b-E_a}\left(1-p_s\right)\beta_{s,j}dz=-S_{F,j} \tag{5.16}$$

Applying the theorem of mean values and Leibniz integral rule:

$$\frac{\partial\left[\left(z_b-E_a\right)\left(1-p_s\right)\beta_{s,j}\right]}{\partial t}=-S_{F,j} \tag{5.17}$$

$$(z_b - E_a)(1 - p_s)\frac{\partial \beta_{s,j}}{\partial t} + (z_b - E_a)\beta_{s,j}\frac{\partial (1 - p_s)}{\partial t} + (1 - p_s)\beta_{s,j}\frac{\partial (z_b - E_a)}{\partial t} = -S_{F,j} \tag{5.18}$$

Equation (5.18) can be rewritten in the following form:

$$\frac{\partial \beta_{s,j}}{\partial t} = \frac{1}{(z_b - E_a)(1 - p_s)}\left[\beta_{s,j}(z_b - E_a)\frac{\partial p_s}{\partial t} - \beta_{s,j}(1 - p_s)\frac{\partial (z_b - E_a)}{\partial t}\right] - \frac{S_{F,j}}{(z_b - E_a)(1 - p_s)} \tag{5.19}$$

In Equation (5.15), (5.19), the function $S_{F,j}$ expresses the exchange process of the active layer and sublayers of the size fraction j^{th}. Determining the $S_{F,j}$ value can be considered as the quantification of the bottom infiltration process. During degradation the active layer gain sediment from the subsurface, during the aggradation the bed load is deposited to the active layer and or subsurface according to the value of parameter c in the mixing model introduced by Hoey and Ferguson (1994) and adopted by Toro-Escobar, Parker, and Paola (1996).

Based on the empirical equation of Toro-Escobar, Parker, and Paola (1996):

$$\beta_{s,j} = c\beta_{a,j} + (1 - c)\beta_{b,j} \tag{5.20}$$

the following equation is obtained, which can be proposed to quantify the exchange between the active layer and active stratum layer for the fine fraction of size class j^{th} during aggradation:

$$S_{F,j} = \left[c\beta_{a,j} + (1 - c)\beta_{s,j}\right]\left\{\frac{\partial q_b}{\partial x} + \frac{\partial}{\partial t}\left[E_a(1 - p_a)\right]\right\} \tag{5.21}$$

During degradation, the Equation is based on the Hirano's research (Hirano, 1971):

$$S_{F,j} = \beta_{s,j}\left\{\frac{\partial q_b}{\partial x} + \frac{\partial\left[E_a(1 - p_a)\right]}{\partial t}\right\} \tag{5.22}$$

where coefficient c can be considered as a parameter of the model.

In semi-empirical Equations (5.21) and (5.22), the function $S_{F,j}$ depends on sediment discharge, size fraction of class j^{th}, bed porosity and active layer thickness. In Equations (5.15), (5.21) and (5.19), the bed porosity variation and the sediment exchange were considered to calculate the grain size distribution in two bed layers. Furthermore, the exchange rate, fine sediment distribution can also be obtained by using the framework of DEM and ANN proposed in Chapter 4.

Chapter 6

Results and Discussion

6.1 Overview

This chapter is divided into three main parts. In the first part, DEM simulation results are shown for investigating the porosity, exchange rate and fine fraction distribution of gravel-beds and comparing them with the experimental results. The ANN-results of porosity and fine fraction, trained by DEM data, are in the second part. The final part presents the simulated results of the new bed porosity variation for three straight flumes in comparison with the observed data in order to verify the improvement of the developed model.

Parts of this chapter were published as:

Bui, V.H.; Bui, M.D.; Rutschmann, P. A Combination of Discrete Element Method and Artificial Neural Network for Predicting Porosity of Gravel-Bed River. Water 2019, 11, 1461, doi:10.3390/w11071461.

Bui, V.H.; Bui, M.D.; Rutschmann, P. Advanced Numerical Modeling of Sediment Transport in Gravel-Bed Rivers. Water 2019, 11, 550, doi:10.3390/w11030550.

Bui, V.H.; Bui, M.D.; Rutschmann, P. The Prediction of Fine Sediment Distribution in Gravel-Bed River using a Combination of DEM and ANN. (submitting).

Bui, V.H.; Bui, M.D.; Rutschmann, P. Modeling infiltration process of fine sediment in gravel bed river. Proc. of Wasserbau-Symposium. 2018, 419-426, Austria.

Bui, M.D.; **Bui, V.H.**; Rutschmann, P. A new concept for modelling sediment transport in gravel bed rivers. Proc. of the 21st Vietnam Fluid Mechanics. 2018, Vietnam.

Bui, V.H.; Bui, M.D.; Rutschmann, P. A new numerical model for sediment transport in gravel-bed river. Proc. of the 5th IAHR Europe Congress — New Challenges in Hydraulic Research and Engineering. 2018, 723-725, Italy, doi:10.3850/978-981-11-2731-1_189-cd.

6.2 DEM simulation

6.2.1 DEM input parameters

The DEM simulations includes of seven cases: Two cases for porosity verification (Case 1, 2), one case for investigating the exchange rate (Case 3), and four cases (Case 4, 5, 6, 7) for verifying the infiltration process of fine sediment into gravel-bed of the DEM simulation. The DEM simulated results of Case-4, 5 and Case-6, 7 are used to generate data for porosity and fine fraction prediction.

Case-1: Numerical simulations are carried out for 13 cylinder containers with a diameter of 0.18 m. Each container is filled with uniform coarse grains with size D=1.0 mm and different fractions of the uniform fine grains with size d=0.14 mm, which are similar to the experiments conducted by McGeary (1961). Porosity for 13 different distributions are simulated by varying fraction of fine grains. The average height of the sediment layer is about 0.50 m.

Case-2: Only coarse grains with uniform size D = 8 mm are contained in a flume with 78.1 cm long, 32.9 cm wide and 23.3 cm high. The calculated results are compared with the experimental results of the gravel bed named ‘Run 1’ and ‘Run 2’ done by Navaratnam, Aberle, and Daxnerová (2018).

For simulating the exchange rate, one case is simulated with nine samples:

Case-3: The simulations consist nine square boxes: Coarse grains with uniform size D = 1.0 cm is filled in all nine boxes, fine grain with uniform sizes d = 0.45, 0.414, 0.40, 0.35, 0.30, 0.35, 0.30, 0.25, 0.20, 0.15, 0.10. cm are filled in boxes from 1 to 9 respectively.

For simulating the infiltration process, 4 cases were considered. Case 4 and 5 are comprised of a square box with edges of 0.15 m and a sediment layer thickness of 0.1 m for preparing porosity data. Case 6 and 7 are conducted in a rectangular flume with a length of 0.5 m, a hight of 0.2 m and a sediment layer thickness of 0.1 m for preparing fine fraction data.

Case-4 (Bridging-1): Fine sediment with a mean diameter of d_m = 0.353 mm and a standard deviation of $\sigma^{(d)}$ = 1.933; Gravel-bed with a mean diameter of D_m = 7.104 mm and a standard deviation of $\sigma(D)$ =1.375.

Case-5 (Percolation-1): Fine sediment with a mean diameter of d_m = 0.142 mm and a standard deviation of $\sigma^{(d)}$ = 1.837; Gravel-bed with a mean diameter of D_m = 7.482 mm and a standard deviation of $\sigma(D)$ = 1.324.

Case-6 (Bridging-2): Fine sediment with a mean diameter of d_m = 0.349 mm and a standard deviation of $\sigma^{(d)}$ = 1.98; Gravel-bed with a mean diameter of D_m = 7.427 mm and a standard deviation of $\sigma(D)$ =1.251.

Case-7 (Percolation-2): Fine sediment with a mean diameter of d_m = 0.235 mm and a standard deviation of $\sigma^{(d)}$ = 1.983; Gravel-bed with a mean diameter of D_m = 10.141 mm and a standard deviation of $\sigma(D)$ =1.462.

Case-4 and Case-5 are similar to experiments No. 2 and No. 3 respectively, conducted by Gibson et al. (2009a), Case-6 and Case-7 are similar to experiments No. 2 and No. 3 respectively, conducted by Gibson et al. (2011) with a very slow water flowrate, hence the effects of water flow on infiltration and packing processes can be neglected in the numerical model. The grain and water densities as well as four model parameters used in the DEM can be found in Table 6.1.

Table 6.1 Parameters for numerical simulation.

Sphere Density (kg/m^3)	Water Density (kg/m^3)	Young's modulus (Pa)	Poisson Ratio	Grain Friction	Restitution Coefficient
2350	1000	5.0x10^6	0.45	0.18-0.35	0.40

6.2.2 DEM verification for porosity

For simulating 13 samples of Case-1, the ratio of fine grain diameter to coarse grain diameter (d/D=0.14) was used. In the model, the vibration force with a wiggle amplitude of 0.001 m and a period of 0.06 s was applied to adjust the porosity. Figure 6.1a, b shows the 3D simulated results of 2/13 cylinder samples for the case without fine sediment and fine sediment fraction 0.4. Figure 6.1c shows the comparison between the measured and the calculated results for these 13 samples. There is a difference between DEM simulation and measurement: the line shape of DEM simulation results (diamond markers) is not as sharp as the measurement line (circle markers). This can be because the fine grain in DEM simulation did not completely fill in the void structure of coarse gravels due to the high friction coefficient of grain, and because of the short time and small amplitude of vibration. Another cause for the tolerance of the porosity in the simulation is the convex and concave surface of the cylinder, which may lead to an increase of porosity and therefore an increase in the total volume of the cylinder. However, in general, the agreement between DEM simulation and McGeary (1961) depicted that DEM performs well for porosity simulation (Table 6.2).

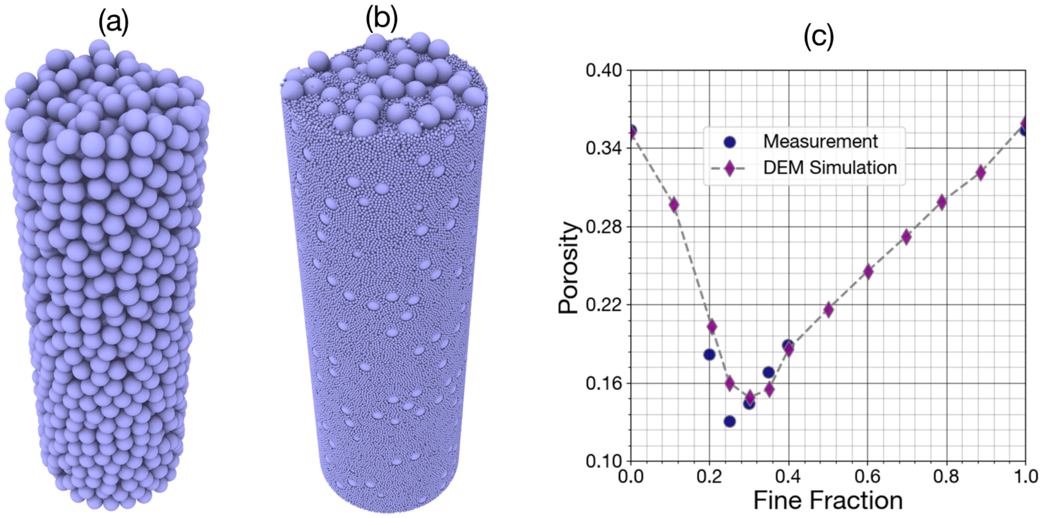

Figure 6.1 Porosity of packing of binary mixtures of spheres with size ratio (d/D=0.14) in comparison with McGeary (1961) porosity measurement.

Figure 6.2a shows the simulation result of the flume (Case-2) filled by uniform gravel with D = 8 mm. As can be seen in Figure 6.2b, DEM model provided a value of 0.47 for bulk porosity along the flume, which is slightly smaller than the measured porosity in ‘Run 1’ (0.48). Figure 6.2b shows the comparison of porosity variation by depth between DEM simulation and two experiments Run 1, Run 2 (Navaratnam, Aberle, and Daxnerová, 2018), where Run 2 has been carried out in a larger flume. At the surface and bottom of the flume, DEM porosity results agree with the measurement data. In the middle of flume elevation, DEM porosity results did not change as dramatically as the experimental results due to the absolute uniformity of diameters in simulation, which is very difficult to mimic in the experiment. In addition, in the middle of the flume elevation, DEM results are significantly smaller than the experimental porosity results. This can be explained by the fact that the uniform spherical grains used in DEM simulation, required for grain close packing are different from the irregular shapes of gravel used in the experiment for loose packing. In general, from the statistical performance (Table 6.2), DEM simulations are in good agreement with the experimental porosity measurement in gravel-bed flume.

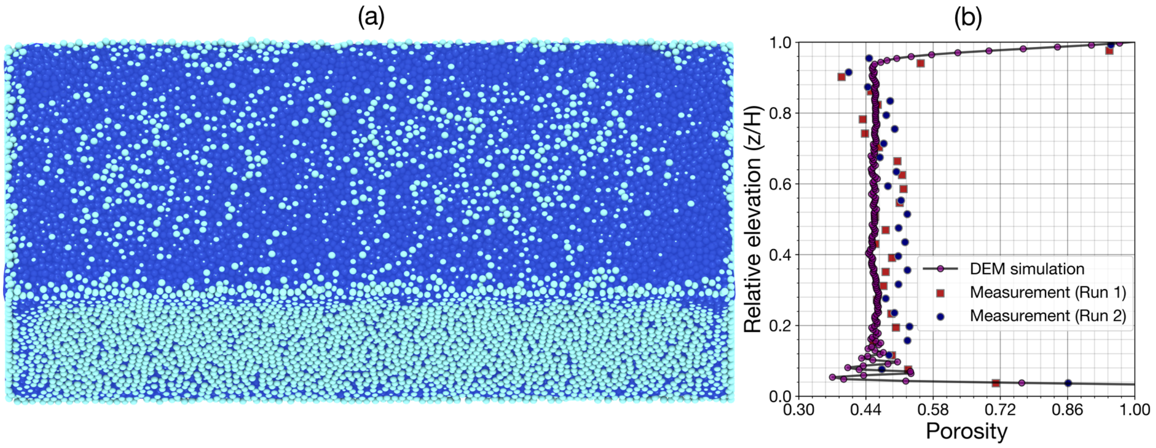

Figure 6.2 Porosity obtained from DEM simulations in comparison with the porosity measurement of Navaratnam, Aberle, and Daxnerová (2018), z is the distance from the flume bottom and H, the total height of the bed.

Table 6.2 Statistical performance of porosity simulation using DEM.

Statistical indicators	**Case-1**	**Case-2**	
		Run 1	Run 2
R	0.9857	0.9575	0.9083
RMSE	0.0165	0.0485	0.0598
MAE	0.0125	0.0361	0.0514

6.2.3 The exchange rate of fine sediment

In order to understand the mechanisms of grain sorting during the infiltration processes of fine sediment into immobile bed, the DEM simulation (Case-3) with uniform fine sediment and gravel are used to investigate the dependence of the exchange rate on size ratio and the fine sediment fraction contained in the bed.

The simulation results for the fine grain size distribution of nine size ratios are shown in Figure 6.3. The DEM simulation is conducted in a square box with dimension of 0.2 x 0.2 m, the depth of the initial gravel thickness is 0.08 m. From Figure 6.3a to Figure 6.3i, size of the coarse grain (D) are constant 0.02 m, while the diameter of fine grain (d) reduces from 0.009 m to 0.002 m to investigate the dependence of fine sediment distribution on the size ratio. The bed porosity is 0.454. The fine sediment is fed uniformly in space and time, and the simulation are stopped when the fine sediment in gravel reach the saturation. The difference in grain size distribution for size ratio 0.45, 0.141, 0.40 (Figure 6.3a, b, c) is not significant. The fine particles accumulate on the surface and cannot infill to gravel. This is consistent with what has been found in Allen (1982) namely how the largest possible sphere (d) which could fit in the largest void in a packing arrangement of spheres (D), was $d/D = 0.52$, when the void fraction is 0.4. The reason that few particles filled in the gravel is that the ratio of fine and coarse grain was smaller and the porosity was larger(0.42) than the ones in Allen research (Allen, 1982).

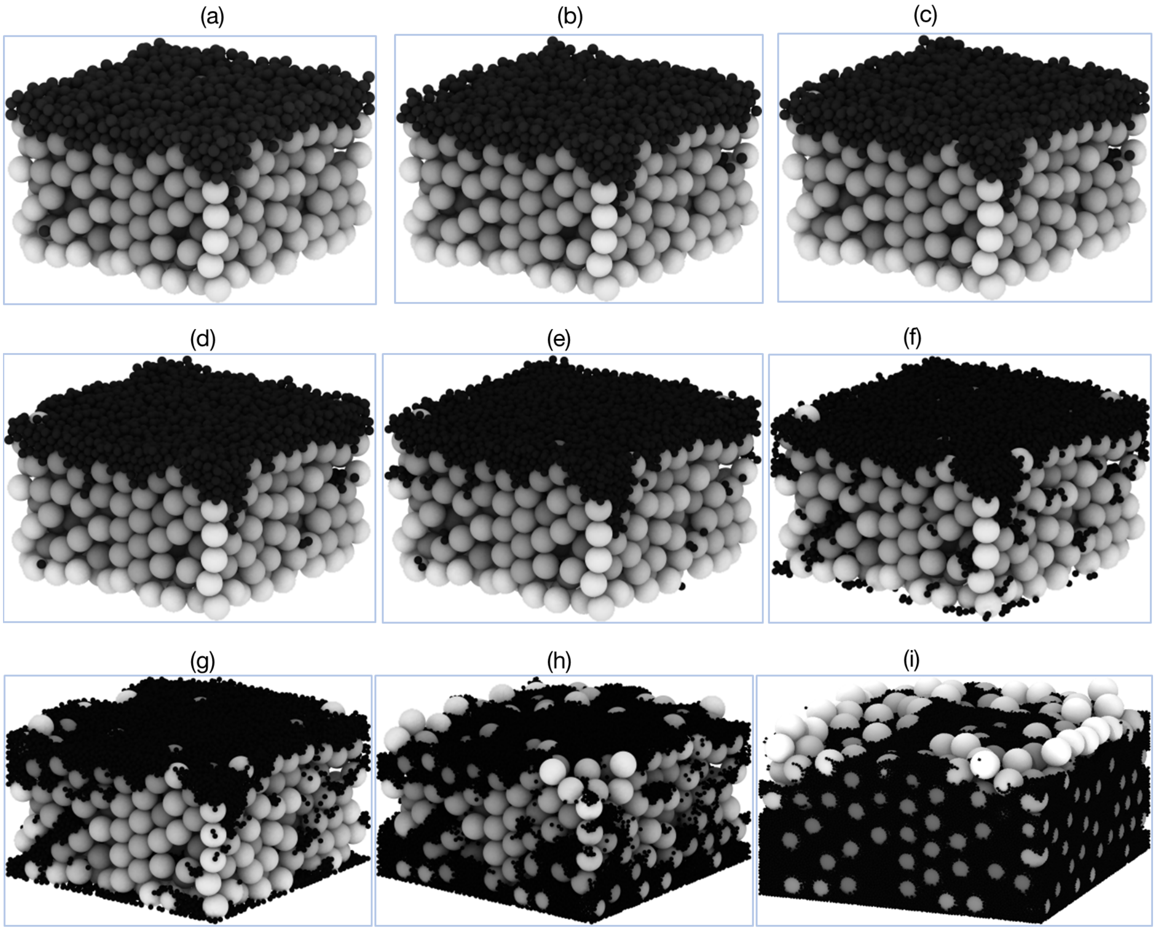

Figure 6.3 Fine sediment distribution dependent on the size ratio (a)-d/D=0.45; (b)- 0.414; (c)-d/D=0.40; (d)-d/D=0.35; (e)-d/D=0.30; (f)-d/D=0.25; (g)-d/D=0.20; (h)-d/D=0.154; (i)-d/D=0.10.

When the ratio is 0.35, 0.30, (Figure 6.3a, b, c) a small amount of the fine grain infiltrates into coarse bed due to fine particle bridging at the surface layer. The size ratios 0.25, 0.20, 0.154 partially impeded percolation. For the ratios of observed percolation and bridging, these simulations are almost directly in line with previous studies (Dudill, Frey, and Church, 2017; Allen, 1982; Sakthivadivel and Einstein, 1970). The cutoff size, which denotes the coarse limit for the grain sizes that can fill in the bed pores, in DEM model was smaller than that of cubical packing (0.414) and larger than that of tetrahedral packing of solid spheres (in the original model of Yu and Standish (1991) which was suggested that the assumption of tetrahedral packing would be reasonable for natural mixtures (McGeary, 1961; Soppe, 1990)). Size ratio (d/D) for 'unimpeded statistic percolation' is smaller than 0.1 (Figure 6.3i) that was found as a small complement for the conclusions in research conducted by Dudill, Frey, and Church (2017).

Figure 6.4 shows the variation of exchange fraction of fine sediment in two layers by time of nine samples with different ratios (d/D). Therefore, the bed is divided into two layers: the thickness of the surface layer is two times of the coarse diameters (D), while the remaining space from the bottom of the surface layer to the bottom of the box is a subsurface layer which is approximately five times of the coarse diameter. At the initial time, the fine grain is fed into the pure gravel. After that, the increasing gradually over the time of the fine fraction contained on the void space of gravel reduced the exchange rate as can be seen in Figure 6.4.

As can be seen in the Figure 6.4a-d, with size ratio 0.45-0.35, the maximum of the exchange rate is at the first time step (one step in visualization is equivalent to 40000 time steps in simulation) and the exchange of fine sediment only occurs in the surface layer (dash line with diamond marker). For size ratios 0.30-0.10 (Figure 6.4e-i), the maximum exchange rate in the surface is in the second time step. The time delay at the first time step is due to the accumulation of fine grain on the top layer, when the flux of the infiltration has not yet formed. The exchange rate in the subsurface layer is not significant in the ratios (d/D) 0.45-0.35 (Figure 6.4a-d), as fine grains clogged the surface layer and can not infill in the lower layer. The increase of the exchange rate in the subsurface layer is rapid for ratios 0.30 to 0.10 with the maximum nearly reaching the feed rate in Figure 6.4i. In general, with size ratios larger than 0.45, the infiltration process only occurred in the surface layer. The effect of the size ratio on the exchange rate is strongly correlated with size ratios larger than 0.4, and not significant when it is smaller than 0.1. With a size ratio smaller than 0.1, the surface layer has almost no effect on the infiltration process. Increasing fine sediment contained in the gravel over time significantly reduces the speed of the infiltration process and stops altogether when the fine fraction of the gravel reaches saturation.

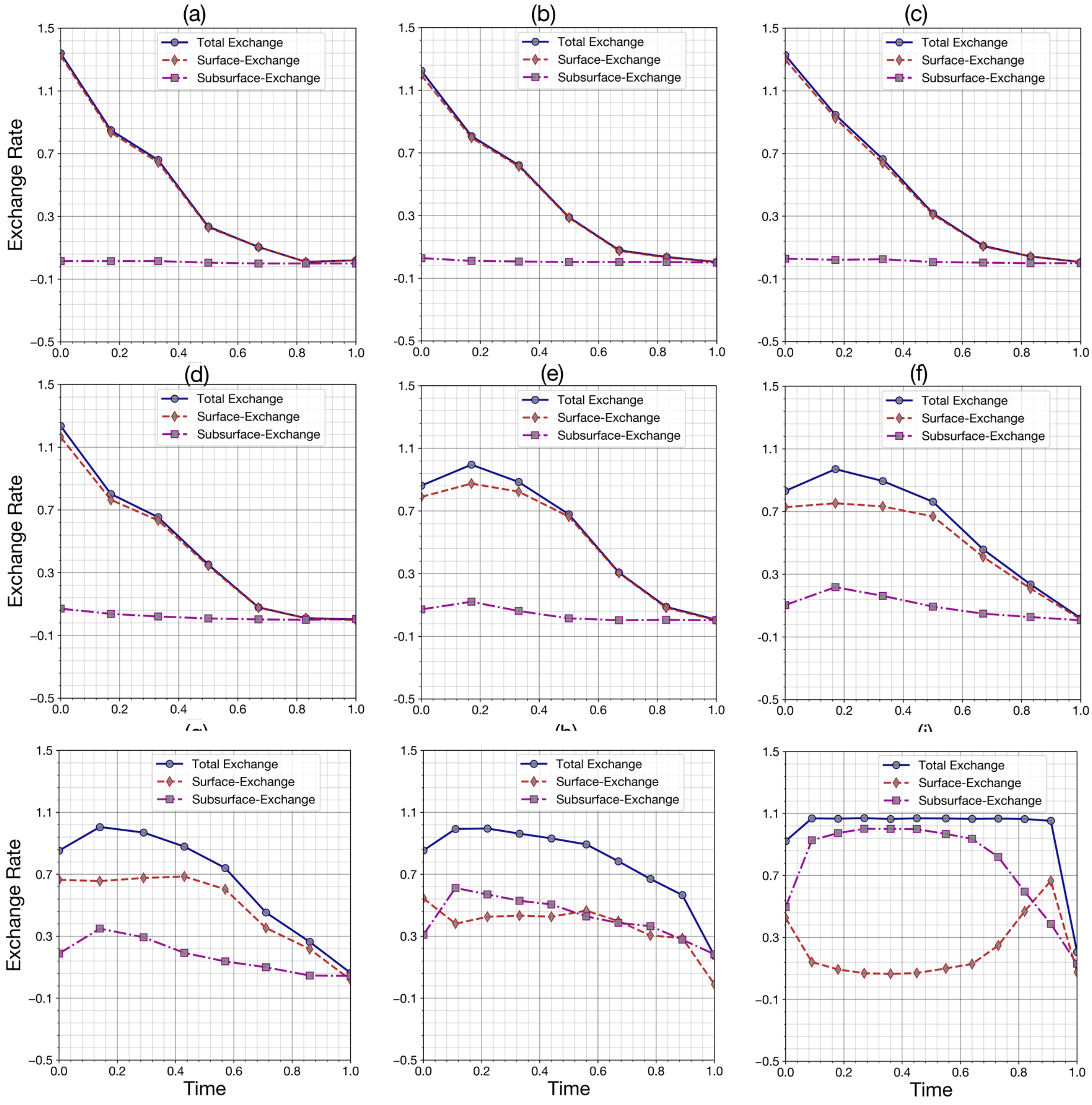

Figure 6.4 The dependent of exchange rate on the size ratio and the time (a)-d/D=0.45; (b)- 0.414; (c)-d/D=0.40; (d)-d/D=0.35; (e)-d/D=0.30; (f)-d/D=0.25; (g)-d/D=0.20; (h)-d/D=0.154; (i)-d/D=0.10.

6.2.4 Simulation infiltration processes to generate data for porosity prediction

Numerical simulations were carried out for Case-4 and Case-5. The model was tested with two small windows with an edge of 0.15 m. In the first 41000 time-steps, 1878 gravel packings were generated and reached a stable state. In the case of bridging, from time-step

41000^{th} to 320000^{th}, the 120000 fine grains sediment were inserted. The time it took for fine sediment to settle was 60000 time-steps. In the case of percolation, from the time-step 41000 to 480000, fine sediment (255976 grains) was fed into the generated gravel-bed. The time it took for fine sediment to settle was 180000 time-steps.

Figure 6.5 presents the structure of the gravel-bed as well as the distribution of fine sediments for the Case-4 and Case-5 at the end of the simulation. Figure 6.5a shows the 3D structure of the gravel-bed and fine sediment distribution in the bridging case. The infiltration process was stopped when the top gravel layer was filled. Figure 6.5c shows the bed materials at the middle cross section at the end of the simulation, where the clogging of fine sediment occurs at the surface. The formed fine sediment layer prevented the upper sediment from filling to the sublayer, where almost all void space remained empty. As can be seen in Figure $6.5c_1$, although the diameters of fine particles are significantly smaller than the void space, they connect to build the ‘bridge’ across gravel called ‘cake filtration’, which depends on the size ratio of gravel and the vertical fine sediment rate (Gibson et al., 2010; Holdich, 2002; Valdes and Santamarina, 2008). Figure 6.5b shows the 3D structure of gravel-bed and fine sediment distribution in the percolation case. The ratio of mean diameter gravel and fine sediment in DEM simulation is in the range of percolation. In this ratio, fine particles are easy to infill to gravel, consistent with what has been found in previous studies (Leonardson, 2010). Figure 6.5d shows the middle x axis cross-section with the most of its void space filled by sediment; however, not all void space was entirely filled. In the bottom of the simulation domain (Figure $6.5d_1$), fine sediment could not move down because of the bottom walls effect, leading to a sudden increase of fine fraction near the flume bed. This phenomenon usually occurred in flume experiments with gravel and fine sediment (Gibson et al., 2009a; Seal et al., 1995; Wooster et al., 2008). Although there are some limitations in the time and scale of the simulations, it can be said that DEM is suitable for simulating the realistic 3D structure of fine sediment and gravel.

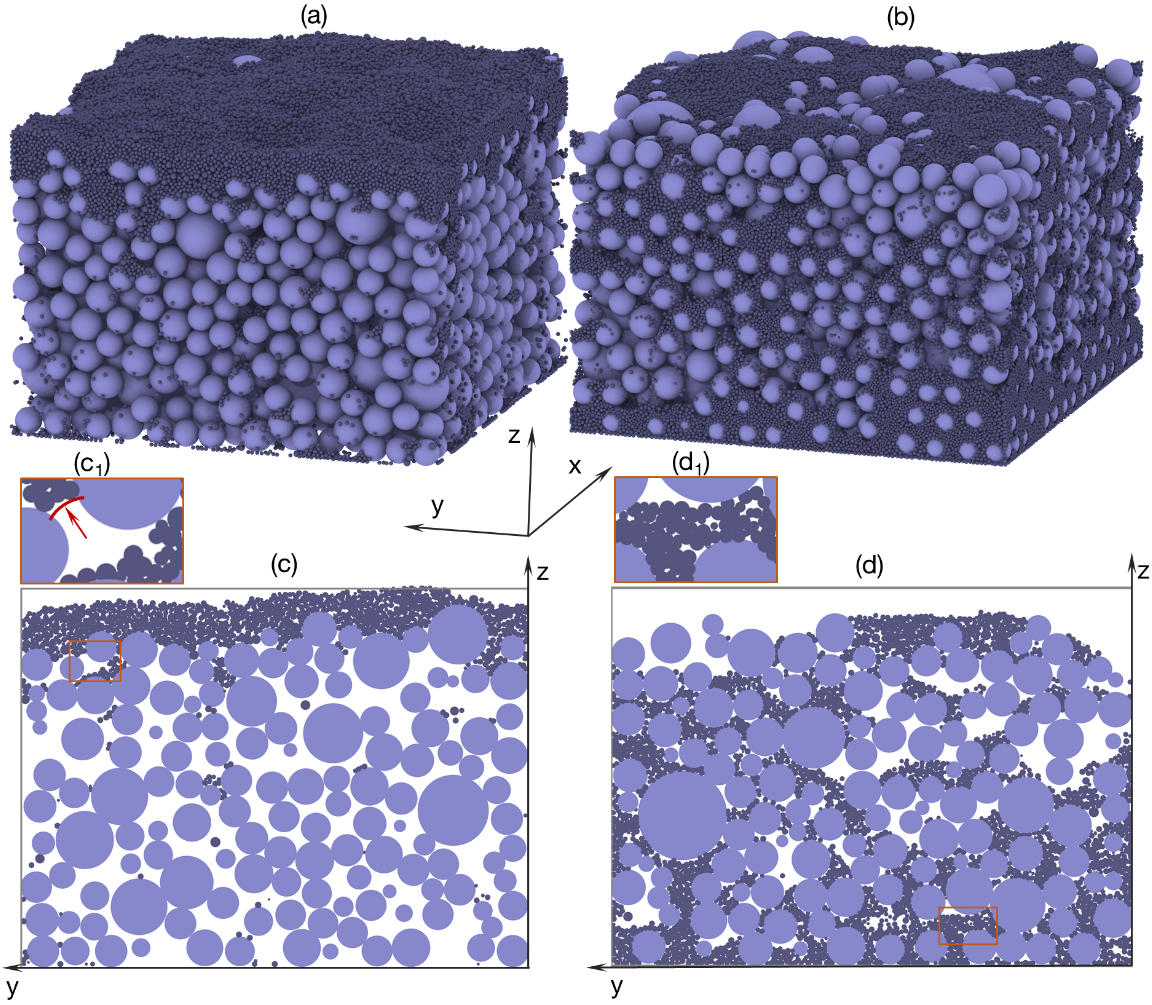

Figure 6.5 Bed structure of filled gravel at final computational time step (a: for bridging and b: for percolation) and of the middle x-axis cross-section (c: for bridging and d: for percolation).

Figure 6.6 shows the comparison between the predicted results of fine sediment distribution and Gibson et al. (2009a) experiments in the bridging and percolation cases. In the top layer-bridging case, fine sediment fraction that reached the highest value (0.6) had values decrease with depth and a final large increase at the bottom. Opposite results found in the percolation case in Figure 6.6b shows that a larger amount of fine sediment was stored in the sublayer (average fine fraction 0.22) and at the surface layer (average fine fraction 0.19). From the bottom, we can observe a wave-form of fine fraction variation due to bottom wall effect and the interactions between particles. The amplitude of the wave is reduced with the elevation because of the influence of the wall effect, resulting in a reduction in chaotically stacked particles in the upper layer. To evaluate the performance of the model, the correlation coefficient (R), root mean square error (RMSE) and mean absolute error (MAE) are used. I reduced the resolution of simulated results from 500 points to 10 points because of the low resolution of the experimental results as well as the collected averaged 7 measurements data at six different flume positions (5.5, 7.8, 9.8, 12.5, 16.5, 18.5 m and 'the still water') (Gibson et al., 2009a). It needs to be emphasized that the experiments and measurements have been conducted in a large flume with no sediment transport, while due to high computational requirements, DEM model only considered a small window (0.15 m wide and 0.5 m long with quiescent water). There are small differences between DEM results and measurement data of Gibson et al. (2009a) due to the rescaling of the experiment. However, we obtained a good agreement between the experimental and numerical results (Table 6.3). The validated results of the DEM method for simulation with fine sediment infiltration into gravel-bed are used to generate data for the FNN model, which is introduced in the next part.

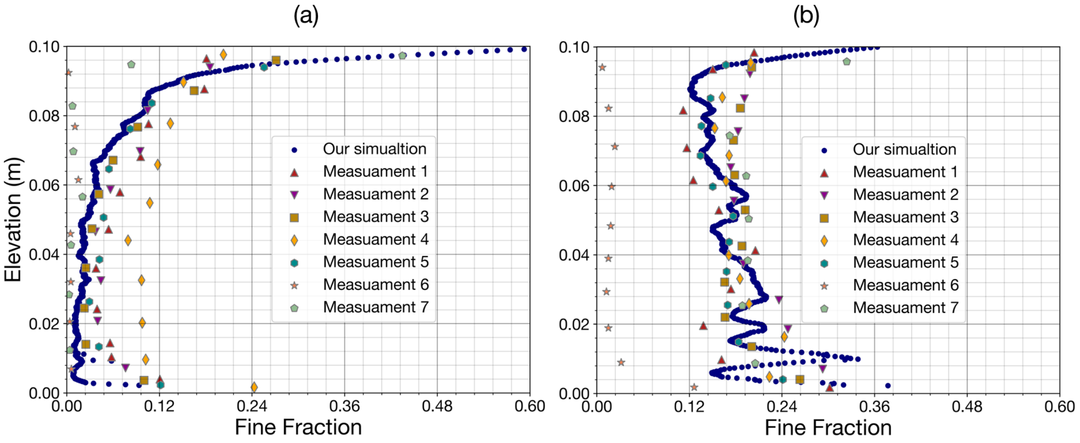

Figure 6.6 Simulated fine sediment distribution in comparison with Gibson's measurement (Gibson et al., 2009a) (a: for bridging and b: percolation).

Table 6.3 Verification of fine sediment distribution with Gibson's measurement (Gibson et al., 2009a).

Statistical indicators	Case-1 (Bridging-1)	Case-2 (Percolation-1)
R	0.969191	0.940474
RMSE	0.128067	0.261443
MAE	0.066765	0.121255

6.2.5 Simulation infiltration processes to generate data for fine fraction prediction

The second and third simulations (Case-6 and Case-7) were conducted for multiple sizes of fine sediment and gravel-bed. The DEM calculated results were compared with the preceding experiment results conducted by Gibson et al. (2011). Algorithms were developed for calculating porosity and grain size distribution in the depth and along the flume to prepare data for data driven methods. Image processing was used to analyze pore distribution which is particularly difficult to determine (Huston and Fox, 2015). Finally, 12 generated datasets, based on the DEM results of Case 6 and 7, were used to train an ANN model (namely Feedforward Neural Network (FNN)) to get the relationship between fine fraction and the controlling factor.

Figure 6.7 shows the 3D results of simulating the infiltration of fine sediment into gravel-bed using spherical particle. Figure 6.7a shows the gravel bed, which generated a random distribution under various forces. These forces are gravity, which is the main cause of sediment settling (which reduces the distance between grains and therefore porosity); buoyancy, which reduces the effect of gravity; and grain friction, which resists the relative motion and may increase porosity. Figure 6.7b shows the sediment and the fine sediment distribution in the gravel (Case-6). For the first 320,000 time steps, 569 grains are fed uniformly onto the surface. Then, 580 grains percolate per time step until the 980,000th time step. Figure 6.7c shows the fine sediment distribution in Case-6, where fine particles clogged the top layer. Figure 6.7d shows another fine sediment distribution. In the bottom of the simulation domain, fine sediment cannot move down due to bottom walls creating a sudden increase of fine fraction near the flume bed. The vertical walls around of the flume support the infiltration process and high concentration of fine grain can be observed in Figure 6.7c, d. This significant increasing of fine fraction in two side of flume always appears in experiments conducted with fine sediment and gravel-bed (Gibson et al., 2009a; Seal et al., 1995; Wooster et al., 2008). As can be seen in the Figures 6.7c, d, the fine sediment distribution result based on DEM is pretty good and realistic.

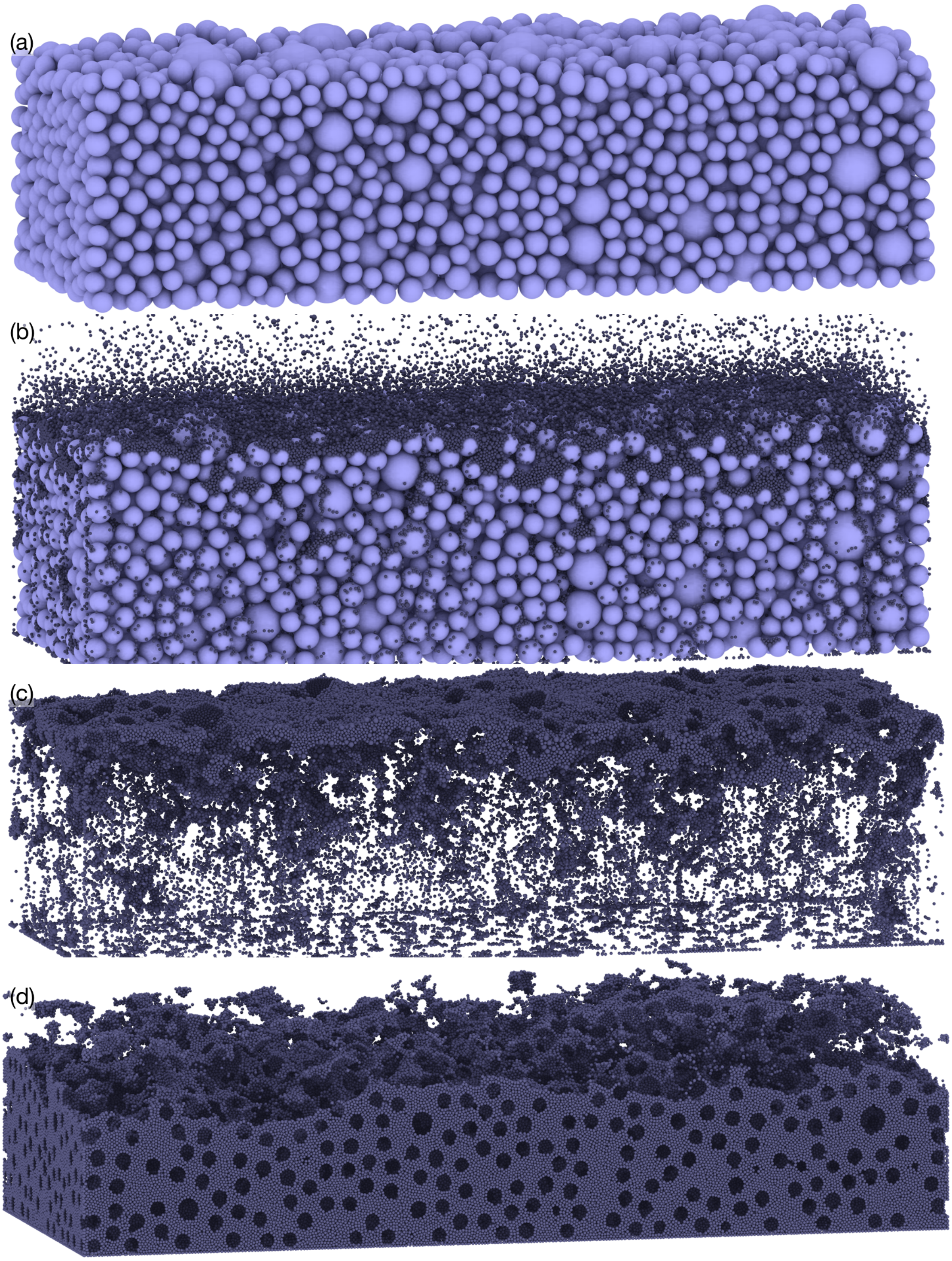

Figure 6.7 Structure of bed: a) gravel-bed structure; b) fine sediment infiltration; c) fine sediment distribution-bridging; d) fine sediment distribution-percolation.

Figure 6.8 shows DEM simulation and experiments conducted by Gibson et al. (2011) in Case-6 and 7. As can be seen in Figure 6.8a, with the fine fraction variation in 5 time steps, the speed of infiltration was reduced with time due to the increasing of the trapped fine sediment in void space of gravel. At the top layer, the fine sediment fraction reached its highest value (0.5) because of the convex and concave shapes of the surface gravel. At the bottom layer, the fine fraction slightly increased due to the accumulation of fine sediment in flume bed. In Figure 6.8b, the porosity varied significantly at the top layer (from elevation 0.08 - 0.1 m) and showed small variation at the bottom layer (from elevation 0.0 - 0.08 m). These values correspond with the fine sediment fraction variation in Figure 6.8a.

Opposite results of fine sediment distribution were found in the Case-7 (Figure 6.8c), where a larger amount of fine sediment was stored at the surface layer (0.19) and in the sublayer (0.22). As a result of a large amount of fine sediment infiltration, porosity varied significantly in both the top layer and the bottom layer. At the bottom layer, porosity changed more drastically than the top layer and reached a minimum value of 0.16 (Figures 6.8d). Fine fraction is stable in the middle of the vertical flume and varies greatly at both ends due to the bottom wall effect and the connection space between layers (6.8c). The amplitude of the fraction wave decreases with elevation because of the bed flume effect, resulting in a reduced chaotic stacking particle in the above bottom layer. The comparison between the simulation results and the experimental measurements (Gibson et al., 2011) are shown in Figure 6.8a,b. The good agreement between DEM simulation and experimental result in Figure 6.8a, and the poor results in Figure 6.8c. The fundamental reason for the lower simulated results of fine fraction in the top layer and the higher results in the bottom layer is the effect of spherical shape on the capacity of the infiltrating process, allowing fine sediment to easily fill the bottom layers without clogging the top. Another reason for the differences between DEM results and measurement data of Gibson et al. (2011) is due to the rescaling of the experiment the experiments and measurements were conducted in a large flume with no sediment transport, while due to high computational requirements, DEM model only considered a small window, 0.15 m wide and 0.5 m long with quiescent water. However, I obtained an acceptable agreement between the experimental and numerical results (Table 6.4). The validated results of the DEM method for simulation with fine sediment infiltration into gravel-bed is used to generate data for the FNN, which is introduced in the next section.

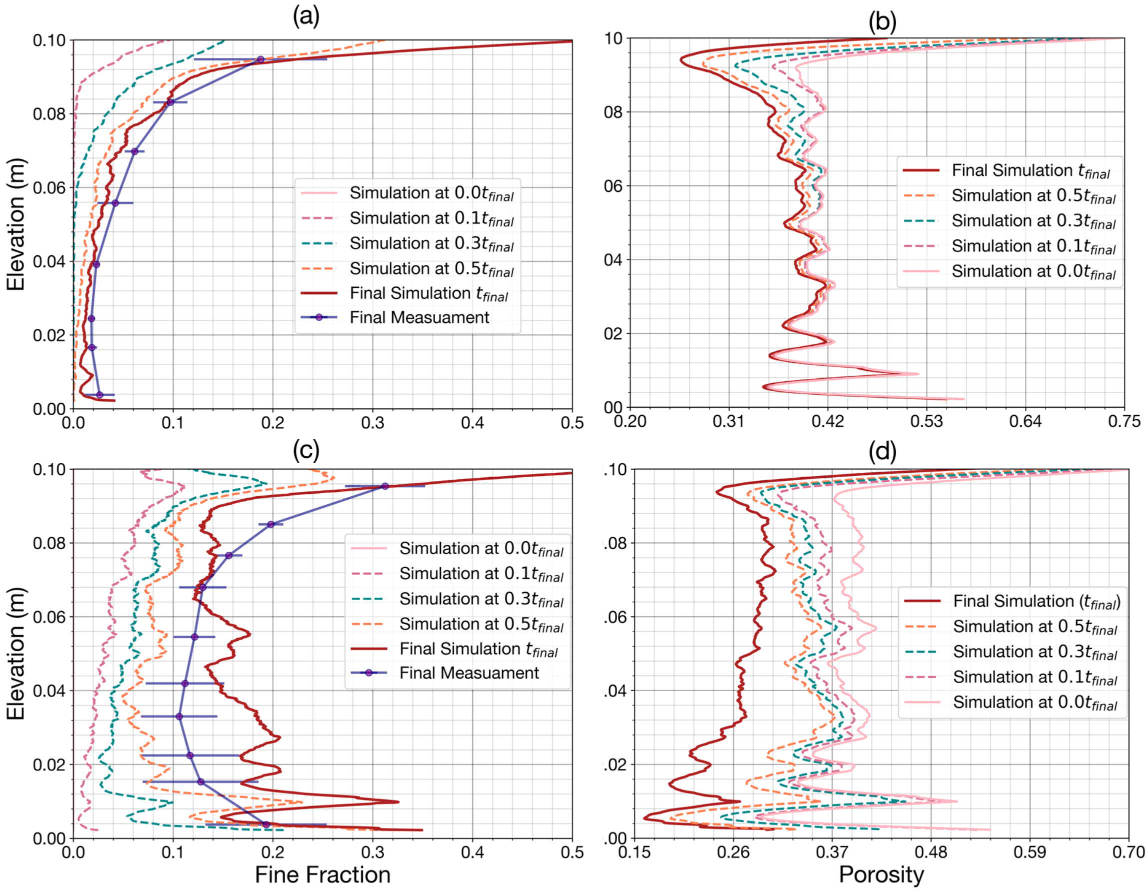

Figure 6.8 Simulated fine sediment distribution in comparison with measurements (Gibson et al., 2011) ((a)- bridging and (d)-percolation) and simulated porosity ((b)- bridging and (d)-percolation).

Table 6.4 Verification of fine sediment distribution in comparison measurements (Gibson et al., 2011).

Statistical indicators	Case-2 (Bridging-2)	Case-3 (Percolation-2)
R	0.941472	0.866244
RMSE	0.049372	0.041221
MAE	0.035878	0.028537

6.2.6 Pore size distribution

Figure 6.9 shows the detection and separation of pores based on the Watershed Segmentation method. Figure 6.9 a, b showed pore detection as the result of a middle surface cross section before and after infiltration. After the infiltration process, the void space area decreases significantly as can be seen in Figure 6.9 a, b. The pore distribution near the side of flume did not change significantly due to the effect of the wall, while the vertical plane of the boundary flume easy to shape a column to transport fine from surface to the bottom.

I chose cross sections at the middle surface layer and subsurface to analyze the change of pore size before and after infiltration process of the flume in Case-6 and Case-7. Four cases were analyzed in Figures 6.9c, d, e, f. The navy color charts represent the frequency of pore distribution before the infiltration process, while the orange color charts represent the frequency of pore distribution after infiltration. The frequency decreased significantly for pore sizes from 1.6 mm to 8 mm and increased sharply for pore sizes smaller than 1 mm. This suggests that the main contributors to the infiltration process are pore sizes larger than seven times the grain diameter (fine grain diameter used this simulation is 0,235, 0.349 mm). The calculated results of the pore diameter shown in Figure 6.9 are based on the equivalent area pore. To compare this result of pore distribution with the previous studies, I converted from area equivalent pore size to largest size that fits into the voids, which is dependent on size ratio and packing profile (loose or dense). Using the transferred ratio calculated in Section 4.2.4 and the transferred ratio (from 1.26 to 1.46), I obtained the range for the minimum pore diameter contribution on the infiltration process (4.79 -5.55). This result is in agreement with previous literature Valdes and Santamarina (2008), who also used perfectly spherical and uniform glass beads as the clogging material in spherical slots, obtained a similar range (4-5) for minimum pore diameter. The 5.5 cutoff value for $d_l : d_f$ was tested in experiments W-3 and W-23 conducted by Wooster et al. (2008), the median pore size to fine geometric diameter of 6.5 in the threshold proposed by Huston and Fox (2015). Conversely, a reinterpretation of the Gibson et al. (2010) threshold value results in a ratio of pore size to fine sediment size as 2.7. The difference in the simulated result and experiment is due to the friction, shape of grain, the methodology to calculate pore. However, in general, the good agreement of the simulated result and measurement demonstrated that Watershed Segmentation is an effective method in analyzing the DEM results to obtain the pore size distribution, which is useful for analyzing the infiltration process.

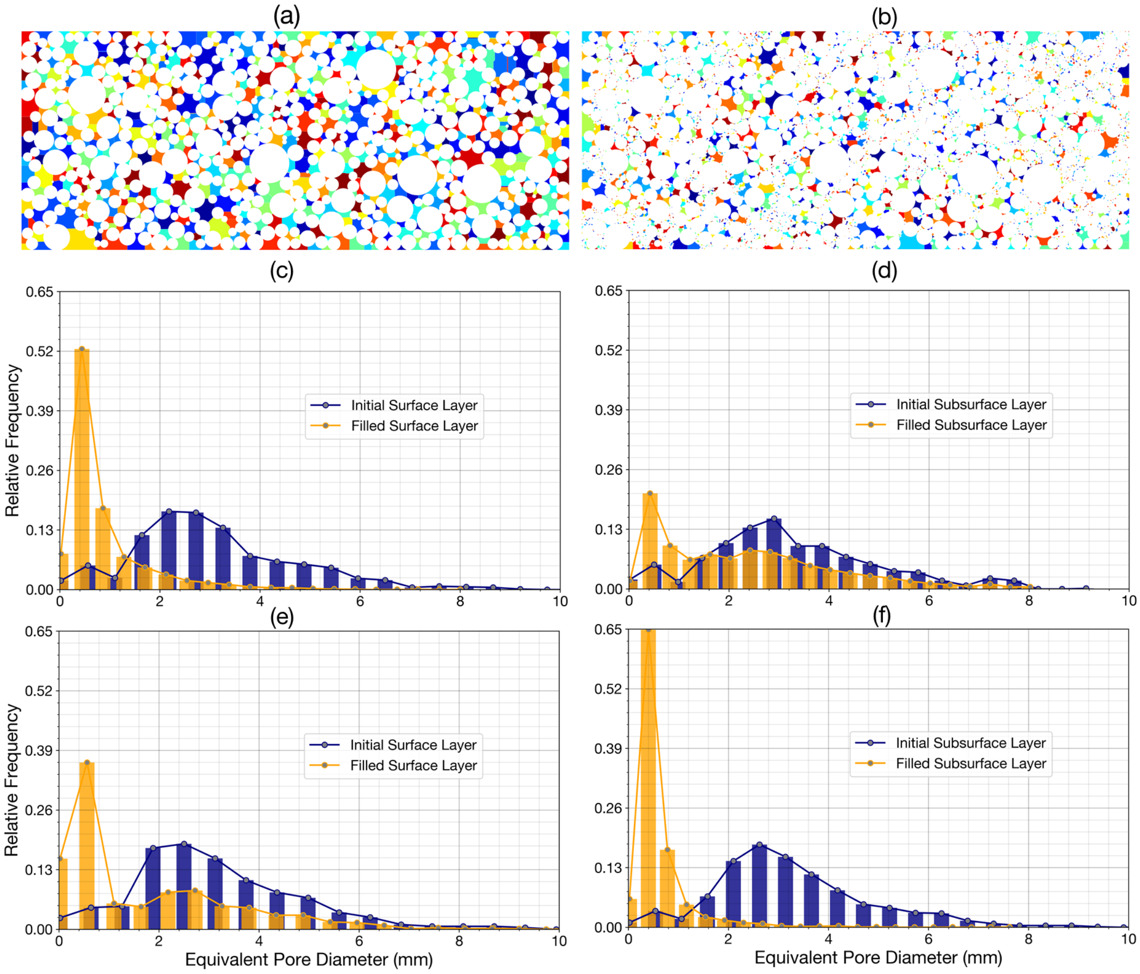

Figure 6.9 Pore distribution at middle of layer: a) surface - initial gravel; b) surface-bridging; c) Frequency - surface - bridging; d) Frequency -subsurface - bridging; e) Frequency - surface - percolation; f) Frequency - subsurface-percolation.

6.3 FNN prediction based on DEM data

6.3.1 Porosity prediction

6.3.1.1 Input data for FNN

As mentioned above, I used the results obtained by the DEM for Case-4 and Case-5 to develop FNN models. Furthermore, based on DEM grain mixtures I create two groups of data (Data-classification-1 and Data-classification-2) as follows:

Data-classification-1: The mixture is characterized by 9 grain-sizes, inputs parameters included: location of sample (l), and 9 fractions: $f_1\ (d_1 < 0.125\,mm),\ f_2\ (0.125 \leq d_2 < 0.25),\ f_3\ (0.25 \leq d_3 < 0.5),\ f_4\ (0.5 \leq d_4 < 1),\ f_5\ (1 \leq d_5 < 2),\ f_6\ (2 \leq d_6 < 4),\ f_7\ (4 \leq d_7 < 8),\ f_8\ (8 \leq d_8 < 16),\ and\ f_9\ (16\,mm \leq d_9)$.

Data-classification-2: The mixture is characterized by two grain-sizes. Inputs parameters included location of sample (l), fraction of the fine grain (with d< 2 mm), and fraction of the coarse grain (with $D \geq 2mm$).

Based on the DEM results, grain size distribution and porosity data were generated for 500 different cross sections along the depth (z-direction) and for 800 different cross sections along the flume (x-direction). I created in total 8 datasets: the 1^{st} dataset using Data-classification-1 for bridging case and in z-direction (called Dataset-1), the 2^{nd} dataset using Data-classification-2 for bridging case and in z-direction (called Dataset-2), the 3^{rd} dataset using Data-classification-1 for percolation case and in z-direction (called Dataset-3), the 4^{th} dataset using Data-classification-2 for percolation case and in z-direction (called Dataset-4),the 5^{th} dataset using Data-classification-1 for bridging case and in x-direction (called Dataset-5), the 6^{th} dataset using Data-classification-2 for bridging case and in x-direction (called Dataset-6), the 7^{th} dataset using Data-classification-1 for percolation case and in x-direction (called Dataset-7), and the 8^{th} dataset using Data-classification-2 for percolation case and in x-direction (called Dataset-8). These datasets contain also cross section locations.

Each dataset in the x-direction is randomly divided into two subsets of data, namely 80% (400 data) for training and 20% (100 data) for testing purposes. Similarly, I randomly split 800 samples in the x-direction of each dataset into two subsets: 80% (640 data) for training and 20% (160 data) testing purposes. Figure 6.10 shows exemplarily the cumulative distribution at 10 different cross sections and grain distribution at cross-section 480^{th} in the z-direction.

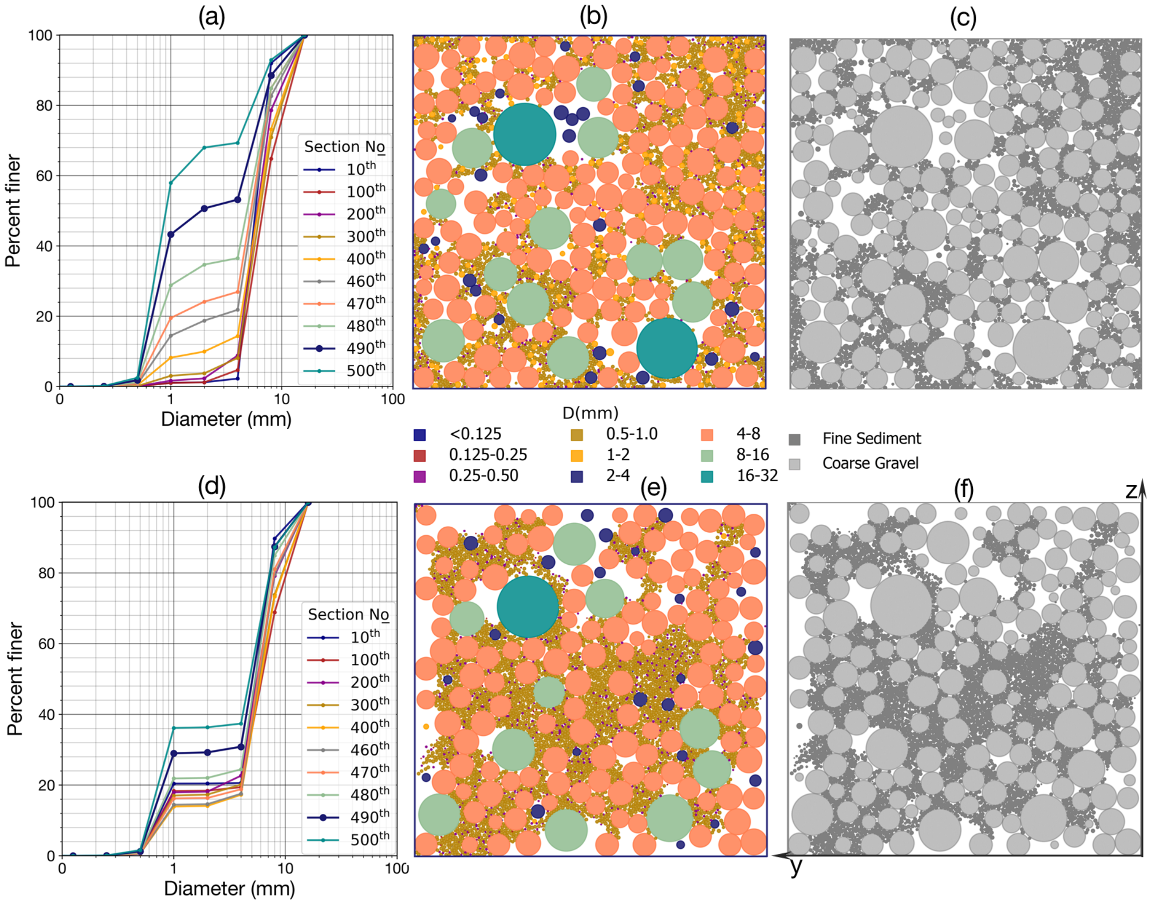

Figure 6.10 The cumulative grain-size distributions of bed materials at ten different represented cross- sections in z-direction (a-for bridging; d-for percolation) and bed structures at cross section 480^{th} in z-direction (b-for Dataset-1; c-for Dataset-2; e-for Dataset-3; d-for Dataset-4).

6.3.1.2 Porosity prediction based on FNN model

Porosity depends on pressure and grain size distribution. In DEM model, effects of pressure on porosity, the consequence of forces acting on the grain matrix including gravity, buoyancy, grain friction and contact force, were considered. The influence of these factors contributed to the final location of grain obtained from DEM simulations. Grain diameter and fraction of each size class are used to represent the characteristic of the grain size distribution.

To create the FNN architecture one must first determine the number of layers of each type and the number of nodes in each of these layers. In an FNN one or more hidden layers of sigmoid neurons are often found, subsequently followed by an output layer containing linear neurons or nodes. By having multiple layers of neurons with nonlinear activation functions, it allows the network to learn nonlinear relationships that exist between input and output vectors (Bui et al., 2015). There is debate surrounding if the performance of FNN improves from the addition of more hidden layers. It has been found the instances where performance improves with a second (or third, etc.) hidden layer are very few. Thus, one hidden layer is claimed as adequate for most problems FNN aims to solve. Let it be known that the number of neurons in the input layer is equal to the number of input features in the data set. The output layer contains only a single node, namely the bed porosity. The optimal size of the hidden layer is normally in the range of the size of the input and output layers (Heaton, 2008). In this study, an FNN with three layers is created with number neural nodes in the input layer of 10, the hidden layer of 8 and the output layers of 1.

The statistical indices (R, RMSE, MAE) of FNN model performance for four porosity predictions in z-direction (Datasets 1, 2, 3, and 4) are presented in Table 6.5. In the bridging case, the prediction based on Data-classification-2 (Dataset-2) performed significantly better than Data-classification-1 (Dataset-1). Similarly, in the percolation case, the prediction using Dataset-4 is slightly better than Dataset-3. The prediction for percolation case achieved a higher quality of result than bridging case. It can be explained that in the bridging case, the fine fraction stored in the void space of gravel-bed is smaller than in the percolation case. That lead to the prediction model being able to easily capture the effect fine sediment has on porosity output results. Furthermore, in the percolation case, the distinction between the coarse and fine groups is clear because of the large ratio of the coarse gravel to the fine sediment. As a result, the errors in the predicted results also reached minimum values (RMSE = 0.005753, MAE = 0.003155) from the model using Data-classification-2 of percolation (Dataset-4).

Table 6.5 Statistical performances of FNN model for predicting porosity along the depth (z-direction).

Statistical indicators	Case-1 (z-direction)		Case-2 (z-direction)	
	Dataset-1	Dataset-2	Dataset-3	Dataset-4
R	0.965968	0.989206	0.990841	0.994024
RMSE	0.015736	0.008786	0.007807	0.005753
MAE	0.009580	0.006548	0.004898	0.003155

Figure 6.11 shows the comparison between the FNN based porosity and the data obtained from DEM. In Figure 11a, d the predicted porosity variation along the depth is compared with porosity based on Dataset-1 and Dataset-2. The dark magenta dotted line represents

the DEM based data, where the minimum porosity reaches the value of 0.24 at the surface layer and increases with depth to reach a maximum value 0.6 near the bottom. Near the box bottom, porosity fluctuated widely. Gravel packing created two clear connection areas: a coarse gravel layer with the bottom box and with the upper layer that suddenly increased void spaces seen at z = 0.00 m and z = 0.012 m in Figure 6.11a, d. This also confirms the problem with laboratory porosity experiments, specifically how the disturbance of packing near the wall of the container causes pores size near the walls to be consistently larger than near the center of the container (also discussed in Ridgway and Tarbuck (1968)).

Figures 6.11b, c, e, f show the performance of the FNN model and the scatter of porosity for the test dataset. As can be seen in Figure 6.11b, the FNN prediction using Dataset-1 in bridging case overestimated significantly the high peak (0.58,0.01), (0.47,0.018), (0.43,0.044) in comparison with the DEM based data. A light overestimation also occurs with the FNN prediction based on Dataset-3 in percolation case (Figure 6.11d, e). A point worth noting is that both of Dataset-1 and Dataset-3 used Data-classification-1 with nine sizes of grains. While the performance of the FNN model is very good for Dataset-2, Dataset-4 is based on Data-classification-2 with two sizes of grains (Figure 6.11c, f). Overall, as can be seen in Figure 6.11, FNN models provide good results for porosity prediction. This suggests that the data-driven method based on the grain size distribution is suitable for porosity prediction along with the depth in a gravel-bed.

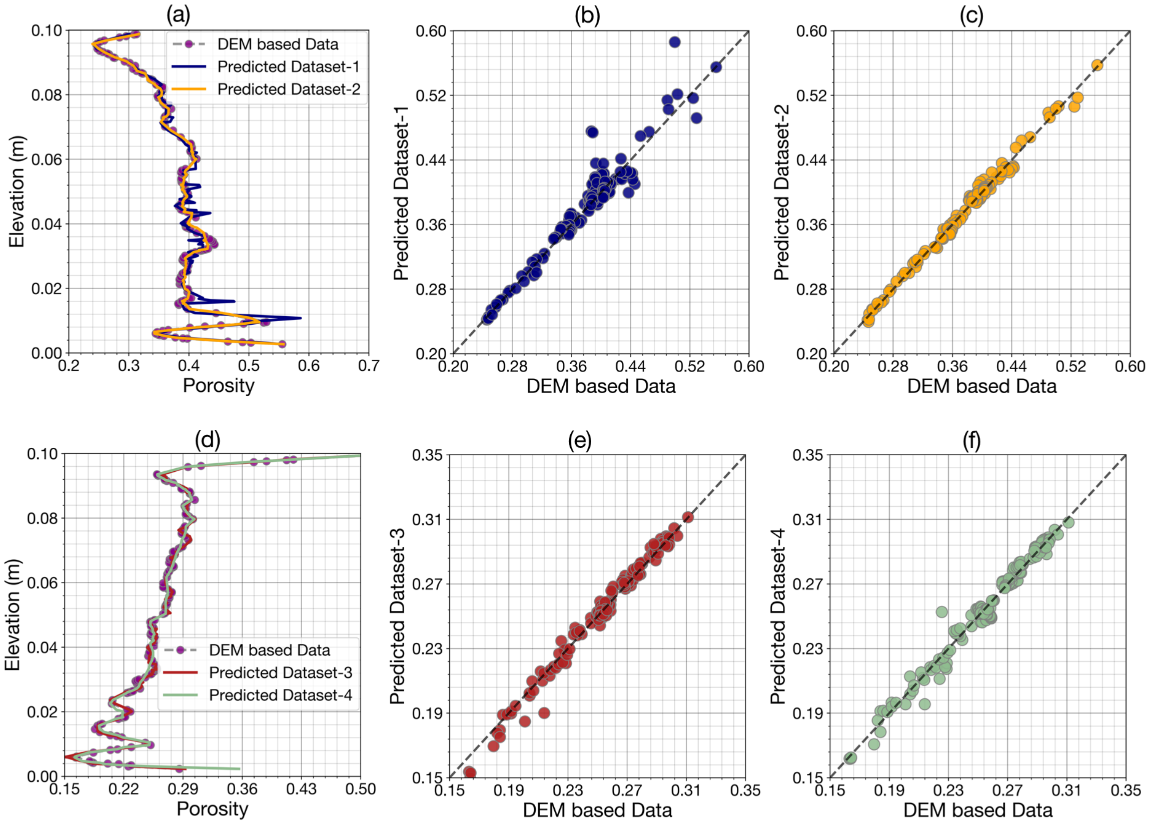

Figure 6.11 FNN predicted porosity along the depth (z-direction) (a-for Datasets 1 and 2; d-for Datasets 3 and 4) and scatter plot (b-for Dataset-1; c-for Dataset-2; e-for Dataset-3; f-for Dataset-4).

Figure 6.12 shows the performance of FNN models using four datasets along the horizontal x-direction for bridging and percolation cases in comparison with the DEM based data. The dark magenta dot-dash lines show the DEM based porosity along the horizontal direction. The porosity values changed from 0.37 to 0.51 in bridging case – upper panel (Figure 6.12a) and from 0.22 to 0.40 for percolation – lower panel (Figure 6.12b). The average oscillation amplitude of porosity for these four cases (0.18) near the sidewall varies significantly more than the inside domain (0.060). This can be partly explained because when the distance is equal to one medium radius (0.007 m) from the wall, the center of coarse particles stacked along a vertical plane parallel to the wall, where the highest density of the material is reached and reduces with distance from the center of the grain. The effect of the sidewall on the increasing porosity was also discussed in previous experimental studies (Navaratnam, Aberle, and Daxnerová, 2018; Ridgway and Tarbuck, 1968; Sulaiman, Tsutsumi, and Fujita, 2007b).

In Figure 6.12a, b the FNN prediction based on four Datasets (5, 6, 7, and 8) gave poor results at profiles, x=0.010 and 0.140 and some other profiles. The model did not agree with the curve of DEM based porosity distribution (e.g. x=0.095-0.135 m). The model tends to overfit a few points with sudden increases and decreases of fine sediment due to the two sidewalls. Inversely, inside the flume when the porosity did not fluctuate significantly, the model was found to underfit. However, in general, the performances of models are in good agreement with the DEM based data. Table 6.6 shows relatively good results of porosity prediction and in the x-direction, FNNs using Dataset-6 and Dataset-8 perform better than using Dataset-5 and Dataset-7 respectively.

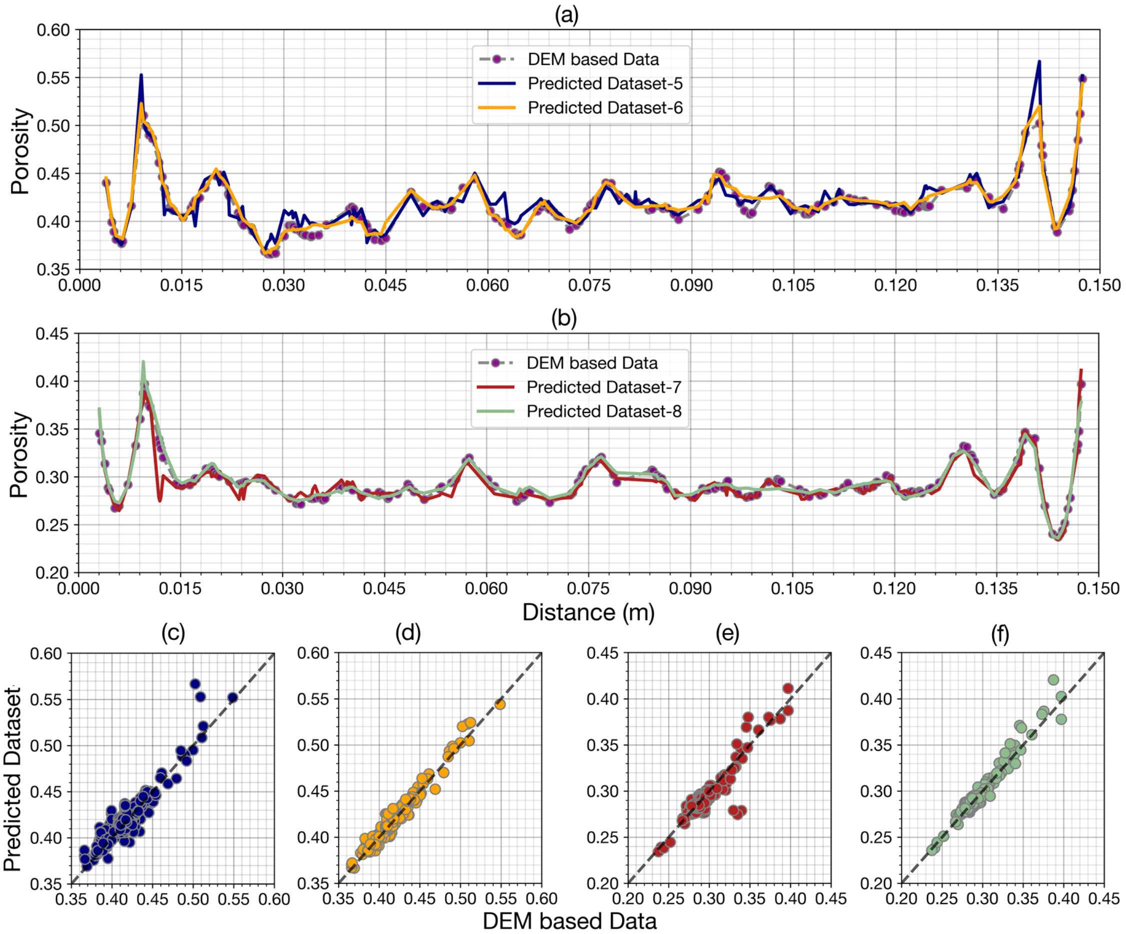

Figure 6.12 FNN predicted porosity along x-direction (a-for Datasets 5 and 6; b-for Datasets 7 and 8) and Scatter plot (c-for Dataset-5; d-for Dataset-6; e-for Dataset-7, f-for Dataset-8).

Table 6.6 Statistical performances of the FNN model for predicting porosity along the flume (x-direction).

Statistical indicators	Case-1 (x-direction)		Case-2 (x-direction)	
	Dataset-5	Dataset-6	Dataset-7	Dataset-8
R	0.9298	0.9786	0.9236	0.9748
RMSE	0.0113	0.0063	0.0097	0.0060
MAE	0.0080	0.0050	0.0056	0.0041

Eight datasets were used to train the FNN networks. Regarding the influence of the grain classifications on the efficiency of FNN models, I observed slight differences between Data-classification-1 and Data-classification-2. As can be seen in Tables 6.5 and 6.6, the statistical parameters of datasets based on Data-classification-2 are better than datasets based on Data-classification-1. Interestingly, with more detailed classification the porosity prediction is not as good as in the less detailed classification. This suggests that with the large size ratio of the coarse gravel to the fine sediment (D/d greater than 6.4), the detailed classification contained the little information groups (usually the coarse groups with the diameter larger than 2 mm) that may cause some inaccuracies in predicting porosity. This is consistent with the former study conducted by Bui, Bui, and Rutschmann (2019) in that the variation of porosity of gravel-bed is mainly caused by the variation in fine sediment rather than the effect of the rearrangement of the coarse gravel. The redundancy of useless information decreased the capability of FNN.

6.3.2 The prediction of the fine sediment fraction

6.3.2.1 Input data

The results obtained by the DEM for Case-6 and Case-7 are used to develop FNN models. Input parameters to predict the fine sediment fraction (fine fraction) along the depth (z-direction) included the location of the sample (l), the size ratio of fine to coarse grain and porosity of the layer. 500 samples of each dataset were generated from 500 different cross sections along with the depth (z-direction). In this part, the fine sediment fractions at the half time and the final time of the infiltration process for Case-6 and Case-7 are predicted. Thus, the total 4 datasets of the z-direction are created: the 1^{st} dataset for Case-6 at half-time simulation (called Dataset-1), the 2^{nd} dataset for Case-6 at final-time simulation (called Dataset-2), the 3^{rd} dataset for Case-7 at half-time simulation (called Dataset-3), the 4^{th}

dataset for Case-7 at final-time simulation (called Dataset-4).

In the x-direction, the fine sediment fraction in surface layer and subsurface layer at the half time and the final time of the infiltration process are predicted. Thus, total 8 datasets of the x-direction are created are created (each dataset contained 1500 samples). For the x direction: the 5^{th} dataset for surface layer of Case-6 at half-time simulation (called Dataset-5), the 6^{th} dataset for subsurface layer of Case-6 at half-time simulation (called Dataset-6), the 7^{th} dataset for surface layer of Case-6 at final-time simulation (called Dataset-7), the 8^{th} dataset for subsurface layer of Case-6 at final-time simulation (called Dataset-8), the 9^{th} dataset for surface layer of Case-7 at half-time simulation (called Dataset-9), the 10^{th} dataset for subsurface layer of Case-7 at half-time simulation (called Dataset-10), the 11^{th} dataset for surface layer of Case-7 at final-time simulation (called Dataset-11), the 12^{th} dataset for subsurface layer of Case-7 at final-time simulation (called Dataset-12).

Each dataset in the z-direction (500 samples) is randomly divided into two subsets of data, namely 80% (400 data) for training and 20% (100 samples) for testing purposes. Similarly, 1500 samples in the x-direction of each dataset is randomly divided into two subsets: 80% (1200 samples) for training and 20% (300 samples) for testing purposes.

6.3.2.2 The prediction of the fine sediment fraction based on FNN model

Figure 6.13 shows the performance of the FNN model and the scatter of the fine sediment fraction (fine fraction) for the test dataset. As can be seen in Figure 6.13a, the FNN in Case-6 gave very good result in predicting the fine fraction variation with depth at half time of simulation (Dataset-1) and final time simulation (Dataset-2). In Case-7, the performance of the FNN model is good for Dataset-3, and not good for Dataset-4 (Figure 6.13b). Overall, as can be seen in Table 6.7, FNN models provide good results for the fine fraction prediction. This suggests that the data-driven method based on porosity and ratio is suitable for the fine fraction prediction along the depth in a gravel-bed.

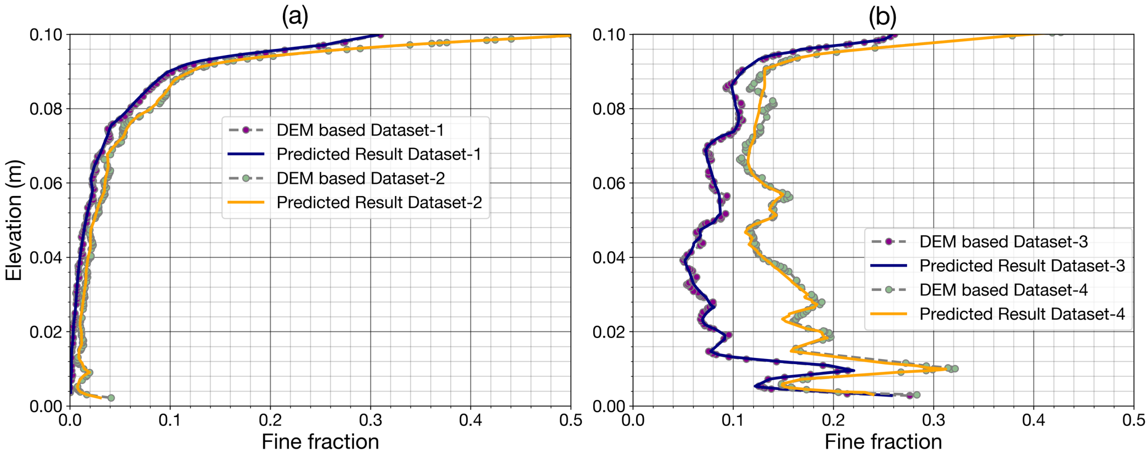

Figure 6.13 FNN predicted the fine fraction along the depth (z-direction) (a-for Datasets 1 and 2; b-for Datasets 3 and 4).

Table 6.7 Statistical performances of FNN model for predicting the fine fraction along the depth (z-direction).

Dataset	1	2	3	4
R	0.9996	0.9998	0.9970	0.9957
RMSE	0.0026	0.0021	0.0041	0.0075
MAE	0.0016	0.0016	0.0033	0.0053

Figure 6.14 shows the comparison between the FNN based the fine sediment fraction and the data obtained from DEM. In Figure 6.14 the predicted fine fraction variation along the x-direction is compared with the fine fraction based on Datasets 5 to 12. In Case-6 (Figure 6.14a, b), the blue dot-dash line represents the DEM based data of the fine fraction in the surface layer, which has an averageda value of around 0.2 at half time simulation and around 0.3 at end simulation while at the subsurface layer, the fine sediment was small with little fluctuation (0.01 at half time and 0.04 at the end of simulation). In Case-7 (Figure 6.14c, d), the fine fraction in the subsurface (magenta dot-dash line) is significantly higher than in the surface layer (blue dot-dash line). The average values of the fine fraction contained in the subsurface layer are around 0.1 at half time of simulation and 0.18 at the end time of simulation while at the surface layer, the values are 0.06 and 0.07 respectively. The amplitude of fluctuation of the fine fraction in the surface is larger than in the subsurface (Figure 6.14). The reason for this phenomenon is the convex and concave surface layer. As a result of the movement from high elevation to the low elevation, low concentration of the fine sediment

was accumulated at convex zones and high concentration of the fine sediment at the concave zones. The thin surface layer also increases the amplitude of the fine fraction. The values of the fine fraction for the subsurface of percolation near the sidewall (magenta dot-dash line (Figure 6.14 c, d)) are significantly higher than inside a domain. The effect of the sidewall on the increasing the fine fraction was also discussed in previous experimental study (Gibson et al., 2010; Wooster et al., 2008).

Figure 6.14a, b, c, d show the performance of the FNN model of the fine sediment fraction prediction for the test dataset. The FNN prediction underestimated significantly the high peak (distance 0.21 - 0.38 dataset-5 Figure 6.14a), (distance 0.32 - 0.36 dataset-7 Figure 6.14 b), in comparison with the DEM based data. In some ranges, FNN did not catch the rule of distribution (distance 0.27 - 0.39 m dataset-10 Figure 6.14c, distance 0.26 - 0.36 m dataset-12 Figure 6.14d). The fundamental reason for the tolerances is the quality of the input data. The average porosity, the input parameters of the FNN model, can be high at the top of the cross section and low at the bottom, the average porosity used may not contain enough information for the fine fraction prediction. Furthermore, the DEM data may be disturbed by the bottom and side wall effect that reduced the accuracy of the FNN model. However, in general, the performances of models are in good agreement with the DEM based data. Table 6.8 shows relatively good results of the fine fraction prediction and in the x-direction.

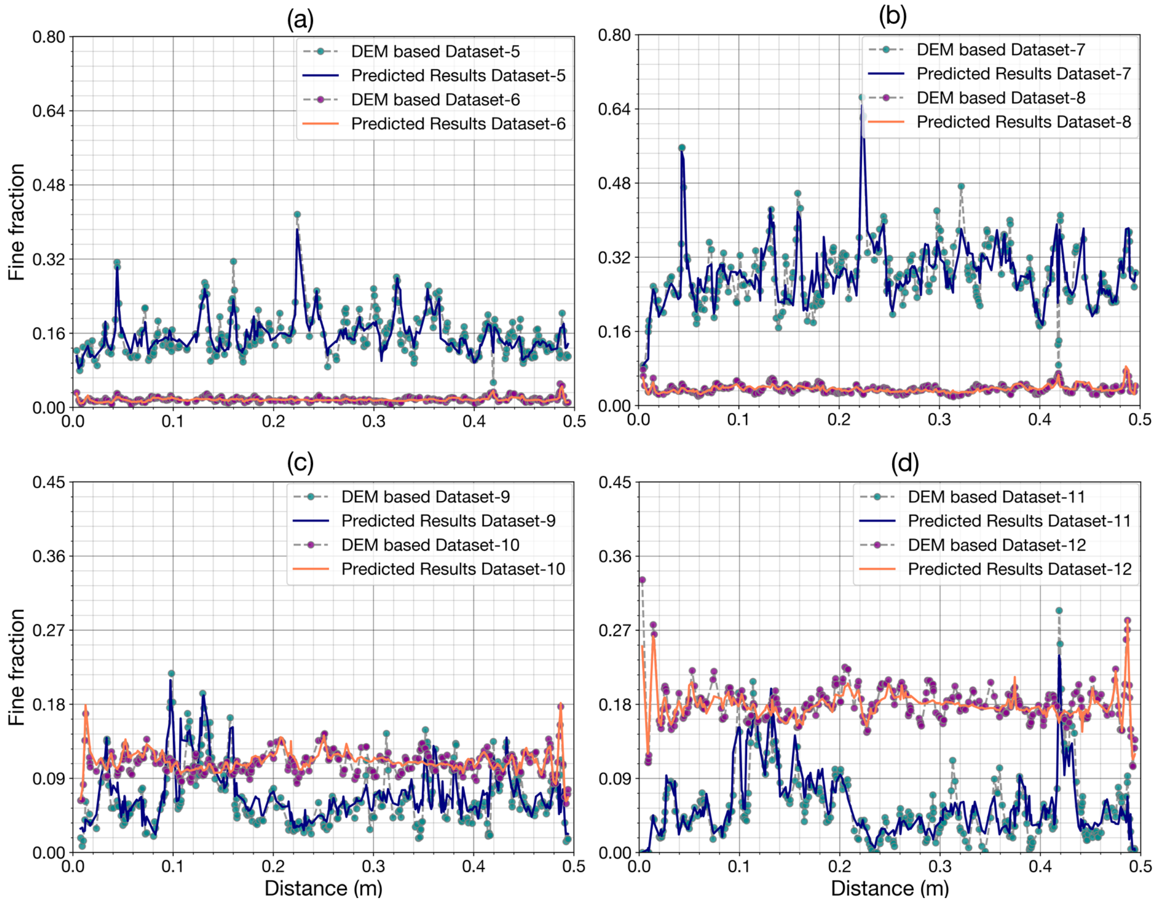

Figure 6.14 FNN predicted the fine fraction along the flume (x-direction) (a-for Datasets 5 and 6; b-for Datasets 7 and 8; c-for Datasets 9 and 10; d-for Datasets 11 and 12).

Table 6.8 Statistical performances of FNN model for predicting the fine fraction along the flume (x-direction).

Dataset	5	6	7	8	9	10	11	12
R	0.846	0.768	0.868	0.731	0.858	0.865	0.840	0.813
RMSE	0.025	0.004	0.037	0.006	0.022	0.013	0.021	0.009
MAE	0.019	0.003	0.028	0.005	0.016	0.010	0.015	0.007

6.3.3 Computation time

Eight and twelve datasets were used to train network to predict porosity and the fine fraction respectively. The time for each training a dataset is approximately 1,5 hours for 10000 iterations. The time to obtain the tested results from the predicted model is approximation

0.5 seconds. The required time for calculating porosity and the fine fraction using DEM is from few hours to few hundred hours (up to 198 hours in Case 7-Table 6.9). Although the time required for training ANN was also significantly long, the model was trained only once for each dataset. After the training process, I obtained an explicit relationship between porosity, the fine fraction and the inputs, which can be then used to calculate the porosity, the fine fraction with other datasets of inputs. Thus, the time needed to calculate the porosity and the fine fraction is reduced significantly by employing an FNN method in comparison with using solely DEM. It is needed to emphasize that a data-driven method can entirely replace the DEM in calculating the porosity and the fine fraction. Of cause, this replacement is strictly applied for the same variable range of the grain size distribution. Nonetheless, the reduced simulation time does not only save computer resources but also makes the connection between FNN and conventional hydro-morphodynamics model more robust.

Table 6.9 Computation time each process for two cases of infiltration process (in hour).

	Process	Pair time	Neigh time	Comm time	Outpt time	Other time
Case-4	Insert	4.058	4.519	0.005	0.002	0.720
	Settle	2.311	0.659	0.002	0.001	0.288
Case-5	Insert	6.932	12.020	0.012	0.002	1.469
	Settle	3.920	3.411	0.003	0.001	0.579
Case-6	Insert	4.439	4.860	0.009	0.003	1.013
	Settle	3.003	0.744	0.003	0.002	0.471
Case-7	Insert	58.415	110.914	0.081	0.015	10.285
	Settle	8.697	8.728	0.006	0.003	1.165

Pair time: Time to find contact overlaps, forces; Neigh time: Time to form verlet lists, sorting them and finding the neighbors; Comm time: Message Passing Interface (MPI) communication time; Outpt time: Dump and thermo commands; Other time: Other fixes.

6.4 Bed variation considering porosity change

6.4.1 Bed form movement and porosity variation of sand wave

The simulation was conducted in a 500 m long straight channel with a rectangular cross section, a uniform specific water discharge of 23 $m^3/s/m$, a constant water elevation of 10 m long the channel, and the initial bed level defined, as follows:

$$z_b\left(x,0\right)=\begin{cases}\sin^2\left[\frac{\pi(x-200)}{100}\right] & 200\leq x\leq 300\\ 0 \quad otherwise\end{cases} \tag{6.1}$$

The bed mixture was sorted into two fractions (d_1 = 7 mm; d_2 = 1 mm), which was then used to compose a desired size gradation. The initial size fractions are ($\beta_{a,1}$ = 0.75 and $\beta_{a,2}$ = 0.25) in the active layer and ($\beta_{s,1}$ = 0.65 and $\beta_{s,2}$ = 0.35) in the stratum layer.

Figure 6.15 presents the change in bed characteristics over time. Figure 6.15a shows the bed elevation at different time steps, the dune moved forward with the water flow and reduced its height. Especially, in the front of the dune, the gradient of sediment discharge is positive due to the increase in flow velocity, which caused the bed erosion. Inversely, sediment is deposited on the back of the dune, where the gradient of sediment discharge is negative. Figures 6.15c &d depict the size fraction of the coarse and the fine sediments along the channel. Since the fine sediment on the left side of the dune was eroded, transported by the increased water velocity and deposited on the right side of dune due to the reduced water velocity. It leaded to an increasing coarse fraction on the left side of the dune and decreasing the coarse fraction on the right side. An opposite picture was obtained for distribution of the fine fraction. Variation of the size fractions resulted in changing the bed porosity (Figure 6.15b). Porosity obtains a minimal value of 0.2 on the right side of the dune at time 80000 (s), where the coarse fraction is approximately 0.69 and the fine fraction about 0.31. Increasing the fine fraction from this value caused the bed porosity to become larger. For the left side of the dune (the coarse fraction 0.73), growing the coarse fraction increases the bed porosity.

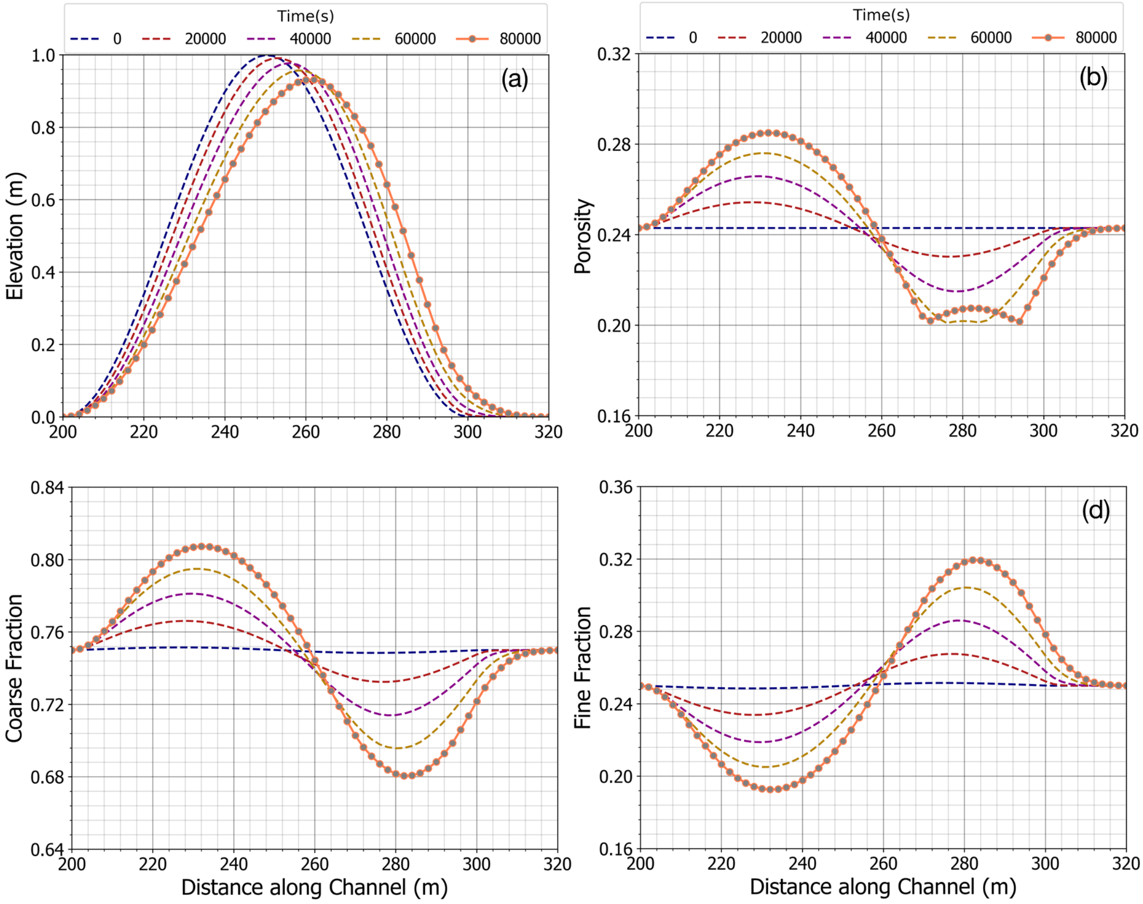

Figure 6.15 The performance of bed-porosity variation model in different times (a) – Bed elevation; (b) – Porosity of active-layer; (c) – Coarse size fraction of active-layer; (d) – Fine size fraction of active-layer.

Figure 6.16 compares the new model with a conventional model (with a constant porosity). In the conventional model, a constant value of 0.25 for bed porosity was selected, while in the new model it varied in a range from 0.21 to 0.28 due to size fraction change at the end of the calculation time. It can be seen that due to the larger values of the calculated bed porosity on the left side of the dune, the predicted bed elevations were slightly higher than those obtained from the conventional model. An opposite picture can be seen on the right side of the dune. The new model provided a qualitatively good picture of the bed form movement and porosity variation in the channel.

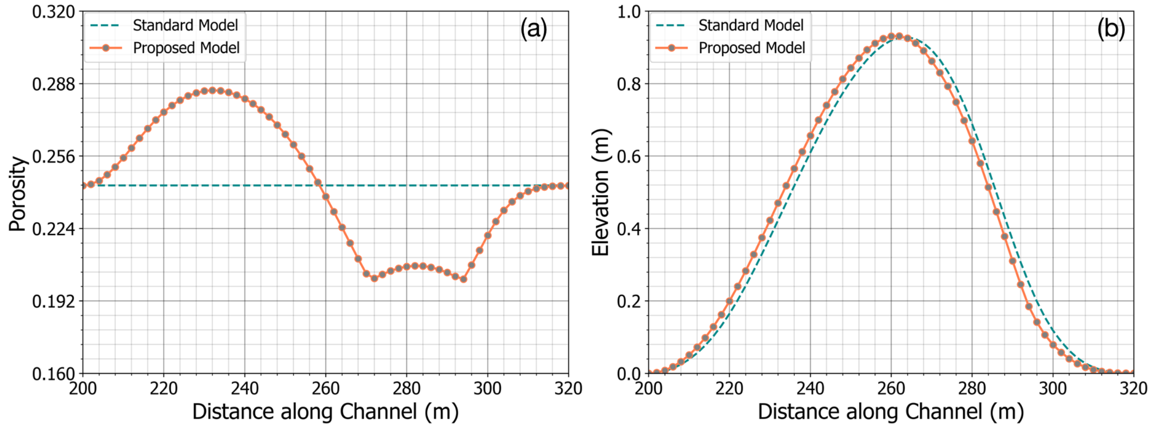

Figure 6.16 Comparison between the conventional model and the new model at the final time step (a) – Porosity of the active-layer; (b) – Bed elevation.

6.4.2 One layer bed porosity variation in comparison with Sulaiman's Experiment data

To identify the transformation processes of void structure in gravel-bed, experiments were conducted by Sulaiman, Tsutsumi, and Fujita (2007a) in a flume with a width of 0.40 m, a depth of 0.40 m and a working length of 7.0 m (Figure 6.17). The slope of the flume was adjusted to 1/50. Water discharge was kept nearly constant for all runs and circulated. A sediment mixture was initially placed in the working section and scraped flat. The thickness of the sediment layer was 5.3 cm. A weir with a height of 10 cm was placed at the end of the working section. The bed consisted of a coarse and fine fraction of sediments. The coarse fraction ranges from 4.75 mm to 26.5 mm in size with d_{50} = 15 mm, and the fine fraction ranges from 0.5 mm to 4.75 mm with d_o = 2 mm. The sediments were mixed and thoroughly homogenized. Experiments have been carried out for two situations. In Run-1, no sediment was supplied at the inlet; coarse sediment did not move actively, and only fine sediment was removed from the bed. In Run-2, an amount of the fine sediment fraction was continuously fed from the upstream of the flume; these fine sediments could be deposited into the coarse bed or transported downstream. The condition of the riverbed at the end of Run-1 was used as an initial condition of Run-2. Cumulative time steps for Run-1 are 20, 65, 130, 250 minutes and for Run 2 were 30, 50, 66, 82 minutes. The total duration of Run-1 and Run-2 was 332 minutes. The experimental conditions are summarized in Table 6.10. Water depth h and velocity v are the initial average water depth and velocity in the uniform region.

More details of the experiments description can be seen in Sulaiman, Tsutsumi, and Fujita (2007a).

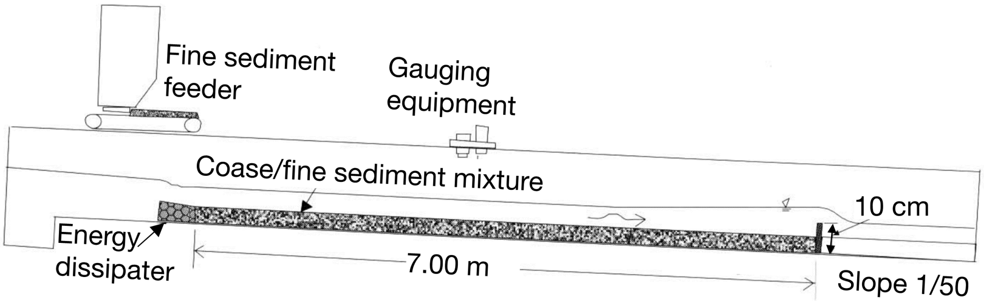

Figure 6.17 Schematic drawing of experimental channel and apparatus (Sulaiman, Tsutsumi, and Fujita, 2007a).

Table 6.10 Experimental conditions for two runs (Sulaiman, Tsutsumi, and Fujita, 2007a).

Exp.	$q_w(m^2/s)$	$q_s(10^{-6}m^2/s)$	$h(m)$	$v(m/s)$	Fr	τ_{fine}	τ_{coarse}
Run-1	0.034	0	0.039	0.879	1.428	0.178	0.026
Run-2	0.034	31.8	0.045	0.754	1.133	0.203	0.03

where: q_w - water discharge; q_s - sediment discharge; Fr - Froude number; τ - non-dimensional bed shear stress.

Figure 6.18 shows the comparison of simulated results and Sulaiman's results for the erosion case (Run-1) and deposition case (Run-2) with regard to bed elevation, fine fraction and porosity between, respectively. In figure 6.18a, the results of bed elevation with porosity variation are better than those in the constant models because of the incorporation of porosity changes in the developed model. The erosion of the upstream part in the developed model is a good fit with the experimental result while larger erosion of the upstream part of the constant model can be seen. The stored fine sediment in the pores of gravel-bed left the coarse layer increased the void space but did not contribute to the lowering of the bed level. This result is consistent with the findings of Frings, Kleinhans, and Vollmer (2008). Moreover, the storage capacity of the gravel-bed reached 30% while fine sediment fraction was greater than the range of 31% – 37%. As a result, the bed elevation at the final step is lower than the initial elevation because of the erosion of fine sediment on the surface. Downstream, the bed profiles of our and Sulaiman simulation are not good due to the bed load formula, which has not been developed for a mixture of two particle groups with very different grain sizes (Sulaiman, Tsutsumi, and Fujita, 2007b).

Figure 6.18b presents bed elevation, fine fraction and porosity to compare our results and Sulaiman's results for the deposition case (Run 2). The results of our bed elevation fit well compared to the results derived from Sulaiman and constant models. However, the bed level differences in all models are small due to a hidden function in the bed load equation for fine sediment on the upper gravel-bed surface, and because bed shear stress is larger than critical shear stress of most fine sediment. More detail about the comparison between the models can be seen in Table 6.11.

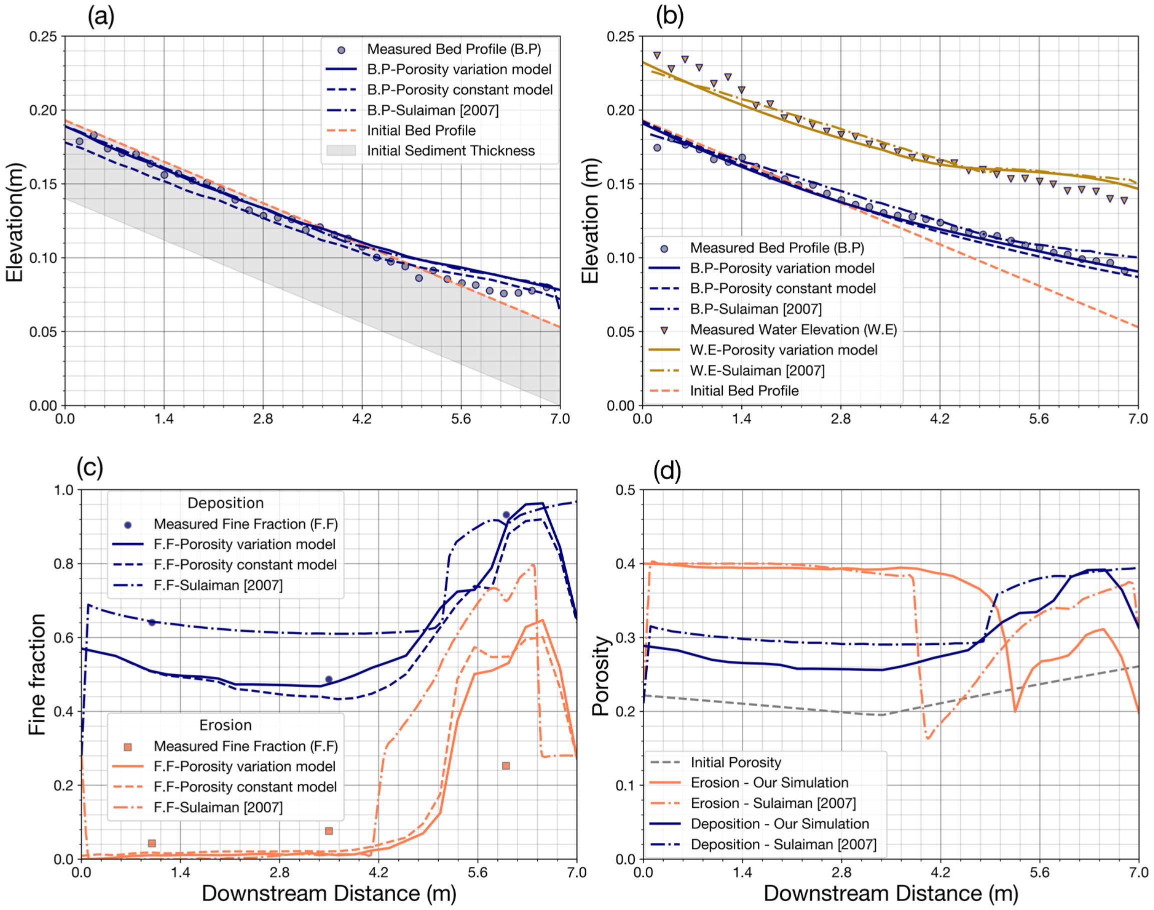

Figure 6.18 Bed variation for surface layer in comparison with observations from flume measurements: (a) bed elevation - erosion case; (b) bed elevation– deposition case (c) Fine fraction variation in erosion and deposition cases; (d) Porosity variation in erosion and deposition cases.

Table 6.11 Statistical performances of bed variation model within surface layer.

	Erosion			Deposition		
	Variation	Constant	Sulaiman	Variation	Constant	Sulaiman
	Bed Elevation					
R	0.99510	0.99442	0.99412	0.99451	0.99538	0.99465
RMSE	0.00585	0.00631	0.00560	0.00347	0.00490	0.00414
MAE	0.00451	0.00546	0.00442	0.00275	0.00424	0.00343
	Fine Fraction					
R	0.98936	0.98953	0.991247	0.96269	0.98205	0.96953
RMSE	0.16423	0.17410	0.26149	0.07897	0.09265	0.07297
MAE	0.12371	0.12518	0.18397	0.05929	0.08579	0.05088

Grain size distribution (size fractions) due to sediment exchange in the bed surface layer was investigated for two cases, one for erosion and the other for deposition. The calculated results were compared with Sulaiman's and constant porosity models, as well as the observed data.

Figure 6.18c shows the fine fraction along the flume in these two cases. In the erosion case, fine sediment is removed from the bed material on the upstream part and deposited on the downstream part. The fine sediment fraction upstream is nearly zero and equal to 0.6 downstream (Figure 6.18c-coral color line). In the deposition case (navy color line), the supplied fine sediment completely filled the pore of the bed material increasing fine fraction to 0.6 upstream and 0.96 downstream. The results show that the developed model with variable porosity is slightly better than the constant porosity model because the fine fraction in the developed model tends to fluctuate widely compared with those in the constant model. The results can be partly explained by considering the fine sediment stored in void spaces exchanged with sediment transport may lead to porosity changes. In Figure 6.18c – fine fraction for the deposition case, the results of Sulaiman are better than our results (navy color line), inversely our model performs better in erosion case (coral color line). The slight difference in the fine fraction results between our porosity variation model and Sulaiman porosity variation model and the significant variation in comparison of the porosity variation model and the constant model can be seen also in Table 6.11.

Figure 6.18d depicts the porosity due to sediment exchange on the surface layer in the cases of sediment erosion (coral color lines) and deposition (navy color lines). At the initial condition, the fine fraction upstream and downstream is from 37% to 22%, respectively and the diameter ratio is d_{coarse}/d_{fine} =7.5, while the minimum porosity is equal to 0.195. At the end of the simulation, the fine sediment wholly filled in the void structure of gravel at the middle of the flume. In the erosion case, most of the fine particles are removed from gravel upstream (x = 4.2 m), the porosity is reached the maximum value of 0.4. Afterward, the porosity decreased to a minimum value of 0.195 when the fine fraction increased from 0.22 to 0.30. In the deposition case, in contrast to the erosion case, the fine fraction is greater than 0.30 then porosity is proportional to a fine fraction. The increase in porosity in the deposition case is less than that in the erosion case.

6.4.3 Two layers bed porosity variation in comparison with SAFL's experiment data

SAFL (St. Anthony Falls Laboratory) downstream fining experiment is known as the most comprehensive set of experiments to date on gravel transport which were performed at the St. Anthony Falls Laboratory in Minnesota by Parker and his co-workers (Paola et al., 1992; Seal et al., 1997; Toro-Escobar et al., 2000). The experiment was conducted in a 0.305-m wide and 50-m long flume with an initial concrete-bottom slope of 0.002 (Figure 6.19), constant water discharge and a constant sediment feed rate. The flume is ponded at its downstream reach by setting a constant water surface elevation at the downstream end, which drives channel aggradation and downstream fining. The relevant parameters for the run are given in Table 6.12. A full description of the experimental data is given by Seal et al. (1995).

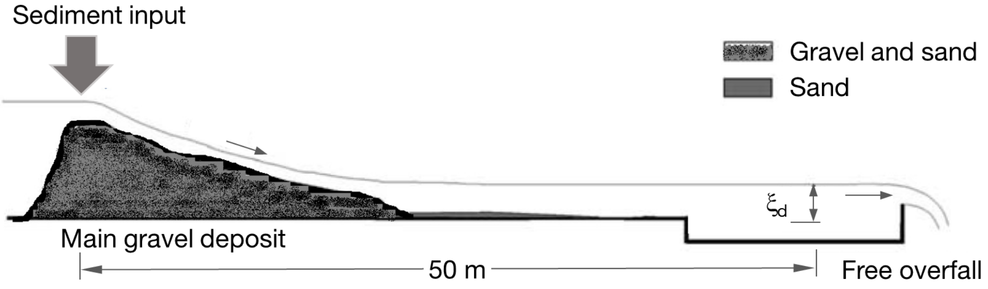

Figure 6.19 Flume set up for SAFL downstream fining experiments (Cui, 2007).

Table 6.12 Parameters for SAFL Downstream Fining Experiments.

Exp.	$q_w(m^2/s)$	$q_s(m^2/s)$	$\xi_d(m)$	$S_o(\%)$	$\beta_s(\%)$	Time (hour)
Run 1	0.163	2.3710^{-4}	0.4	0.20	33	2, 8,16.83

Notations: q_w: water discharge, q_s: sediment discharge, ξ_d downstream water depth, S_o: flume slope, β_s: sand fraction.

I simulated bed elevation, grain size distribution and porosity in the surface layer and subsurface layer considering the sediment exchange between these layers. A bed load equation developed by Wilcock and Crowe (2003b) was used to calculate sediment discharge for each size fraction. The thickness of the active layer is changing over time and space based on the multiplication of D_{90} and the coefficient of active layer thickness $n_{active} = 2$. The roughness height also varies over time and space defined by the product of D_{90} and roughness coefficient of n_k =1.8.

Bed profile due to sediment transport and sediment exchange between the surface layer and subsurface layer is presented in Figure 6.20 for comparing with Cui (2007) experiment results and simulation results (Figure 6.20a). The results were also compared with the constant model (Figure 6.20 b). It can be seen in figure 6.20a, b, that results of bed profile agree well with observations at 2h (red line), 8h (pink line) and 16.83h (blue line) simulations. Since in Cui's model, porosity was assumed as a constant of 0.3, I used this value for the initial condition in our simulation. The results in Figure 6.20a shows that our calculated bed profile has a higher correlation with observations than Cui's bed profile, especially on the upstream part. The good agreement between simulated results and experiments suggests that the developed model with a constant porosity could be adequately satisfied for applying in this study case. Figure 6.20b represents the bed profiles obtained from the porosity variation and those from constant porosity models. The first model provides slightly better results than those in the constant models (Table 6.13). Furthermore, the bed profile obtained from the variable porosity model gives a higher agreement with observation and lower values than those in the constant porosity model. This can be explained that porosity in the active layer and sub-layer tend to change in inverse directions. As a result, the total effect of porosity contributes unsubstantially on bed elevation.

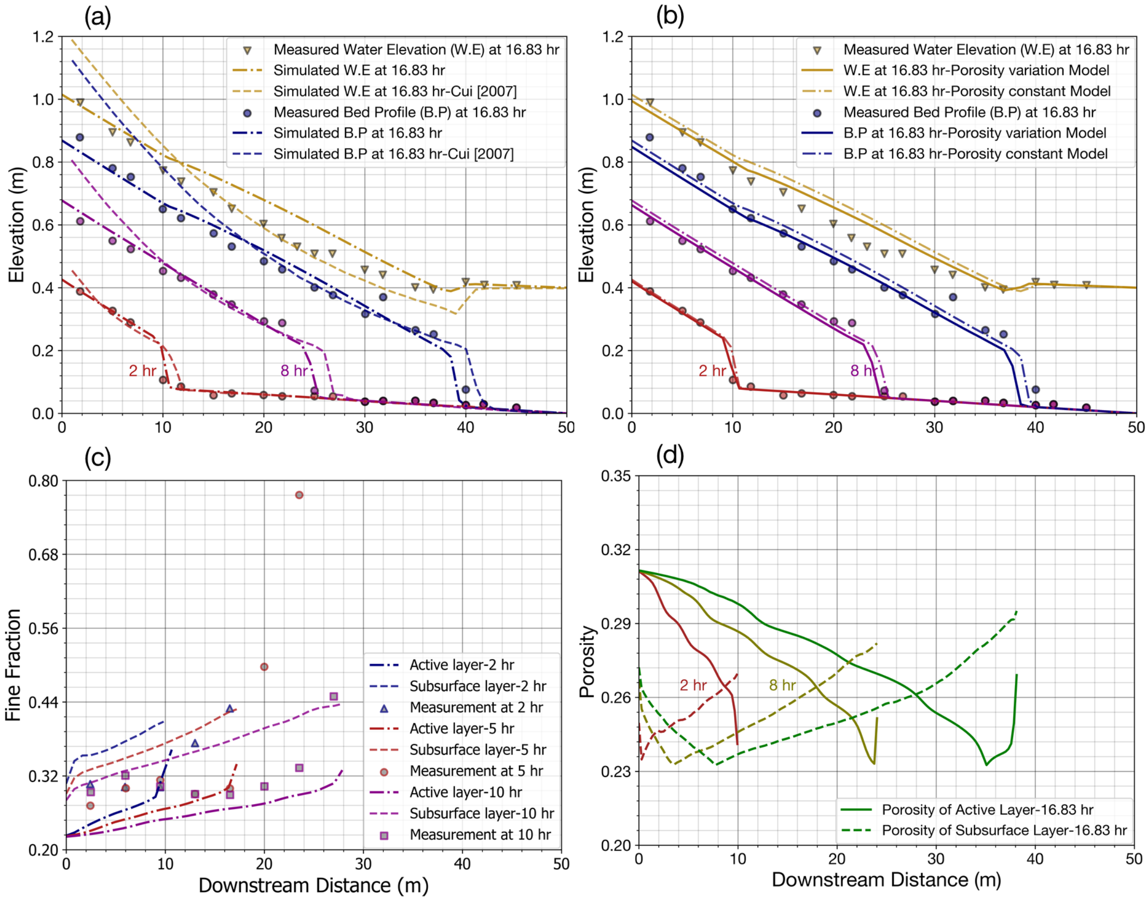

Figure 6.20 Simulated results of bed variation model in comparison with observations and previous study: (a) bed elevation-porosity constant model; (b) bed elevation-porosity variation model (c) Sand fraction-porosity variation model (d) Porosity variation.

Table 6.13 Statistical performances of bed variation model in two layers.

	2 hours			8 hours			16 hours		
	R	RMSE	MAE	R	RMSE	MAE	R	RMSE	MAE
Variation	0.987	0.019	0.010	0.998	0.016	0.013	0.989	0.033	0.027
Constant	0.980	0.023	0.011	0.996	0.024	0.018	0.988	0.034	0.032

Figure 6.20b shows the result of the constant porosity model for the variation of the sand fraction in the surface layer and subsurface layer. The predicted results are compared with the results of experiments and Cui's simulations (Cui, 2007). The simulated results of two layers for sand fraction variation are unable clearly to compare with the result of one layer (total bed) of the Cui simulation and experiment. However, from the obtained results, we

can realize that the trend of sand fraction variation in two-layer results is suitable with the variation of experimental results. The results of sand fraction variation obtained from the constant and variable porosity models will be compared with each other.

Figure 6.20c shows the fine fraction in the active layer and sublayer at 2h, 5h, and 10h. Fine fraction calculated by the variable porosity model at different time experiments is increased along with space (flume) and time. These results are suitable for the tendency of experiments with a lower value upstream and gradually increase downstream. For example, the fine fraction is varied from 0.20 to 0.40 along the flume in the active layer and 0.30 to 0.44 in sublayer. The predicted results also are in line with the conclusions of previous studies (Cui, 2007; Toro-Escobar et al., 2000).

Figure 6.20d shows the porosity change at different times of 2 hours, 8 hours, 16.83 hours for the active layer (solid line) and sub-layer (dash line). Porosity upstream on the surface layer is higher than those downstream while porosity in the sub-layer tends to increase after reaching the minimum value of 0.24 which is correlated with the gravel fraction and fine fraction (0.69 and 0.31, respectively). The variation in porosity gravel-bed is significant, since porosity in the active layer varies from 0.24 to 0.31 and from 0.24 to 0.30 for the sublayer.

The porosity of the active layer upstream is reaching maximum value due to high velocity and reduces gradually because flow velocity decreased along the flume. However, a suddenly reduction of velocity on the last part of downstream leads to a rapid increase in fine sediment. When a fine fraction is over the value of 0.31, then porosity also rises from 0.24 to 0.27 in the active layer. In contrast to the active layer, porosity in the sub-layer is not affected by high velocity, values of porosity on the upstream and downstream and reaching a minimum value of 0.23 as described by dash lines in Figure 6.20d.

Chapter 7

Conclusions

7.1 Summary

A profound understanding of the phenomenon of natural sediment transport in the gravel-bed river is critical to river management and eco-hydraulic simulation. Due to the complexity of the structure of bed river and mechanism of particles movements, numbers of conventional models attempting to simulate the sediment transport and bed variation are still limited by various assumptions. The proposed model in this study comes with bed porosity variabilities and considers the vertical fine sediment transport between multiple layers to assess the bed elevation variations and disturbance and grain sorting processes.

In this research, I developed a model framework to predict porosity and fine sediment distribution combining the Discrete Element Method and Artificial Neural Network. DEM realistically simulated porosity samples, fine sediment infiltration and the exchange rate between the surface and subsurface layers of the 3D gravel-bed structure. One image processing method, named Watershed Segmentation, was applied effectively in analyzing pore distribution. Algorithms were developed to calculate the exchange rate and the transferred coefficients as well as to extract the simulated DEM results to calculate grain size distribution and porosity. Based on that, eight different datasets were generated and applied to design several Artificial Neural Networks to predict porosity. Using a similar approach, twelve datasets were used to predict fine sediment distribution in a gravel-bed river. The impressive accurately results demonstrated that the combination of DEM and ANN is successful in simulating porosity, exchange rate and fine sediment distribution in the gravel-bed.

In addition, I integrated the porosity and fine sediment exchange rate in developing a new model for gravel-bed variation, not only by adding the porosity source term in the Exner's equation but also by calculating size fractions in the surface layer and subsurface layer by taking into account the exchange rate of fine sediment and porosity variation in multi-layer river bed.

The new model was verified by testing with three times with one numerical simulation and two experiments. The results indicated that the developed model can simulate bed variations considering the variable porosity in single and multiple layers. The application of this model helps stakeholders and managers to effectively maintain fine sediment stored in the riverbed and assess the effect of void spaces in gravel, home of small aquatic species, for eco-hydraulic management.

7.2 Recommendation

The model for bed variation which considers the change in porosity was just developed for one dimension and considers the exchange of fine sediment in two layers. As a next step, the bed variation needs to be developed for two dimensions and for considering the exchange of fine sediment in several subsurface layers.

The validity of the DEM models in the case of flowing water and sediment transport has not been tested. This model framework has a quite good performance for the analysis of bed and porosity changes. However, to increase the quality of the training data, the effect that flow velocity has on fine sediment packing into void spaces of gravel-bed should be considered by coupling LIGGGHTS with OpenFOAM to study fluid-particles interactions. This coupling model will be used to investigate the effect of shear stress, intra-gravel flow, and mobility gravel bed on the infiltration process and the bed porosity variation as well as to define the exchange rate of fine sediment between layers in gravel-bed rivers.

The Convolutional Neural Network (CNN) can be applied for segmenting the void spaces, fine sediment, and gravel, then the result images can be used to calculate gain size distribution, pore distribution, and estimate amount of fine sediment stored in the void space of gravel from the real picture of the river bed. This result of porosity, exchange rate and fine sediment fraction based on CNN segmentation will be used to train ANN and calibrate DEM model, and will be integrate with the developed bed porosity variation model.

References

Allen, John (1982). *Sedimentary structures, their character and physical basis*. Vol. 1. Elsevier. ISBN: 0080869432.

Asquith, GB (1985). “Handbook of Log Evaluation Techniques for Carbonate Reservoirs: Methods in Exploration Series No. 5”. In: *AAPG, Tulsa, Okla*.

Bagheripour, Parisa and Mojtaba Asoodeh (2013). “Fuzzy ruling between core porosity and petrophysical logs: Subtractive clustering vs. genetic algorithm–pattern search”. In: *Journal of Applied Geophysics* 99, pp. 35–41. ISSN: 0926-9851.

Bear, Jacob (2013). *Dynamics of fluids in porous media*. Courier Corporation. ISBN: 0486131807.

Beschta, Robert L and William L Jackson (1979). “The intrusion of fine sediments into a stable gravel bed”. In: *Journal of the Fisheries Board of Canada* 36.2, pp. 204–210. ISSN: 0706-652X.

Bhattacharya, B, RK Price, and DP Solomatine (2007). “Machine learning approach to modeling sediment transport”. In: *Journal of Hydraulic Engineering* 133.4, pp. 440–450. ISSN: 0733-9429.

Bogárdi, János and János Bogárdi (1974). *Sediment transport in alluvial streams*. Report. Akademiai Kiado Budapest.

Brown, Carl B (1950). *Sediment transportation*.

Bui, M. D., K. Kaveh, and P. Rutschmann (2015). “Integrating Artificial Neural Networks into Hydromorphological Model for Fluvial Channels”. In: *Proceedings of the 36th Iahr World Congress*, pp. 1673–1680. URL: <GotoISI>://WOS:000398996201002.

Bui, M. D. and P. Rutschmann (2012). “Numerical investigation of hydro-morphological changes due to training works in the Salzach River”. In: *River Flow 2012, Vols 1 and 2*, pp. 589–594. URL: <GotoISI>://WOS:000347871500078.

— (2010). “Numerical modelling of non-equilibrium graded sediment transport in a curved open channel”. In: *Computers & Geosciences* 36.6, pp. 792–800. ISSN: 0098-3004. DOI: 10.1016/j.cageo.2009.12.003. URL: <GotoISI>://WOS:000279095300011.

Bui, Minh Duc, Keivan Kaveh, Petr Penz, and Peter Rutschmann (2015). “Contraction scour estimation using data-driven methods”. In: *Journal of Applied Water Engineering and Research* 3.2, pp. 143–156. ISSN: 2324-9676.

Bui, Van Hieu, Minh Duc Bui, and Peter Rutschmann (2019). “Advanced Numerical Modeling of Sediment Transport in Gravel-Bed Rivers”. In: *Water* 11.3, p. 550.

— (2018). “Modeling infiltration process of fine sediment in gravel bed river”. In: *Wasserbau-Symposium Graz 2018*. Vol. 19. 512. Verlag der Technischen Universität Graz.

Bui M.D.; Bui, V.H.; Rutschmann (2018). “A new concept for modelling sediment transport in gravel bed rivers”. In: *Proc. of the 21st Vietnam Fluid Mechanics, Quynhon (in Vietnamese)*.

Campbell, Rhoda (2000). “Physical and Chemical Hydrogeology (2nd edition) by Patrick Domenico and Franklin W. Schwartz. John Wiley, Chichester, 1997. No. of pages: 506.

Price: £34.95 (hardback). ISBN 0-471-59762-7”. In: *Geological Journal* 35.2, pp. 133–134. DOI: doi:10.1002/1099-1034(200004/06)35:2<133::AID-GJ803>3.0.CO;2-S. URL: https://onlinelibrary.wiley.com/doi/abs/10.1002/1099.

Carling, PA and CP McCahon (1987). “Natural siltation of brown trout (Salmo trutta L.) spawning gravels during low-flow conditions”. In: *Regulated streams*. Springer, pp. 229–244.

Carling, Paul A (1984). “Deposition of fine and coarse sand in an open-work gravel bed”. In: *Canadian journal of fisheries and Aquatic Sciences* 41.2, pp. 263–270. ISSN: 0706-652X.

Carling, Paul A and Nigel A Reader (1982). “Structure, composition and bulk properties of upland stream gravels”. In: *Earth Surface Processes and Landforms* 7.4, pp. 349–365. ISSN: 0197-9337.

Carling, R. C. and D. Templeton (1982). “The effect of carbachol and isoprenaline on cell division in the exocrine pancreas of the rat”. In: *Q J Exp Physiol* 67.4, pp. 577–85. ISSN: 0144-8757 (Print) 0144-8757 (Linking). URL: https://www.ncbi.nlm.nih.gov/pubmed/6185966.

Chanson, Hubert (2004). *Hydraulics of open channel flow*. Elsevier. ISBN: 0080472974.

Chien, Ning (1956). “The present status of research on sediment transport”. In: *Transactions of the American Society of Civil Engineers* 121.1, pp. 833–868.

Cui, Y., J. K. Wooster, P. F. Baker, S. R. Dusterhoff, L. S. Sklar, and W. E. Dietrich (2008). “Theory of fine sediment infiltration into immobile gravel bed”. In: *Journal of Hydraulic Engineering-Asce* 134.10, pp. 1421–1429. ISSN: 0733-9429. DOI: 10.1061/(Asce)0733-9429(2008)134:10(1421). URL: <GotoISI>://WOS:000259255500002.

Cui, Yantao (2007). “The Unified Gravel-Sand (TUGS) Model: Simulating Sediment Transport and Gravel/Sand Grain Size Distributions in Gravel-Bedded Rivers”. In: *Water Resources Research* 43.10. DOI: doi:10.1029/2006WR005330. URL: https://agupubs.onlinelibrary.wiley.com/doi/abs/10.1029/2006WR005330.

Cundall, Peter A and Otto DL Strack (1979). “A discrete numerical model for granular assemblies”. In: *geotechnique* 29.1, pp. 47–65. ISSN: 0016-8505.

Cunge, Jan Andrzej, Forrest M Holly, and Adri Verwey (1980). “Practical aspects of computational river hydraulics”. In:

Cunningham, AB, CJ Anderson, and H Bouwer (1987). “Effects of sediment-laden flow on channel bed clogging”. In: *Journal of irrigation and drainage engineering* 113.1, pp. 106–118. ISSN: 0733-9437.

Díaz, MJ Castro, Enrique D Fernández-Nieto, and AM Ferreiro (2008). “Sediment transport models in shallow water equations and numerical approach by high order finite volume methods”. In: *Computers & Fluids* 37.3, pp. 299–316. ISSN: 0045-7930.

Desmond, Kenneth W and Eric R Weeks (2014). “Influence of particle size distribution on random close packing of spheres”. In: *Physical Review E* 90.2, p. 022204.

Dietrich, William E., James W. Kirchner, Hiroshi Ikeda, and Fujiko Iseya (1989). “Sediment supply and the development of the coarse surface layer in gravel-bedded rivers”. In: *Nature* 340, p. 215. DOI: 10.1038/340215a0. URL: http://dx.doi.org/10.1038/340215a0.

DuBoys, P (1879). “Le Rhone et les rivieres a lit affouillable”. In: *Annales des Ponts et Chaussees, Series*. Vol. 5. 18, pp. 141–195.

Dudill, Ashley, Philippe Frey, and Michael Church (2017). “Infiltration of fine sediment into a coarse mobile bed: a phenomenological study”. In: *Earth Surface Processes and Landforms* 42.8, pp. 1171–1185. ISSN: 0197-9337.

Einstein, Hans A (1968). “Deposition of suspended particles in a gravel bed”. In: *Journal of the Hydraulics Division* 94.5, pp. 1197–1206.

Einstein, Hans Albert (1941). “Formulas for the transportation of bed load”. In: *Transactions of ASCE*, pp. 561–597.

— (1950). *The bed-load function for sediment transportation in open channel flows*. Report.

Fleischmann, Jonathan, Radu Serban, Dan Negrut, and Paramsothy Jayakumar (2015). *On the Importance of Displacement History in Soft-Body Contact Models*. Vol. 11. DOI: 10.1115/1.4031197.

Frings, R. M., M. G. Kleinhans, and S. Vollmer (2008). “Discriminating between pore-filling load and bed-structure load: a new porosity-based method, exemplified for the river Rhine”. In: *Sedimentology* 55.6, pp. 1571–1593. ISSN: 0037-0746. DOI: 10.1111/j.1365-3091.2008.00958.x. URL: <GotoISI>://WOS:000261084900003.

Frings, R. M., H. Schuttrumpf, and S. Vollmer (2011). “Verification of porosity predictors for fluvial sand-gravel deposits”. In: *Water Resources Research* 47. ISSN: 0043-1397. DOI: ArtnW0752510.1029/2010wr009690. URL: <GotoISI>://WOS:000292844300003.

Frostick, Lynne E, PM Lucas, and I Reid (1984). “The infiltration of fine matrices into coarse-grained alluvial sediments and its implications for stratigraphical interpretation”. In: *Journal of the Geological Society* 141.6, pp. 955–965. ISSN: 0016-7649.

Gayraud, Sebastien and Michel Philippe (2003). “Influence of Bed-Sediment Features on the Interstitial Habitat Available for Macroinvertebrates in 15 French Streams”. In: *International Review of Hydrobiology* 88.1, pp. 77–93. ISSN: 1434-2944. DOI: 10.1002/iroh.200390007. URL: https://doi.org/10.1002/iroh.200390007.

Geotechdata.info (2013). “Soil void ratio”. In: *http://geotechdata.info/parameter/soil-void-ratio.html (as of November 16, 2013)*.

Gibson, S, R Heath, D Abraham, and D Schoellhamer (2011). “Visualization and analysis of temporal trends of sand infiltration into a gravel bed”. In: *Water Resources Research* 47.12. ISSN: 1944-7973.

Gibson, Stanford, David Abraham, Ronald Heath, and David Schoellhamer (2010). “Bridging Process Threshold for Sediment Infiltrating into a Coarse Substrate”. In: *Journal of Geotechnical and Geoenvironmental Engineering* 136.2, pp. 402–406. DOI: doi:10.1061/(ASCE)GT.1943-5606.0000219. URL: https://ascelibrary.org/doi/abs/10.1061/.

— (2009a). “Vertical gradational variability of fines deposited in a gravel framework”. In: *Sedimentology* 56.3, pp. 661–676. DOI: doi:10.1111/j.1365-3091.2008.00991.x. URL: https://onlinelibrary.wiley.com/doi/abs/10.1111/j.1365-3091.2008.00991.x.

— (2009b). “Vertical gradational variability of fines deposited in a gravel framework”. In: *Sedimentology* 56.3, pp. 661–676.

Glover, Paul (2000). “Petrophysics MSc course notes”. In: *University of Leeds, UK*.

Hales, Thomas C (2005). “A proof of the Kepler conjecture”. In: *Annals of mathematics*, pp. 1065–1185. ISSN: 0003-486X.

Haykin, Simon and Neural Network (2004). “A comprehensive foundation”. In: *Neural networks* 2.2004, p. 41.

He, Ziyang, Xiaoqing Zhang, Yangjie Cao, Zhi Liu, Bo Zhang, and Xiaoyan Wang (2018). “LiteNet: Lightweight neural network for detecting arrhythmias at resource-constrained mobile devices”. In: *Sensors* 18.4, p. 1229.

Heaton, Jeff (2008). *Introduction to neural networks with Java*. Heaton Research, Inc. ISBN: 1604390085.

Hervouet, Jean-Michel (2007). *Hydrodynamics of free surface flows: modelling with the finite element method*. John Wiley & Sons. ISBN: 0470319631.

Hickin, Edward J (1995). *River Geomorphology*. John Wiley & Son Limited. ISBN: 9780471955313. URL: https://books.google.de/books?id=DsYPAQAAIAAJ.

Hirano, Muneo (1971). “River-bed degradation with armoring”. In: *Proceedings of the Japan Society of Civil Engineers*. Vol. 1971. 195. Japan Society of Civil Engineers, pp. 55–65.

Hoey, T. B. and R. Ferguson (1994). “Numerical-Simulation of Downstream Fining by Selective Transport in Gravel-Bed Rivers - Model Development and Illustration”. In: *Water Resources Research* 30.7, pp. 2251–2260. ISSN: 0043-1397. URL: <GotoISI>://WOS:A1994NV57900025.

Holdich, Richard G (2002). *Fundamentals of particle technology*. Midland Information Technology and Publishing. ISBN: 0954388100.

Hudson, Justin (2001). “Numerical techniques for morphodynamic modelling”. Thesis.

Hudson, Justin and Peter K Sweby (2005). “A high-resolution scheme for the equations governing 2D bed-load sediment transport”. In: *International Journal for Numerical Methods in Fluids* 47.10-11, pp. 1085–1091. ISSN: 0271-2091.

Huston, Davis L and James F Fox (2015). “Clogging of fine sediment within gravel substrates: Dimensional analysis and macroanalysis of experiments in hydraulic flumes”. In: *Journal of Hydraulic Engineering* 141.8, p. 04015015. ISSN: 0733-9429.

Iseya, Fujiko and Hiroshi Ikeda (1987). “Pulsations in bedload transport rates induced by a longitudinal sediment sorting: A flume study using sand and gravel mixtures”. In: *Geografiska Annaler: Series A, Physical Geography* 69.1, pp. 15–27. ISSN: 0435-3676.

Jangid, Mahesh and Sumit Srivastava (2018). “Handwritten Devanagari Character Recognition Using Layer-Wise Training of Deep Convolutional Neural Networks and Adaptive Gradient Methods”. In: *Journal of Imaging* 4.2, p. 41.

Johnson, KL (1974). *Contact mechanics, 1985*.

Julien, Pierre Y (2010). *Erosion and sedimentation*. Cambridge University Press. ISBN: 1139486969.

Kalinske, AA (1947). “Movement of sediment as bed load in rivers”. In: *Eos, Transactions American Geophysical Union* 28.4, pp. 615–620. ISSN: 2324-9250.

Kamann, Patrick J, Robert W Ritzi, David F Dominic, and Caleb M Conrad (2007). “Porosity and permeability in sediment mixtures”. In: *Groundwater* 45.4, pp. 429–438. ISSN: 0017-467X.

Ketcham, Richard A (2005). “Three-dimensional grain fabric measurements using high-resolution X-ray computed tomography”. In: *Journal of Structural Geology* 27.7, pp. 1217–1228. ISSN: 0191-8141.

Kingma, Diederik P and Jimmy Ba (2014). “Adam: A method for stochastic optimization”. In: *arXiv preprint arXiv:1412.6980*.

Koltermann, Christine E and Steven M Gorelick (1995). “Fractional packing model for hydraulic conductivity derived from sediment mixtures”. In: *Water Resources Research* 31.12, pp. 3283–3297. ISSN: 0043-1397.

Komura, S (1963). “Discussion of “Sediment transportation mechanics: introduction and properties of sediment””. In: *Journal of the Hydraulics Division, ASCE* 89.HY1, pp. 263–266.

Kraipeerapun, Pawalai, Chun Che Fung, and Sathit Nakkrasae (2009). “Porosity prediction using bagging of complementary neural networks”. In: *International Symposium on Neural Networks*. Springer, pp. 175–184.

Krumbein, William Christian (1934). “Size frequency distributions of sediments”. In: *Journal of sedimentary Research* 4.2, pp. 65–77. ISSN: 1938-3681.

Kubatko, Ethan J, Joannes J Westerink, and Clint Dawson (2006). “An unstructured grid morphodynamic model with a discontinuous Galerkin method for bed evolution”. In: *Ocean modelling* 15.1-2, pp. 71–89. ISSN: 1463-5003.

Landau, LD and EM Lifshitz (1986). “Theory of Elasticity, 3rd”. In: *ed: Pergamon Press, Oxford, UK.*

Lauck, Tim (1991). “A simulation model for the infiltration of sediment into spawning gravel”. Thesis.

Laurien, Eckart and Herbert Oertel Jr (2009). “Numerische Strömungsmechanik”. In: *Viewegþ-Teubner, Wiesbaden, Germany.*

Legates, David R and Gregory J McCabe Jr (1999). “Evaluating the use of “goodness-of-fit” measures in hydrologic and hydroclimatic model validation”. In: *Water resources research* 35.1, pp. 233–241. ISSN: 0043-1397.

Leonardson (2010). “Exchange of fine sediments with gravel riverbeds”. Thesis.

Link, Curtis A and Phillip A Himmer (2003). “Oil reservoir porosity prediction using a neural network ensemble approach”. In: *Geophysical Applications of Artificial Neural Networks and Fuzzy Logic*. Springer, pp. 197–213.

Malpica, Norberto, Carlos Ortiz De Solórzano, Juan José Vaquero, Andrés Santos, Isabel Vallcorba, José Miguel García-Sagredo, and Francisco Del Pozo (1997). “Applying watershed algorithms to the segmentation of clustered nuclei”. In: *Cytometry: The Journal of the International Society for Analytical Cytology* 28.4, pp. 289–297. ISSN: 0196-4763.

Matthias, Brunke (1999). “Colmation and Depth Filtration within Streambeds: Retention of Particles in Hyporheic Interstices”. In: *International Review of Hydrobiology* 84.2, pp. 99–117. DOI: doi:10.1002/iroh.199900014. URL: https://onlinelibrary.wiley.com/doi/abs/10.1002/iroh.199900014.

McGeary, RK (1961). “Mechanical packing of spherical particles”. In: *Journal of the American ceramic Society* 44.10, pp. 513–522. ISSN: 0002-7820.

Meyer-Peter, Eugen and R Müller (1948). “Formulas for bed-load transport”. In: *IAHSR 2nd meeting, Stockholm, appendix 2*. IAHR.

Mindlin, RD (1949). “Compliance of elastic bodies in contact”. In: *J. Appl. Mech. Trans. ASME* 16, pp. 259–268.

Navaratnam, Christy Ushanth, Jochen Aberle, and Jana Daxnerová (2018). “An Experimental Investigation on Porosity in Gravel Beds”. In: *Free Surface Flows and Transport Processes*. Springer, pp. 323–334.

Nolan, GT and PE Kavanagh (1993). “Computer simulation of random packings of spheres with log-normaldistributions”. In: *Powder Technology* 76.3, pp. 309–316. ISSN: 0032-5910.

Nunez-Gonzalez, F., J. P. Martin-Vide, and M. G. Kleinhans (2016). “Porosity and size gradation of saturated gravel with percolated fines”. In: *Sedimentology* 63.5, pp. 1209–1232. ISSN: 0037-0746. DOI: 10.1111/sed.12257. URL: <GotoISI>://WOS:000379930500008.

Onoda, George Y and Eric G Liniger (1990). “Random loose packings of uniform spheres and the dilatancy onset”. In: *Physical review letters* 64.22, p. 2727.

OR3D (2019). Web Page. URL: https://www.or3d.co.uk/knowledge-base/x-ray-inspection-for-composite-materials-and-fibres/.

Ouchiyama, Norio and Tatsuo Tanaka (1984). “Porosity estimation for random packings of spherical particles”. In: *Industrial & engineering chemistry fundamentals* 23.4, pp. 490–493. ISSN: 0196-4313.

Paola, Chris, Gary Parker, Rebecca Seal, Sanjiv K Sinha, John B Southard, and Peter R Wilcock (1992). “Downstream fining by selective deposition in a laboratory flume”. In: *Science* 258.5089, pp. 1757–1760. ISSN: 0036-8075.

Parker, Gary (1990a). “Surface-based bedload transport relation for gravel rivers”. In: *Journal of hydraulic research* 28.4, pp. 417–436. ISSN: 0022-1686.

Parker, Gary (1990b). *The acronym series of Pascal programs for computing bedload transport in gravel rivers*. St. Anthony Falls Hydraulic Laboratory, Universityof Minnesota.

Peronius, N and TJ Sweeting (1985). "On the correlation of minimum porosity with particle size distribution". In: *Powder technology* 42.2, pp. 113–121. ISSN: 0032-5910.

Pletcher, Richard H, John C Tannehill, and Dale Anderson (2012). *Computational fluid mechanics and heat transfer*. CRC press. ISBN: 1591690374.

Rabbani, Arash and Shahab Ayatollahi (2015). "Comparing three image processing algorithms to estimate the grain-size distribution of porous rocks from binary 2D images and sensitivity analysis of the grain overlapping degree". In: *Special Topics & Reviews in Porous Media: An International Journal* 6.1. ISSN: 2151-4798.

Rabbani, Arash, Saeid Jamshidi, and Saeed Salehi (2014). "An automated simple algorithm for realistic pore network extraction from micro-tomography images". In: *Journal of Petroleum Science and Engineering* 123, pp. 164–171. ISSN: 0920-4105.

Rezzolla, Luciano (2011). "Numerical methods for the solution of partial differential equations". In: *Lecture Notes for the COMPSTAR School on Computational Astrophysics*, pp. 8–13.

Ridgway, K and KJ Tarbuck (1968). "Voidage fluctuations in randomly-packed beds of spheres adjacent to a containing wall". In: *Chemical Engineering Science* 23.9, pp. 1147–1155. ISSN: 0009-2509.

Rodi, Wolfgang, George Constantinescu, and Thorsten Stoesser (2013). *Large-eddy simulation in hydraulics*. Crc Press. ISBN: 0203797574.

Sakthivadivel, Ramaswamy and Hans Albert Einstein (1970). "Clogging of porous column of spheres by sediment". In: *Journal of the Hydraulics Division* 96.2, pp. 461–472.

Saljooghi, B Shokooh and A Hezarkhani (2014). "Comparison of WAVENET and ANN for predicting the porosity obtained from well log data". In: *Journal of Petroleum Science and Engineering* 123, pp. 172–182. ISSN: 0920-4105.

Schälchli, Ueli (1995). "Basic equations for siltation of riverbeds". In: *Journal of Hydraulic Engineering* 121.3, pp. 274–287. ISSN: 0733-9429.

— (1992). "The clogging of coarse gravel river beds by fine sediment". In: *Hydrobiologia* 235.1, pp. 189–197. ISSN: 1573-5117. DOI: 10.1007/bf00026211. URL: https://doi.org/10.1007/BF00026211.

Scott, GD and DM Kilgour (1969). "The density of random close packing of spheres". In: *Journal of Physics D: Applied Physics* 2.6, p. 863. ISSN: 0022-3727.

Seal, R, G Parker, C Paola, and B Mullenbach (1995). "Laboratory experiments on downstream fining of gravel, narrow channel runs 1 through 3: supplemental methods and data". In: *External memorandum M* 239.

Seal, Rebecca, Chris Paola, Gary Parker, John B Southard, and Peter R Wilcock (1997). "Experiments on downstream fining of gravel: I. Narrow-channel runs". In: *Journal of hydraulic engineering* 123.10, pp. 874–884. ISSN: 0733-9429.

Sear, DA (1993). "Fine sediment infiltration into gravel spawning beds within a regulated river experiencing floods: ecological implications for salmonids". In: *Regulated Rivers: Research & Management* 8.4, pp. 373–390. ISSN: 0886-9375.

Selby, M.J. and A.P.W. Hodder (1993). *Hillslope Materials and Processes*. Oxford University Press. ISBN: 9780198741831. URL: https://books.google.de/books?id=Qj27QgAACAAJ.

Sheppard, Adrian P, Robert M Sok, and Holger Averdunk (2004). "Techniques for image enhancement and segmentation of tomographic images of porous materials". In: *Physica A: Statistical mechanics and its applications* 339.1-2, pp. 145–151. ISSN: 0378-4371.

Shields, Albert (1936). “Application of similarity principles and turbulence research to bed-load movement”. In:

Soppe, W (1990). “Computer simulation of random packings of hard spheres”. In: *Powder technology* 62.2, pp. 189–197. ISSN: 0032-5910.

Stratos, Karl (2019). *Feedforward and recurrent neural networks*. Web Page. URL: http://karlstratos.com/notes/neural.pdf.

Sulaiman, Muhammad, Daizo Tsutsumi, and Masaharu Fujita (2007a). “Bed variation model considering porosity change in riverbed material”. In: *Journal of the Japan Society of Erosion Control Engineering* 60, pp. 11–18.

— (2007b). “Porosity of sediment mixtures with different type of grain size distribution”. In: *Annual Journal of Hydraulic Engineering* 51, pp. 133–138.

Suzuki, Michitaka and Toshio Oshima (1983). “Estimation of the co-ordination number in a multi-component mixture of spheres”. In: *Powder technology* 35.2, pp. 159–166. ISSN: 0032-5910.

Toro-Escobar, C. M., G. Parker, and C. Paola (1996). “Transfer function for the deposition of poorly sorted gravel in response to streambed aggradation”. In: *Journal of Hydraulic Research* 34.1, pp. 35–53. ISSN: 0022-1686. URL: <GotoISI>://WOS:A1996UA45800004.

Toro-Escobar, Carlos M, Chris Paola, Gary Parker, Peter R Wilcock, and John B Southard (2000). “Experiments on downstream fining of gravel. II: Wide and sandy runs”. In: *Journal of Hydraulic Engineering* 126.3, pp. 198–208. ISSN: 0733-9429.

Valdes, Julio R and J Carlos Santamarina (2008). “Clogging: bridge formation and vibration-based destabilization”. In: *Canadian Geotechnical Journal* 45.2, pp. 177–184. ISSN: 0008-3674.

Verstraeten, Gert and Jean Poesen (2001). “Variability of dry sediment bulk density between and within retention ponds and its impact on the calculation of sediment yields”. In: *Earth Surface Processes and Landforms* 26.4, pp. 375–394. DOI: doi:10.1002/esp.186. URL: https://onlinelibrary.wiley.com/doi/abs/10.1002/esp.186.

White, Frank M and Isla Corfield (2006). *Viscous fluid flow*. Vol. 3. McGraw-Hill New York.

Wilcock, Peter R (1998). “Two-fraction model of initial sediment motion in gravel-bed rivers”. In: *Science* 280.5362, pp. 410–412. ISSN: 0036-8075.

Wilcock, Peter R and Joanna C Crowe (2003a). “Surface-based transport model for mixed-size sediment”. In: *Journal of Hydraulic Engineering* 129.2, pp. 120–128. ISSN: 0733-9429.

— (2003b). “Surface-based transport model for mixed-size sediment”. In: *Journal of Hydraulic Engineering* 129.2, pp. 120–128. ISSN: 0733-9429.

Wilcock, Peter R. and Brendan T. DeTemple (2005). “Persistence of armor layers in gravel-bed streams”. In: *Geophysical Research Letters* 32.8. DOI: doi:10.1029/2004GL021772. URL: https://agupubs.onlinelibrary.wiley.com/doi/abs/10.1029/2004GL021772.

Wilcock, Peter R. and Stephen T. Kenworthy (2002). “A two-fraction model for the transport of sand/gravel mixtures”. In: *Water Resources Research* 38.10, pp. 12–1–12–12. DOI: doi:10.1029/2001WR000684. URL: https://agupubs.onlinelibrary.wiley.com/doi/abs/10.1029/2001WR000684.

Wildenschild, Dorthe and Adrian P Sheppard (2013). “X-ray imaging and analysis techniques for quantifying pore-scale structure and processes in subsurface porous medium systems”. In: *Advances in Water Resources* 51, pp. 217–246. ISSN: 0309-1708.

Wilson, EJ and CJ Geankoplis (1966). “Liquid mass transfer at very low Reynolds numbers in packed beds”. In: *Industrial & Engineering Chemistry Fundamentals* 5.1, pp. 9–14. ISSN: 0196-4313.

Wood, Paul J. and Patrick D. Armitage (1997). “Biological Effects of Fine Sediment in the Lotic Environment”. In: *Environmental Management* 21.2, pp. 203–217. ISSN: 1432-1009. DOI: 10.1007/s002679900019. URL: https://doi.org/10.1007/s002679900019.

Wooster, J. K., S. R. Dusterhoff, Y. T. Cui, L. S. Sklar, W. E. Dietrich, and M. Malko (2008). “Sediment supply and relative size distribution effects on fine sediment infiltration into immobile gravels”. In: *Water Resources Research* 44.3. ISSN: 0043-1397. DOI: ArtnW0342410.1029/2006wr005815. URL: <GotoISI>://WOS:000254529600001.

Wu, Fu-Chun and Hung-Tzu Huang (2000). “Hydraulic resistance induced by deposition of sediment in porous medium”. In: *Journal of Hydraulic Engineering* 126.7, pp. 547–551. ISSN: 0733-9429.

Wu, Weiming and Sam SY Wang (2006). “Formulas for sediment porosity and settling velocity”. In: *Journal of Hydraulic Engineering* 132.8, pp. 858–862. ISSN: 0733-9429.

Yu, A. B. and N. Standish (1991). “Estimation of the Porosity of Particle Mixtures by a Linear-Mixture Packing Model”. In: *Industrial & Engineering Chemistry Research* 30.6, pp. 1372–1385. ISSN: 0888-5885. DOI: DOI10.1021/ie00054a045. URL: <GotoISI>://WOS:A1991FP86000045.

— (1993). “Limitation of Proposed Mathematical-Models for the Porosity Estimation of Nonspherical Particle Mixtures”. In: *Industrial & Engineering Chemistry Research* 32.9, pp. 2179–2182. ISSN: 0888-5885. DOI: DOI10.1021/ie00021a043. URL: <GotoISI>://WOS:A1993LW54200043.